Bragg Diffraction Imaging

Overcoming Angular Uncertainty

Chen, Huaiyu

2025

Bragg Diffraction Imaging

Overcoming Angular Uncertainty

HUAIYU CHEN
SYNCHROTRON RADIATION RESEARCH | FACULTY OF SCIENCE | LUND UNIVERSITY

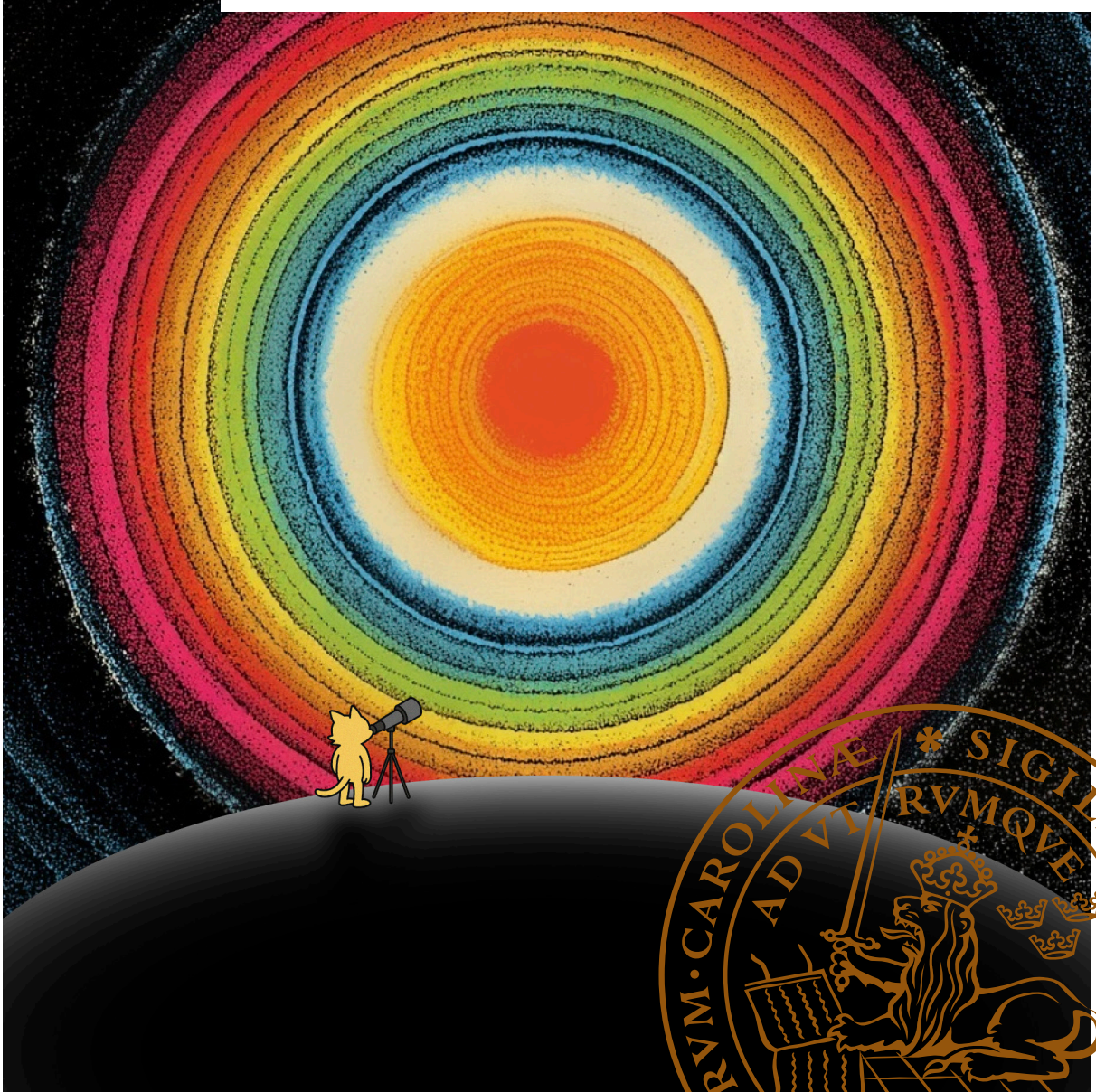

Printed by Media-Tryck, Lund 2025 NORDIC SWAN ECOLABEL 3041 0903

LUND UNIVERSITY

Faculty of Science
Department of Physics
Division of Synchrotron Radiation Research

ISBN 978-91-8104-620-5

Bragg Diffraction Imaging:
Overcoming Angular Uncertainty

Bragg Diffraction Imaging

Overcoming Angular Uncertainty

Huaiyu Chen

LUND
UNIVERSITY

DOCTORAL DISSERTATION

Doctoral dissertation for the degree of Doctor of Philosophy (PhD) at the Faculty of Science at Lund University to be publicly defended on 19th of September at 09.15 in Rydberg lecture Hall, Department of Physics

Faculty opponent
Dr. Tobias Schülli
European Synchrotron Radiation Facility, Grenoble, France

Organization: LUND UNIVERSITY
Division of Synchrotron Radatiation Research
Department of Physics, Box 118
S-22100 Lund

Date of issue: 2025-09-19

Sponsoring organization:

Document name: Doctoral dissertation

Author(s): Huaiyu Chen

Title and subtitle: Bragg Diffraction Imaging: Overcoming Angular Uncertainty

Abstract:
Probing the internal structure of crystalline materials is vital for understanding and optimizing their functional properties, especially in semiconductors and multiferroics, where nanoscale distortions such as strain and lattice tilt can dramatically affect performance. Among various characterization tools, X-ray diffraction imaging offers a unique combination of deep penetration, nondestructive measurement, and high strain sensitivity.

This thesis focuses on Bragg Cohereht Diffraction Imaging (BCDI), a powerful technique that reconstructs three-dimensional internal displacement fields in crystals from coherent X-ray diffraction patterns. While BCDI offers high-resolution structural information, its practical implementation faces a critical challenge: angular instability during data acquisition, which can lead to severe distortions and artifacts in the reconstruction. Addressing this limitation forms the central theme of this work.

A robust angular correction algorithm is developed to mitigate for such distortions, and its effectiveness is demonstrated in experimental studies, including BCDI measurements on heterostructured nanowires. To further relax the stringent sampling requirements of BCDI, a deep learning–based strategy is introduced that enables diffraction volume reconstruction from completely unordered and angularly distorted datasets. Together, these methods aim to enhace the robustness of BCDI and make it more adaptable to complex, dynamic, or extreme experimental conditions.

In addition, scanning X-ray diffraction (nano-XRD) is employed to map local strain and lattice tilt in extended crystalline materials, such as ferroelectric thin films and nanowires. Nano-XRD serves as a practical probe of the internal structure of the extended sample.

Overall, this thesis demonstrates the potential of synchrotron-based X-ray diffraction imgaging tehnique for revealing internal crystalline structures, offering valuable tools for both fundamental research and advanced technological development.

Key words: X-ray diffraction, internal structure, crystalline materials, angular distortion, deep learning

Language English **Number of pages**:101

ISSN and key title:

ISBN: ISBN 978-91-8104-620-5 (print), ISSN 978-91-8104-621-2 (electronic)

Recipient's notes PriceSecurity classification

Signature Date 2025-08-07

Bragg Diffraction Imaging

Overcoming Angular Uncertainty

by Huaiyu Chen

LUND
UNIVERSITY

Division of Synchrotron Radiation Research
Department of Physics
Faculty of Science
Lund University

ISBN 978-91-8104-620-5 (print)
ISSN 978-91-8104-621-2 (electronic)

Printed in Sweden by Media-Tryck, Lund University, Lund 2025

致我的家人与好友

To my beloved family and my friends

Acknowledgements

Almost five years ago, I sat on a train to the airport at 6 a.m., my suitcases beside me and a mask covering my face. I felt dizzy—not just from the mask or lack of sleep, but from the anticipation of the journey ahead. Funnily enough, my time in Sweden began with an unexpected engine failure of the train from Stockholm to Lund—a moment that has now become a fond memory. Since then, this journey has been filled with both ups and downs, challenges and joys, and, most importantly, the incredible people I have met along the way.

First and foremost, my deepest gratitude goes to my main supervisor, Jesper Wallentin, for his invaluable guidance throughout this entire journey. This thesis would not have been possible without you. You were always patient and supportive—not only when I had questions or doubts in research, but also in many other aspects of academic and personal life. Thank you for giving me the opportunity to work with you—I have learned so much from this experience.

I would also like to extend my thanks to my co-supervisors, Pablo Villanueva-Pérez and Megan O. Hill Landberg. Thank you, Pablo, for introducing me to the world of deep learning, and for your feedback, advice, and inspiring discussions along the way. Thank you, Megan, for all your support during beamtimes, for patiently answering my many questions about materials science, and for putting up with my sometimes clumsy language. It has always been a pleasure to talk with you. I'm also grateful to my former co-supervisors, Alexander Björling and Dmitry Dzhigaev. Though you have left academia, I truly appreciate everything you taught me, especially the basis of Bragg coherent diffraction imaging.

My thanks and appreciation also go to everyone in our group at SLJUS. Thanks for all the dinners after group meetings, even if they only happened a few times a year. To Klara, Leo, Sanna, Hanna, Lucas, Megan and Dmitry, thank you for being amazing, supportive, and collaborative. We went through so many challenging and exciting beamtimes together, but somehow always forgot to take group photos. To Lert, thanks for the blessing on your last working day here. And to Nils, Ziyun, Zhaojun and Jake, the perovskites fellows, thank you for being such a welcoming group, and for the sample, even if it had little to do with my own work. I would especially like to thank Zhaojun for helping me so much when you did not have to. Also, I would like to thank Aksel, my master student, who have been both support and inspiration.

SLJUS has been a workplace full of great colleagues and a warm, welcoming atmosphere. I'm grateful for all the fika, kick-offs, barbeques, happy-hour beer and meals in the lunchroom. Thank you to Yuhe, Zisheng, Zhe, Yi, Lingjia, Runqing, Zesen, Rohit, Shilpa, Myrto, Julia, Ahmed, Yen-Po, Vidar, Nelia, Andrea, Alfred, Hanna, Eleni, Mehran, Oskar, Ulrike, Sandra, Emma…everyone at SLJUS for all the great times we spent together. Thanks to Patrik for being magical and funny, and to Josefine for your help with my reimbursements. I feel lucky to have worked here.

MAX IV felt like a second home to me, as most of my work was conducted there. I always enjoyed the nice atmosphere and inspiring environment, though I did occasionally complain about the food truck and the lack of a proper cafeteria. I would like to express my appreciation to the team at NanoMAX for their professional support throughout the years. I also want to thank Kim and Mira at ForMAX—Kim for hosting me during my secondment, and Mira for all the chats and mocha. Thanks as well to Weimin for the coffee chats while waiting during the experiments.

On a more personal level, I'm truly grateful to all my friends I met along the way who showed kindness, support, and friendship. With you, the stressful times became more bearable, the dark days felt a little brighter, and even the rain seemed to come to an end.

There are some people to whom I would especially like to express my sincere appreciation, for their unwavering support during my most difficult times. To Li, thank you for always being there when I doubted myself. To Zhiqiang, thank you for your inspiring words. To Boyan, thank you for all the walks. To Yue, thank you for being a good neighbor. To Kailun, cheers to all the whisky we have shared (and wasted). To Zhaomin, thank you for inviting me to lunches and the delicious mutton soup. To Yueqian, thank you for taking me out to explore the world. To Zhushan and Qifeng, thank you for the companionship, even if it was mostly online.

Last, and most importantly, I want to thank my parents and my sister. 谢谢你们，我爱你们。

Table of Contents

List of Publications

This thesis includes the following publications which are referred to as 'paper X' and their Roman numerals:

I. Nanoscale X-ray imagine of composition and ferroelastic domains in heterostructured perovskite nanowires: implications for optoelectronic devices

S. Hammarberg, L. A. B. Marçal, N. Lamers, Z. Zhang, **H. Chen**, A. Björling, and J. Wallentin

ACS Applied Nano Materials, 6(19): p. 17698-17705 (2023).

https://doi.org/10.1021/acsanm.3c02978

I contributed to the experimental work, discussion about the data analysis and the editing of the manuscript.

II. Electrode modified domain morphology in ferroelectric capacitors revealed by X-ray microscopy

M.O. Hill Landberg, B. Yan, **H. Chen**, E. Ipek, M. Trassin, and J. Wallentin

Submitted

I contributed to the experimental work, the data analysis and the editing of the manuscript.

III. Correcting angular distortion in Bragg coherent X-ray diffraction imaging

H. Chen, D. Dzhigaev, A. Björling, F. Westermeier, M. Lyubomirskiy, M. Stuckerberger, and J. Wallentin

Journal of Synchrotron Radiation, 31(5): p. 1308-1316 (2024)

https://doi.org/10.1107/S1600577524006507

I was the main responsible for the algorithm design, coding and simulation, and I prepared the figures and wrote the manuscript

IV. 3D strain imaging of a heterostructured GaInP/InP nanowire using Bragg coherent diffraction X-ray imaging: implications for optoelectronic devices

H. Chen, M. O. Hill, M. Borgström, and J. Wallentin

ACS Applied Nano Materials, 8(5): p. 2310-2318 (2025)

https://doi.org/10.1021/acsanm.4c06406

I was the main responsible for the beamtime experiment, analysed the presented data, prepared the figures and wrote the manuscript.

V. Bragg coherent diffraction X-ray imaging of nanoparticles with unknown orientation

H. Chen, A. Mihailov, A. Björling, J. Solla-Gullón, and J. Wallentin

Manuscript in preparation

I was the main responsible for the algorithm including coding and simulation, analysed and imaged the presented data and wrote the manuscript.

Publications not included in this thesis, to which I contributed during my PhD:

VI. Water nanochannels in ultrathin clinochlore phyllosilicate mineral with ice-like behavior
R. de Oliveira, L. V. C. Freitas, H. Chacham, R. O. Freitas, R. L. Moreira, **H. Chen**, S. Hammarberg, J. Wallentin, G. Rodrigues-Junior, L. A. B. Marçal, G. A. Calligaris, A. R. Cadore, K. Krambrock, I. D. Barcelos, and A. Malachias
Journal of Physical Chemistry C, 128(34): p. 14388-14398 (2024)

VII. Ferroelectricity in ultrathin HfO_2-based films by nanosecond laser annealing
R. Athle, M. O. Hill, A. Irish, **H. Chen**, R. Timm, E. Kristensson, J. Wallentin, and M. Borg
ACS Applied Materials & Interfaces, 16(41): p. 55684–55692 (2024)

VIII. Effects of local compositional heterogeneity in mixed halide perovskites on blue electroluminescence
X. Luo, W. Xu, G. Zheng, S. Tammireddy, Q. Wei, M. Karlsson, Z. Zhang, K. Ji, S. Kahmann, C. Yin, Y. Zou, Z. Zhang, **H. Chen**, L. A. B. Marçal, H. Zhao, D. Ma, D. Zhang, Y. Lu, M. Li, C. Deibel, S. D. Stranks, L. Duan, J. Wallentin, W. Huang, and F. Gao
Matter, 7(3): p. 1054-1070 (2024)

IX. Structural and chemical properties of anion exchanged $CsPb(Br_{(1-x)}Cl_x)_3$ heterostructured perovskite nanowires imaged by nanofocused x-rays
L. A. B. Marçal, N. Lamers, S. Hammarberg, Z. Zhang, **H. Chen**, D. Dzhigaev, M. A. Gomez-Gonzalez, J. E. Parker, A. Björling, A. Mikkelsen, and J. Wallentin
Nanotechnology, 35(26), 265710 (2024)

X. Oxygen-defective electrostrictors for soft electromechanics
V. B. Tinti, J. K. Han, V. Frederiksen, **H. Chen**, J. Wallentin, I. Kantor, A. Lyksborg-Andersen, T. W. Hansen, G. Bae, W. Song, E. Stamate, D. Z. de Florio, H. Bruus, and V. Esposito
Science Advances, 10(35), eadq3444. (2024)

XI. Electromechanical coupling in polaronic ceria
V. B. Tinti, M. Vasiljevic, M. Grønborg, **H. Chen**, V. Frederiksen, I. Kantor, J. Wallentin, and V. Esposito
Journal of Physics: Energy, 7(3) 035002 (2025)

Popular Science Abstract

When you visit dentist to check for cavities, sit for a medical CT scan, or pass through airport security, you are likely encountering the capacity of *X-rays*. At the dentist, X-rays help detect decay inside the teeth before it becomes visible on the surface. In the hospital, computed tomography (CT) scans, allow doctors to peer inside the human body, identifying everything from broken bones to tumors without surgery. At airports, your luggage is scanned using an X-ray machine to check for hidden items, all without opening your bag. Even in manufacturing, X-rays are used for quality control.

X-rays are a powerful tool and widely used in our daily life. What makes this invisible light so versatile? They have such a high energy that they can pass through most materials. This property allows X-rays to reveal the internal structures of objects without opening them.

So far, these examples focused on large-scale objects, like your teeth, bones or luggage. But thanks to breakthroughs in synchrotron radiation and advanced X-ray optics, we can now use X-rays to examine much smaller systems, down to the nanoscale. Understanding the internal structure of these tiny materials is critical, not only for science but also for the technologies we rely on every day. Devices like LEDs, solar cells, and the microchips in our phones and computers are built from nanostructured components, such as nanowires, quantum dots, and thin films, whose internal arrangements directly affect performance of devices.

However, imaging these small structures is extremely challenging. The resolution of conventional imaging is limited by how tightly we can focus the X-ray beam. To go beyond this limit, we turn to a powerful technique: X-ray diffraction. When X-rays interact with a crystal, they scatter off the atoms and interfere with each other to form a diffraction pattern. Just as visible light bends when it passes through a lens, X-rays experience similar shifts depending on how atoms are arranged inside the crystal. These subtle changes are captured in the diffraction pattern, which acts like a fingerprint of the internal structure. Rather than performing a direct image, we analyze the diffraction to reconstruct the structure of the crystal.

A single diffraction pattern represents only a projection of the object from one direction. To access the full internal structure, sampling of full three-dimensional diffraction pattern is necessary. However, any instability during the sampling can distort the diffractions and thus lead to the inaccurate results.

In my PhD project I have worked on mainly two topics, employing X-ray diffraction imaging techniques to characterize crystalline materials, such as thin films, isolated particles and nanowires, and developing methods to find the unknown angles of diffraction data. Together, these efforts demonstrate the potential of synchrotron-based X-ray diffraction imaging techniques in revealing the internal structure of small-scale crystalline materials. The results of my work are summarized in my publications and explored throughout this thesis.

1 Introduction

Understanding the internal structure of crystalline materials is essential for tailoring their properties and driving technological innovation. In semiconductors, lattice mismatch can shift electronic band structures, altering conductivity and optical behavior. In ferroelectric materials, domain configurations govern switching performance, which is crucial for memory and sensing applications. Even in catalysis, nanoscale lattice distortions can dramatically impact reaction kinetics. Across these examples, subtle variations in the crystal lattice, often hidden beneath the surface, play an important role in how materials function.

X-rays have emerged as a powerful and promising tool to access such internal structural information in materials. Their short wavelength makes them ideally suited for resolving atomic-scale features, while their high penetration depth allows them to probe thick samples. Compared to transmission electron microscopy (TEM), which offers atomic resolution but often requires destructive sample preparation such as thinning or sectioning, X-ray diffraction imaging can probe the internal structure of materials in a non-destructive manner.

When X-rays interact with a crystalline material, they scatter in well-defined directions determined by the lattice periodicity, producing a diffraction pattern. This pattern encodes information about the arrangement of atoms, and any displacement, strain, or tilt within the lattice inherently raises variation in diffraction intensity.

This thesis presents two advanced X-ray diffraction imaging techniques developed to extract nanoscale structural information: Scanning X-ray diffraction imaging (nano-XRD) and Bragg coherent diffraction imaging (BCDI). Both techniques rely heavily on the modern synchrotron radiation sources, which deliver extremely bright and coherent X-ray beams.

The first technique, nano-XRD, involves scanning a highly focused X-ray beam across a sample and recording diffraction patterns at each point. By analyzing the subtle shifts in the Bragg peak positions, this method enables quantitative mapping of lattice parameters such as strain and tilt. It is especially suited for extended materials and enables imaging of hidden domains, such as ferroelectric patterns beneath metallic electrodes, which are inaccessible to conventional probes like piezoresponse force microscopy (PFM). The advanced nano-focusing optics available at synchrotrons push the resolution of nano-XRD imaging down to tens of nanometers.

The second technique, BCDI employs a coherent beam to illuminate the sample and collects the full 3D diffraction pattern surrounding a selected Bragg peak. Using iterative phase retrieval algorithms, the complex-valued electron density volume is reconstructed, providing access to both the morphology and internal displacement field of the crystal at high resolution.

Despite its powerful capabilities, BCDI is particularly sensitive to experimental instabilities and assumes perfect control of the angle of the nanocrystals, but in reality, angular distortions introduced during data acquisition can introduce artifacts in reconstruction. Even worse, these challenges are more severe for smaller nanocrystals and for more intense X-ray beams. This issue limits the broader applicability of BCDI, especially in complex or in situ experimental environments.

A significant portion of this thesis is therefore focused on addressing the challenge of different levels of angular distortions. One central contribution involves the development of a robust angular correction algorithm capable of mitigating the effects of angular distortions in BCDI datasets, thereby improving data quality and reconstruction fidelity.

The final contribution aims to handle data with fully unknown angles. In this case, deep learning is used for its strong ability to handle complex data due by learning representation directly form the given data. This offers an alternative solution to the challenges posed by angular uncertainties in BCDI. Rather than correcting angular uncertainties explicitly, the proposed approach uses deep learning to reconstruct the diffraction volume directly from randomly sampled data. In principle, this strategy can relax the strict experimental constraints of BCDI and ultimately broaden its applicability to more complex or dynamic experimental environments.

The remainder of the thesis is organized as follows:

Chapter 2 introduces the fundamentals of X-ray diffraction. This chapter describes fundamentals of X-ray scattering with crystalline materials, which establishes the theoretical framework for nano-XRD and BCDI.

Chapter 3 provides an overview of synchrotron light sources, and the experimental configuration used for nano-XRD and BCDI. Specifically, the data analysis procedures for both techniques are introduced in this chapter.

Chapter 4 presents the projects utilizing nano-XRD, corresponding to Paper I & II.

Chapter 5 focuses on the projects based on BCDI and the angular correcting algorithm, related to Paper III & IV.

Chapter 6 introduces the project employing deep learning techniques, including a brief overview of the underlying methods. This chapter corresponds to Paper V.

2 Fundamentals of X-ray Diffraction

Our eyes allow us to perceive and interpret the world by capturing light. This interaction with light provides us with understanding and insight into our surroundings. However, light, as an electromagnetic wave, spans a far broader range of wavelengths than the human eye can detect. Beyond visible light, there exists an invisible spectrum that includes radio waves, microwaves, infrared, ultraviolet, X-rays, and gamma rays, each revealing unique aspects of the universe. Today, these invisible forms of light are widely utilized to explore the world and improve the convenience and quality of our daily lives.

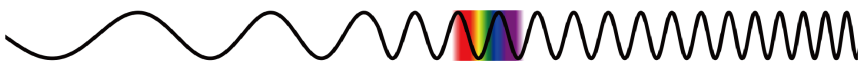

	Radio	Microwave	Infrared	Visible	Ultraviolet	X-ray	Gamma
Wavelength λ [m]	10^{3}	10^{-2}	10^{-5}	10^{-6}	10^{-8}	10^{-10}	10^{-12}
Energy E [eV]	10^{-9}	10^{-4}	10^{-1}	10^{1}	10^{2}	10^{4}	10^{6}

Figure 2.1 The electromagnetic spectrum. From left to right, the wavelengths of electromagnetic waves decrease, while their energy increases. X-rays are positioned on the high-energy side of the spectrum, between ultraviolet and gamma rays.

Among these, X-rays, located on the high-energy side of the electromagnetic spectrum as shown in Figure 2.1, hold a special place for their unique properties. They were firstly discovered by Wilhelm C. Röntgen in 1895. To his surprise, this new radiation[1] could easily pass through his hand, revealing the internal bone structure. Röntgen named it "X-ray" due to its unknown nature at the time. Shortly thereafter, scientists recognized X-rays as an ideal tool for characterizing microscopic materials because of their short wavelengths, high energy, and exceptional penetration ability.

The wavelengths of X-rays cover a range from 10 nm to 0.1 Å, which is comparable to the size of atoms. The relation between the energy E (in kilo electron volts, keV) and the wavelength λ (in Å) can be described as[2]:

$$E = \frac{hc}{\lambda} \approx \frac{12.398}{\lambda[\text{Å}]}\ [keV], \tag{2.1}$$

where h is Plank's constant, and c is the speed of light in vacuum. Therefore, X-rays have an energy range between 0.1 to 100 keV. This is high enough to ionize the core electrons of atoms.

Based on their wavelength, X-rays are classified into two categories: Hard X-rays with shorter wavelengths, and soft X-rays with longer wavelengths. The shorter wavelength and higher energy of hard X-rays provide superior penetration ability, making them suitable for non-destructive investigations of internal structure. Throughout this thesis, hard X-rays are employed as the primary tool for studying the internal structure of microscale objects.

In this chapter, I introduce the fundamentals of X-ray diffraction and demonstrate its application in studying the internal structure of materials. The chapter is organized into three sections: fundamentals of X-ray scattering, diffraction from an ideal crystal, and diffraction from a crystal with strain. The first section provides an overview of how X-rays interact with matter. The second section delves into the principles of X-ray scattering from crystallized materials with a perfect lattice, explaining how diffraction patterns are formed. The final section focuses on how diffraction patterns encode the internal structure of the scattered crystal.

2.1 Fundamentals of X-ray Scattering

Electromagnetic radiation, including X-rays, is considered as continuous waves in the classical framework. In this thesis, I adopt the *scalar wave approximation* to describe X-ray propagation, which simplifies the treatment by neglecting all polarization effects and using a scalar wave instead of the full electromagnetic vector field. The behavior of the scalar wave ψ is governed by the *scalar wave equation* (d'Alembert equation), which can be derived from Maxwell's equations[3].

The time-dependent scalar wave equation in vacuum is

$$\left(\nabla^2 - \frac{1}{c^2}\frac{\partial^2}{\partial t^2}\right)\ \psi(x,y,z;t) = \ 0. \tag{2.2}$$

Here, $\psi(x,y,z;t)$ is the wave function of time t and position (x,y,z) in three-dimensional (3D) space, and ∇ is the Laplacian operator.

A basic solution to this equation is the *plane wave*:

$$\psi(\boldsymbol{r};t) = \psi_0 \exp(i\boldsymbol{kr}) \exp(-i\omega t)\,. \tag{2.3}$$

In this expression, and throughout this thesis, $\boldsymbol{r} = (x,y,z)$ is the position vector and ψ_0 is the amplitude. This equation describes a wave of frequency ω propagating in

the direction of the wavevector $\boldsymbol{k}$. The magnitude of the wavevector $\boldsymbol{k}$ is given by $k = |\boldsymbol{k}| = \frac{2\pi}{\lambda} = \frac{\omega}{c} = \frac{E}{\hbar c}$, which links the wavelength λ and the energy E. The intensity of the plane wave is equal to the square of its amplitude: $I_0 = |\psi_0|^2$. Here, $\boldsymbol{kr}$ denotes the scalar (dot) production of wavevector $\boldsymbol{k}$ and position vector $\boldsymbol{r}$. For simplicity, the dot symbol "·" is omitted. This notation will be used consistently throughout the remainder of the thesis.

Electromagnetic waves also exhibit the wave-particle duality, meaning that they have particle-like properties in addition to the wave properties discussed so far. In the particle picture, X-rays are also described as a stream of photons traveling along the direction $\boldsymbol{k}$, with each photon carrying energy of E and momentum $\boldsymbol{p} = \hbar\boldsymbol{k}$. In practice, modern X-ray detectors measure the discrete arrival of these photons, recording *photon counts* rather than continuous wave amplitudes. In this context, the measured intensity corresponds to the number of photons detected per pixel per unit time.

Moving forward, I will use both descriptions interchangeably, depending on which is most suitable for the explanation.

2.1.1 Microscopic View: Absorption and Scattering

For an individual atom, X-rays primarily interact with its electrons. These interactions can be categorized into four processes[2]: *photoelectric absorption*, *incoherent scattering, coherent scattering* and *pair production*. Since pair production predominantly occurs at photon energies well above the typical X-ray range used in this thesis, it will be neglected in the following discussion. The element-specific *cross sections*, as illustrated in Figure 2.2, represent the likelihood for these interactions as a function of energy.

The photoelectric absorption describes the process in which an X-ray photon is absorbed by an atom. As shown in Figure 2.2, photoelectric absorption dominates at low radiation energies. The cross section for this process is proportional to Z^{3-4}, where Z represents the atomic number, and proportional to the inverse incoming radiation energy ($1/E^3$).

When an X-ray photon is absorbed, its energy is transferred to a core electron, exciting it to the vacuum energy level and ejecting it as a *photoelectron*. This excitation leaves a vacancy (hole) in the inner shell (low energy state) and thus results in the ionization of the atom. The photon energy required to overcome the binding energy of a specific electron shell gives rise to an abrupt increase in cross section, known as an *absorption edge*, as shown in Figure 2.2. To restore a more stable state, an electron from an outer shell spontaneously de-excites to fill the vacancy. The energy released during this transition is either emitted as an *X-ray fluorescence* photon or transferred to another outer-shell electron, producing an

Auger electron. These secondary processes compete, and their relative likelihood depends on the atomic number (Z) of the element. Auger emission is dominant in low-Z elements, while fluorescence is more likely in high-Z elements (typically $Z \geq 30$)[4,5].

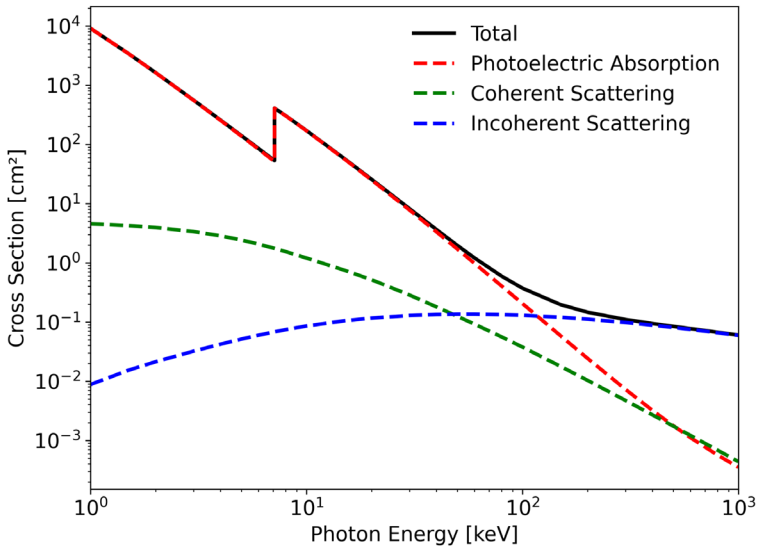

Figure 2.2 X-ray attenuation cross sections of iron (Fe) as a function of energy. The data, covering an energy range from 1 keV to 1000 keV, is obtained from the NIST database[6]. High-energy effects such as pair production are not included, as they occur beyond 1000 keV.

X-ray fluorescence (XRF) is a powerful tool for material characterization[7], as it can identify elements within a sample. When illuminated by incident X-rays, all elements with binding energies below the energy of incident beam will generate energy-specific fluorescence collected as an XRF spectrum, which can be used for precise elemental analysis. In this thesis, XRF has been utilized as a supporting tool for locating and aligning samples in various experiments.

In addition to being absorbed, X-ray photons can also be scattered by electrons, resulting in a change in their propagation direction $\boldsymbol{k}$. Incoherent scattering, also known as inelastic scattering, involves a change in the wavelength λ (and the energy E) of the outgoing X-rays compared to the incident X-rays. In contrast, coherent scattering is an elastic scattering process, meaning that the wavelength λ (and the energy E) remains unchanged during after scattering.

Inelastic scattering of X-rays by an electron is known as *Compton scattering*. The Compton scattering is inelastic, meaning that the energy (or wavelength) of incoming and outgoing X-rays differs. Due to the energy and momentum

conservation, energy is transferred between X-rays and scatterer (in this case, the electron) during inelastic scattering This interaction results in the angular dependence of the Compton scattering and the ejection of an electron, referred to as the *Compton recoil electron*.

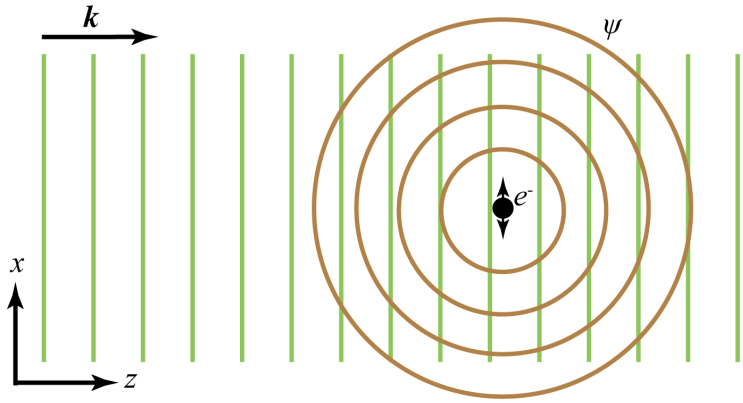

Figure 2.3 Illustration of X-ray scattering from a single free electron. The incident X-rays are shown as wave fronts of plane waves with linear polarization along the *x*-direction and propagation along the *z*-direction.

The coherent scattering with a free single electron is known as *Thomson scattering*. As shown in Figure 2.3, the incident X-rays are represented as plane waves with amplitude ψ_0, linearly polarized along the x- direction and propagating in the z-direction. The electric field component of the wave drives the electron to oscillate along the x- direction, acting as a radiating *dipole*. This oscillating electron emits secondary radiation in the form of spherical waves. The resulting scattered wave $\psi(\boldsymbol{r})$ observed at arbitrary angle α in the xz- plane at a distance r is given by[2]

$$\psi(\boldsymbol{r}) = -r_0 \frac{\psi_0 e^{i\boldsymbol{kr}}}{r} \cos\alpha\,, \tag{2.4}$$

where r_0 is the *Thomson scattering length*.

The factor $\cos\alpha$ can also be expressed as the scalar product of the polarization vectors of incident scattered wave, $\hat{\boldsymbol{\varepsilon}} \cdot \hat{\boldsymbol{\varepsilon}}'$, in the xz- plane. The scattering amplitude of Thomson scattering is then equal to $-r_0|\hat{\boldsymbol{\varepsilon}} \cdot \hat{\boldsymbol{\varepsilon}}'|$, which is independent of the incident photon energy. The negative sign arises from the negative charge of the electron, meaning that the scattered wave is 180° out of phase with the incident X-ray wave.

The coherent scattering from multiple bound electrons within an atom is known as the *Rayleigh scattering*. In this process, each electron scatters with the incident X-ray wave and contributes to the total scattered wave. To analyze this scenario, an important assumption, known as the *kinematical approximation*[2], is applied, which

states the scattering process occurs at most once for every incident photon, and secondary scattering events are negligible. Additionally, both incident and scattering waves are observed in the far-field region, where the *Fraunhofer approximation*[3] holds. Under these conditions, both the incoming and scattered X-rays can be treated as plane waves, characterized by the wavevector $\boldsymbol{k'}$ and $\boldsymbol{k}$, respectively. For coherent scattering, the magnitude of these wavevectors is equal, $|\boldsymbol{k}| = |\boldsymbol{k'}|$, but their directions differ.

Next, we consider a charge distribution. The *electron density* $\rho(\boldsymbol{r})$ describes probability of finding an electron at position $\boldsymbol{r}$ within the atom. Since the scattering is coherent, we have to consider the coherent addition of scattered waves, taking the phase into account. For an arbitrary electron located at position $\boldsymbol{r}$, the path difference relative to an electron at the origin introduces a phase shift:

$$\Delta\varphi(\boldsymbol{r}) = (\boldsymbol{k} - \boldsymbol{k'})\boldsymbol{r} = -\boldsymbol{Q}\boldsymbol{r}, \tag{2.5}$$

where $\boldsymbol{Q} = \boldsymbol{k'} - \boldsymbol{k}$ is the *scattering vector*, or the *momentum transfer vector*.

Each electron thus contributes to the scattered wave $\boldsymbol{k'}$ with a phase factor $e^{-i\boldsymbol{Q}\boldsymbol{r}}$, and the total scattering amplitude[2] from the atom is the sum over all such contributions, weighted by the electron density.

$$A(\boldsymbol{Q}) = -r_0 f(\boldsymbol{Q}) = -r_0 \int \rho(\boldsymbol{r}) e^{-i\boldsymbol{Q}\boldsymbol{r}}\, d\boldsymbol{r}, \tag{2.6}$$

where $f(\boldsymbol{Q})$ is known as the *atomic form factor*. As $|\boldsymbol{Q}| \to 0$, the phase factor $e^{-i\boldsymbol{Q}\boldsymbol{r}}$ approaches unity, and the integral yields the total number of electrons in the atom, $f(\boldsymbol{Q} = 0) = Z$.

Note that Eq. (2.6) shows that the scattering amplitude of an atom corresponds to the Fourier transform of its electron density $\rho(\boldsymbol{r})$, and this principle remains valid also when $\rho(\boldsymbol{r})$ represents a larger object, such as a unit cell or nanocrystal, within the approximations of kinematical scattering and Fraunhofer diffraction. This foundational result forms the theoretical basis for much of the work in this thesis.

Eq. (2.6) assumes that the scattering is purely elastic and that the atomic form factor $f(\boldsymbol{Q})$ is real and energy independent. However, when the incident X-ray photon energy near an absorption edge, the interaction becomes more complex and typically involves absorption. To account for this, the atomic form factor is extended to include energy-dependent *dispersion corrections*.

$$f(\boldsymbol{Q}, E) = f^0(\boldsymbol{Q}) + f'(E) + if''(E). \tag{2.7}$$

As illustrated in Figure 2.2, the cross section for elastic scattering is higher than that for inelastic scattering within the X-ray energy range of 0.1-50 keV.

2.1.2 Macroscopic View: Refractive Index

For macroscopic objects, the *complex refractive index* n is used to characterize the material's interaction with X-rays. It is defined as:

$$n = 1 - \delta + i\beta. \tag{2.8}$$

In the X-ray regime, the real part δ is typically on the order of 10^{-5} for solids, while the imaging part β is usually even much smaller[2].

The definitions of δ and β can be derived by comparing the mathematical description of the X-ray propagation in materials (using refractive index n) with the interaction of X-rays photons with multiple electrons within a given volume. They are given as

$$\delta = \frac{2\pi\rho_{at}r_0}{k^2}(f^0(0) + f'), \qquad \beta = -\frac{2\pi\rho_{at}r^0}{k^2}f'', \tag{2.9}$$

Definitions in Eq. (2.9) elegantly link the macro view and the micro view of the X-ray-matter interactions. The real part δ introduces a phase shift to the scattered wave and is associated with elastic scattering. The imaginary part β, on the other hand, accounts for absorptions within the material.

2.1.3 Coherence

In the previous sections, outgoing X-rays are described as the result of interference between the scattered waves from individual electrons. This process introduces one important concept in this thesis, *coherence*. Coherence refers to the ability of waves to maintain a consistent phase relationship, determining whether waves can interfere. This property is necessary for creating observable interference or diffraction patterns.

There are two types of coherence: *longitudinal/temporal coherence* and *transversal/spatial coherence*. Longitudinal coherence is related to the spectral bandwidth of the wave, which determines its degree of monochromaticity. Transversal coherence, on the other hand, depends on the uniformity of the wavefront and the direction of wave propagation. A simple threshold for defining the visibility of interference is the *coherence length*.

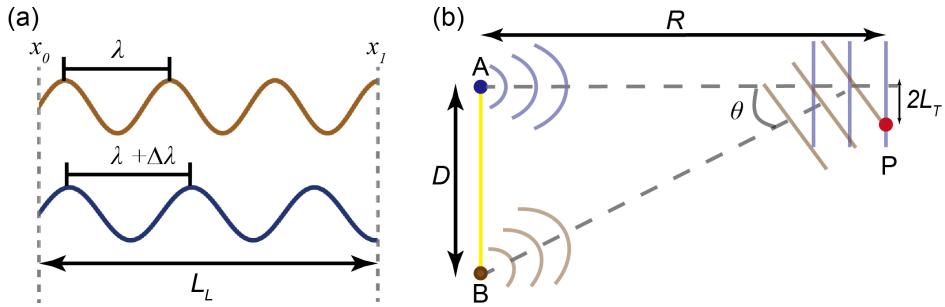

Figure 2.4 Illustration of longitudinal and transversal coherence. a) Longitudinal coherence, which is related to spectral bandwidth of the source. b) Transversal coherence, which arises from the finite size of the source.

As shown in Figure 2.4(a), consider two waves with slightly different wavelengths, λ and $\lambda + \Delta\lambda$, propagating along the x- direction. At the point x_0, they are in-phase. The longitudinal coherence length quantifies the distance over which two waves become completely out-of-phase (phase difference of π):

$$L_L = \frac{\lambda^2}{2\Delta\lambda}. \tag{2.10}$$

Now, consider a finite light source, as illustrated in Figure 2.4(b). Points A and B on the source are separated by a distance of D. Waves emitted from these two points propagate in different directions. At the observation point P, the waves are in-phase. The transversal coherence length defines the distance from P to the position where they are completely out-of-phase:

$$L_T = \frac{\lambda R}{2D}. \tag{2.11}$$

Together, longitudinal and transversal coherence lengths form the *coherence volume* V_c. The coherence volume V_c represents the maximum scale that waves remain coherent or partially coherent and thus contribute to the interference patterns. Beyond this volume, incoherent waves will blur and even eliminate the interference fringes. For X-ray diffraction imaging techniques, as discussed in this thesis, it is vital that the sample is within the coherence volume of the incoming X-ray beam.

2.2 Diffraction from an Ideal Crystal

The previous section demonstrated that, in the X-ray regime, the scattering amplitude is proportional to the Fourier transform of the object's electron density $\rho(\boldsymbol{r})$. In the following section, I will focus on materials with periodic structure, known as *crystals*, and explore how their symmetry and periodicity influence the X-ray diffraction.

2.2.1 Crystal Structure: Lattice in Direct and Reciprocal Space

For perfectly crystalline materials, the distribution of atoms can be represented as a regular, repeating grid, known as a *crystal lattice*. There are two types of crystalline materials: *single crystals* and *polycrystals*. A single crystal refers to the material in which the entire structure shares the same crystal lattice and orientation. In contrast, polycrystalline materials consist of multiple grains, where each grain varies in size and has different orientation of the crystal lattice.

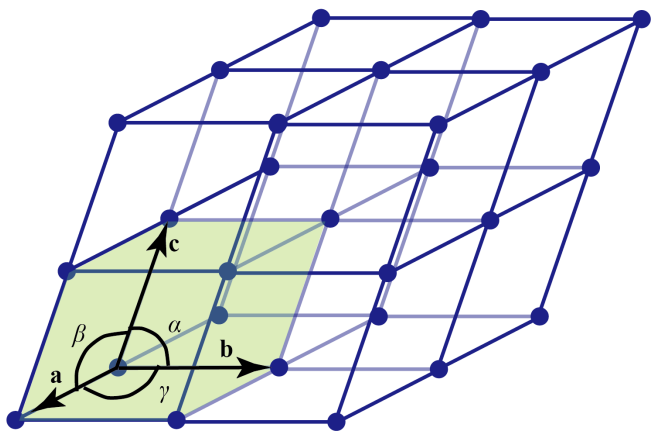

Figure 2.5 An ideal crystal lattice with basis vectors. The shaded volume is a crystal unit cell, in which a single-atom basis is assumed for simplicity.

As shown in Figure 2.5, the entire crystal lattice is constructed from many identical blocks called *unit cells*. Each unit cell contains the identical fundamental components that make up the crystal. The lattice vector of the n-th unit cell can be represented as:

$$\boldsymbol{R}_n = u\boldsymbol{a} + v\boldsymbol{b} + w\boldsymbol{c}, \tag{2.12}$$

where $(\boldsymbol{a}, \boldsymbol{b}, \boldsymbol{c})$ are the basis vectors of a unit cell and (u, v, w) are corresponding integer factors. The length of basis vectors $(\boldsymbol{a}, \boldsymbol{b}, \boldsymbol{c})$ called *lattice constants* represent the lattice spacings along each axis of the crystal lattice. In general, $(\boldsymbol{a}, \boldsymbol{b}, \boldsymbol{c})$ might not be mutually perpendicular, and the angles between them are denoted as (α, β, γ). The volume of a single unit cell can be calculated as $V^{\mathrm{uc}} = \boldsymbol{a} \cdot (\boldsymbol{b} \times \boldsymbol{c})$.

An ideal infinite crystal lattice can be mathematically expressed as a Dirac comb function

$$|||(\boldsymbol{r}) = \sum_n \delta(\boldsymbol{r} - \boldsymbol{R}_n)\,. \tag{2.13}$$

The Fourier transform of the lattice results in another lattice, known as the *reciprocal lattice*. Based on its definition, the basis vectors of the reciprocal lattice are given by

$$\boldsymbol{a}^* = 2\pi \frac{\boldsymbol{b} \times \boldsymbol{c}}{V^{\mathrm{uc}}}, \boldsymbol{b}^* = 2\pi \frac{\boldsymbol{c} \times \boldsymbol{a}}{V^{\mathrm{uc}}}, \boldsymbol{c}^* = 2\pi \frac{\boldsymbol{a} \times \boldsymbol{b}}{V^{\mathrm{uc}}}. \tag{2.14}$$

Naturally, the basis vectors in real and reciprocal space satisfy the reciprocal relationship $\boldsymbol{a} \cdot \boldsymbol{a}^* = 2\pi$. Thus, the reciprocal lattice vector $\boldsymbol{H}_{hkl}$ constructed from these basis vectors is defined as

$$\boldsymbol{H}_{hkl} = h\boldsymbol{a}^* + k\boldsymbol{b}^* + l\boldsymbol{c}^*, \tag{2.15}$$

where hkl are the *Miller integer indices*. In crystallography, the Miller indices are used to denote specific lattice directions and its corresponding sets of planes within the crystal.

The distance between $\{hkl\}$ planes is called the *d-spacing*, denote d_{hkl}. The relationship between d-spacing and its corresponding lattice vector $\boldsymbol{H}_{hkl}$ is

$$d_{hkl} = \frac{2\pi}{|\boldsymbol{H}_{hkl}|}. \tag{2.16}$$

2.2.2 X-ray Scattering from a Finite Crystal

The discussion so far has assumed an infinite crystal, but real crystals are finite. The real *shape function* $m(\boldsymbol{r})$ is introduced here to describe the shape of the crystal:

$$m(\boldsymbol{r}) = \begin{cases} 1, & \boldsymbol{r} \in V, \\ 0, & \boldsymbol{r} \notin V, \end{cases} \tag{2.17}$$

where V is the volume of the crystal.

The electron density $\rho(\boldsymbol{r})$ of the finite crystal can then be mathematically expressed as the product of the crystal lattice and the shape function[8]

$$\rho(\boldsymbol{r}) = \rho_{uc}(\boldsymbol{r}) \otimes [|||(\boldsymbol{r}) \cdot m(\boldsymbol{r})]. \tag{2.18}$$

Here, symbol $\otimes$ denotes the convolution operation. ρ_{uc} is the electron density of a single unit cell, given by summing over all atoms in the unit cell.

$$\rho_{uc}(\boldsymbol{r}) = \sum_j \rho_j(\boldsymbol{r} - \boldsymbol{R}_j), \tag{2.19}$$

with $\rho_j(r)$ representing the electron density of the j-th atom and $\boldsymbol{R}_j$ being the position vector of the j-th atom in the unit cell. Adopting the definition of atomic form factor $f(\boldsymbol{Q})$ in Eq. (2.6), the *unit cell structure factor*[2] is given by the Fourier transform of $\rho_{uc}(\boldsymbol{r})$.

$$F^{\mathrm{uc}}(\boldsymbol{Q}) = \sum_j^{\text{atoms}} f_j(\boldsymbol{Q}) e^{i\boldsymbol{Q}\cdot\boldsymbol{R}_j}, \tag{2.20}$$

Finally, the total scattering amplitude from a finite crystalline material is obtained by taking the Fourier transform of its electron density $\rho(\boldsymbol{r})$. This results in:

$$\begin{aligned} A(\boldsymbol{Q}) &= F^{\mathrm{uc}}(\boldsymbol{Q}) \cdot \widehat{|||}(\boldsymbol{Q}) \otimes \hat{m}(\boldsymbol{Q}) \\ &= \underbrace{\sum_j f_j(\boldsymbol{Q}) e^{-i\boldsymbol{Q}\cdot\boldsymbol{R}_j}}_{\text{Unitcell}} \cdot \underbrace{\left[\frac{(2\pi)^3}{V^{\mathrm{uc}}} \sum_{hkl} \delta(\boldsymbol{Q} - \boldsymbol{H}_{hkl})\right]}_{\text{Lattice}} \otimes \hat{m}(\boldsymbol{Q}), \end{aligned} \tag{2.21}$$

where $\hat{m}(\boldsymbol{Q})$ is the Fourier transform of the real shape function $m(\boldsymbol{r})$.

2.2.3 Laue Condition, Bragg's Law and Ewald's Sphere

Eq. (2.23) demonstrates that the diffraction pattern of a finite crystal arises from the coherent superposition of waves scattered from atoms at each lattice point. It reflects the combined contribution from the unit cell structure, the crystal lattice periodicity and the overall shape of the crystal.

Laue Condition

Let's us examine the lattice part in Eq. (2.21). Diffraction occurs when

$$\boldsymbol{Q} = \boldsymbol{H}_{hkl}, \tag{2.22}$$

as the scattering from all unit cells are in phase. This condition is known as the *Laue condition*[9], and the resulting maxima in intensity are referred to as the *Bragg peaks*. At these points, the intensity of the diffraction pattern is determined by the combined contributions of the unit cell structure factor and the shape function.

Bragg's Law

The magnitude of the momentum transfer vector $\boldsymbol{Q}$ can be calculated as

$$Q = |\boldsymbol{Q}| = |\boldsymbol{k} - \boldsymbol{k}'| = 2k \sin\theta\,, \tag{2.23}$$

where θ is the half-angle between wave vectors $\boldsymbol{k}$ and $\boldsymbol{k}'$. When the Laue condition (Eq. (2.22)) is satisfied, substituting Eq. (2.16) into Eq. (2.23) yields *Bragg's law*[10]:

$$\mathrm{n}\lambda = 2d_{hkl} \sin\theta_B\,. \tag{2.24}$$

From the perspective of traditional optics, Bragg' law[2] describes the condition for maintaining an in-phase relationship between the parallel waves incident on a crystalline material orientated along the $[hkl]$ direction, as illustrated in Figure 2.6. It specifies the angle θ_B, known as the *Bragg angle*, at which the selected Bragg peak appears. The direction associated with the Bragg angle is also referred to as the *rocking direction*. Bragg's law is a fundamental concept in X-ray diffraction and is widely used in crystal structure analysis.

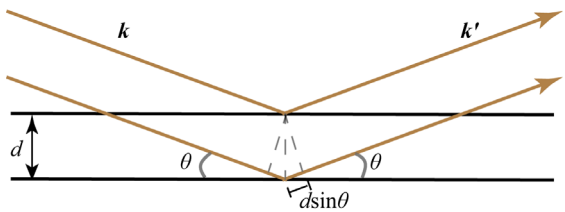

Figure 2.6 Illustration of Bragg's law. Two parallel incident X-rays illuminates planes separated by a spacing with d at an angle θ. The X-rays are in-phase at the initial point. The dashed-line triangles demonstrates the optical path difference between scattered waves.

Ewald's Sphere

The Laue condition requires the Bragg peak appear at the reciprocal lattice points, while the Bragg's law specifies the scattering geometry needed to select a target Bragg peak. Together, these principles describe where and how diffraction occurs within a crystalline material. However, visualizing the relationship between the

reciprocal lattice and the scattering geometry can be challenging. *Ewald's sphere*[11] provides a practical and intuitive tool for this purpose. It represents the diffraction condition in reciprocal space, illustrating how the orientation of the crystal and the wavelength (or energy) of the X-ray influence which reciprocal lattice points satisfy the principles and result in Bragg peaks.

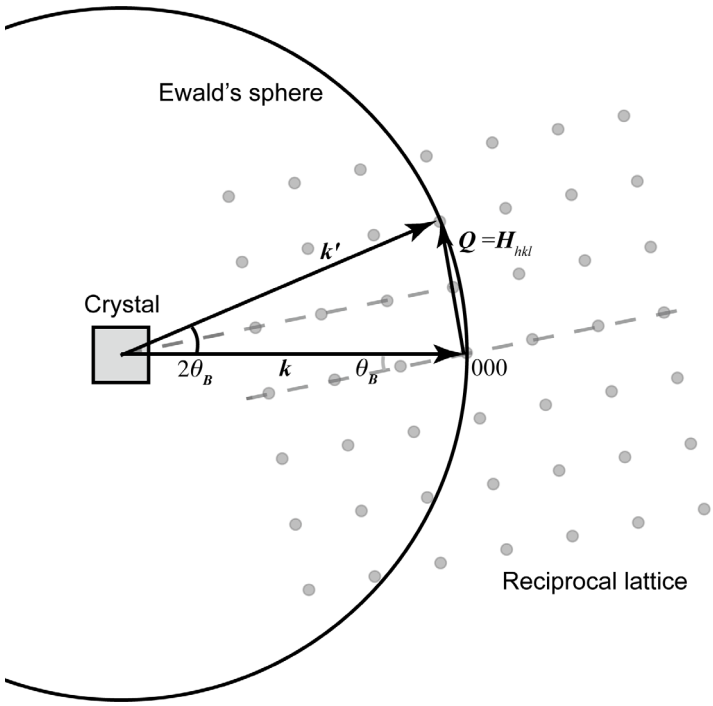

Figure 2.7 Illustraction of the Ewald's sphere. Gray dots represent the reciprocal lattice points, with the origin at [000]. The incoming wavevector $\boldsymbol{k}$ and outgoing wavevector $\boldsymbol{k}'$ define the scattering vector $\boldsymbol{Q}$.

Ewald's sphere is defined as a spherical shell with its radius equal to the magnitude of the wavevector $k = 2\pi/\lambda$. In 2D, it is represented as a circle as shown in Figure 2.7. The incoming wave vector $\boldsymbol{k}$ points at the origin [000] of the reciprocal lattice. As the crystal is rotated in the rocking direction, the reciprocal lattice also rotates around the origin. When the Ewald's sphere intersects a reciprocal lattice point $[hkl]$, the momentum transfer $\boldsymbol{Q}$ satisfied the Laue condition, and the angle between $\boldsymbol{k}$ and $\boldsymbol{k}'$ is twice the Bragg angle. The geometry defined by this intersection specifies the experimental parameters, including the rotation angle of the sample and detector position, required for measuring the target Bragg peak.

2.3 Diffraction from a Crystal with Strain

So far, the discussion has focused on a perfect crystal, where the lattice remains undistorted. However, such a perfect crystalline material is nearly impossible to be realized physically. Even slight displacements of lattice points naturally disrupt the periodic order, leading to local distortions that can significantly affect material properties, such as energy state, charge carrier mobility, and other physical parameters. Therefore, understanding the internal structure and imperfections of crystalline materials has become a central topic in modern solid-state physics and chemistry. The following section explores how these displacements alter diffraction patterns.

2.3.1 Deformation, displacement and strain

In physics, *deformation* is defined as changes in position and shape of a body. In the context of a crystal lattice, deformation primarily refers to variations in atomic positions within the ordered structure. Factors such as *strain*, ferro-elasticity and ferro-electric domains cause the distort the lattice order. Such a deformation is mathematically described by the *displacement field*[2]:

$$\boldsymbol{u}(\boldsymbol{r}) = \boldsymbol{R}'_n - \boldsymbol{R}_n, \tag{2.25}$$

where $\boldsymbol{R}_n$ represents the ideal lattice positions, and $\boldsymbol{R}'_n$ denotes the actual atomic positions in the deformed crystal lattice. The displacement field $\boldsymbol{u}(\boldsymbol{r}) = (u_x, u_y, u_z)$ captures the local shift at each lattice point in the crystal.

During X-ray scattering, a non-zero displacement field $\boldsymbol{u}(\boldsymbol{r})$ induces additional phase shift in the scattered wave, given by:

$$\varphi(\boldsymbol{r}) = -\boldsymbol{Q} \cdot \boldsymbol{u}(\boldsymbol{r}). \tag{2.26}$$

This phase shift represents the projection of the displacement field $\boldsymbol{u}(\boldsymbol{r})$ onto the scattering vector $\boldsymbol{Q}$. According to the Laue condition, diffraction occurs only when $\boldsymbol{Q}$ coincides with a lattice vector $\boldsymbol{H}_{hkl}$. Therefore, in X-ray scattering, the projection of the displacement field is directly encoded in the phase of the diffracted wave, which will be discussed in detail later.

The degree of deformation can be quantified by strai*n*, which is generally defined as the relative displacement of points within the crystal lattice. Considering the phase term defined in Eq. (2.26), the strain component along the x- direction as an example can be derived as

$$\varepsilon_{xx} = \frac{\partial u_x}{\partial x} = \frac{1}{|\boldsymbol{H}_{hkl}|}\frac{\partial \varphi}{\partial x} \tag{2.27}$$

If the lattice spacing d along a specific direction $[hkl]$ is known, the corresponding strain can also be calculated as

$$\varepsilon = \frac{d_s - d_0}{d_0}, \tag{2.28}$$

where d_s is the strained lattice parameter and d_0 is the ideal lattice parameter.

2.3.2 X-ray Scattering from a Finite Crystal with Strain

To account for the effect of strain, the shape function in Eq. (2.21) is modified to a complex form[12] with a phase term defined in Eq. (2.26):

$$s(\boldsymbol{r}) = m(\boldsymbol{r})e^{i\varphi(\boldsymbol{r})} = m(\boldsymbol{r})e^{-i\boldsymbol{Q}\boldsymbol{u}(\boldsymbol{r})}. \tag{2.29}$$

Inserting Eq. (2.29) into Eq. (2.21), the scattering amplitude is derived as[13]

$$\begin{aligned} A(\boldsymbol{Q}) &= F^{\mathrm{uc}}(\boldsymbol{Q}) \cdot \widehat{\coprod\coprod\coprod}(\boldsymbol{Q}) \otimes \hat{s}(\boldsymbol{Q}) \\ &= \sum_j f_j(\boldsymbol{Q}) e^{-i\boldsymbol{Q}\cdot\boldsymbol{R}_j} \cdot \left[\frac{(2\pi)^3}{V^{\mathrm{uc}}} \sum_{hkl} \delta(\boldsymbol{Q} - \boldsymbol{H}_{hkl})\right] \otimes \hat{s}(\boldsymbol{Q}) \\ &= \frac{(2\pi)^3}{V^{\mathrm{uc}}} \sum_j f_j(\boldsymbol{Q}) e^{-i\boldsymbol{Q}\cdot\boldsymbol{R}_j} \int \sum_{hkl} \delta(\boldsymbol{Q}' - \boldsymbol{H}_{hkl}) \hat{s}(\boldsymbol{Q} - \boldsymbol{Q}') d\boldsymbol{Q}' \\ &= \frac{(2\pi)^3}{V^{\mathrm{uc}}} \sum_j f_j(\boldsymbol{Q}) e^{-i\boldsymbol{Q}\cdot\boldsymbol{R}_j} \sum_{hkl} \int \delta(\boldsymbol{Q}' - \boldsymbol{H}_{hkl}) \hat{s}(\boldsymbol{Q} - \boldsymbol{Q}') d\boldsymbol{Q}' \\ &= \frac{(2\pi)^3}{V^{\mathrm{uc}}} \sum_j f_j(\boldsymbol{Q}) e^{-i\boldsymbol{Q}\cdot\boldsymbol{R}_j} \sum_{hkl} \hat{s}(\boldsymbol{Q} - \boldsymbol{H}_{hkl}) . \end{aligned} \tag{2.30}$$

The term $\hat{s}(\boldsymbol{Q} - \boldsymbol{H}_{hkl})$ is given by

$$\hat{s}(\boldsymbol{Q} - \boldsymbol{H}_{hkl}) = \int s(\boldsymbol{r}) e^{-i(\boldsymbol{Q} - \boldsymbol{H}_{hkl})\boldsymbol{r}} d\boldsymbol{r} . \tag{2.31}$$

Therefore, Eq. (2.30) becomes

$$A(\boldsymbol{Q}) = \frac{(2\pi)^3 F^{\mathrm{uc}}(\boldsymbol{Q})}{V^{\mathrm{uc}}} \sum_{hkl} s(\boldsymbol{r}) e^{-i(\boldsymbol{Q}-\boldsymbol{H}_{hkl})\boldsymbol{r}}\, d\boldsymbol{r}. \tag{2.32}$$

According to the Laue condition, the scattering vector is $\boldsymbol{Q} \approx \boldsymbol{H}_{hkl}$ in the vicinity of a selected Bragg peak along the specific $[hkl]$ direction. The deviation $\boldsymbol{q}$ from the Bragg peak can be introduced as $\boldsymbol{q} = \boldsymbol{Q} - \boldsymbol{H}_{hkl}$. At a given lattice point, the complex shape function[13] takes the form $s(\boldsymbol{r}) = m(\boldsymbol{r}) e^{-i\boldsymbol{H}_{hkl}\boldsymbol{u}(\boldsymbol{r})}$. Thus, the scattering amplitude around the selected Bragg peak is derived as

$$A(\boldsymbol{q}) = \frac{(2\pi)^3 F^{\mathrm{uc}}(\boldsymbol{Q})}{V^{\mathrm{uc}}} \int m(\boldsymbol{r}) e^{-i\boldsymbol{H}_{hkl}\boldsymbol{u}(\boldsymbol{r})}\, e^{-i\boldsymbol{q}\boldsymbol{r}} d\boldsymbol{r}. \tag{2.33}$$

The scattering intensity is defined as the absolute square of the scattering amplitude $A(\boldsymbol{q})$,

$$I(\boldsymbol{q}) = |A(\boldsymbol{q})|^2 = \left| \frac{(2\pi)^3 F^{\mathrm{uc}}(\boldsymbol{Q})}{V^{\mathrm{uc}}} \right|^2 \left| \int m(\boldsymbol{r}) e^{-i\boldsymbol{H}_{hkl}\boldsymbol{u}(\boldsymbol{r})}\, e^{-i\boldsymbol{q}\boldsymbol{r}} d\boldsymbol{r} \right|^2. \tag{2.34}$$

If for example $\boldsymbol{u}(\boldsymbol{r})$ is assumed to scale linearly with $\boldsymbol{r}$, i.e. for homogeneous and constant strain, the additional phase term $\exp(-i\boldsymbol{H}_{hkl}\boldsymbol{u}(\boldsymbol{r}))$ introduced by the displacement field can be interpreted as a linear phase ramp in real space. According to shift theorem of the Fourier transform, this corresponds to a shift of the diffraction pattern in reciprocal space. This relationship is expressed as:

$$\mathcal{F}\{\rho(\boldsymbol{r}) e^{-i\boldsymbol{q}\mathrm{d}\boldsymbol{r}}\} = \mathcal{F}\{\rho(\boldsymbol{q} + \mathrm{d}\boldsymbol{q})\}. \tag{2.35}$$

This property also holds in reverse. Higher-order variations in $\boldsymbol{u}(\boldsymbol{r})$, which is normally what we are interested in, give rise to more complex changes in the diffraction pattern.

Eq. (2.33) and Eq. (2.34) show that strain in a finite crystal introduces an additional phase term $\exp(-i\boldsymbol{H}_{hkl}\boldsymbol{u}(\boldsymbol{r}))$ at the Bragg peak along the selected $[hkl]$ direction. Figure 2.8 compares the simulated diffraction patterns for a perfect lattice and a strained lattice. As seen, the diffraction pattern from the perfect crystal exhibits central symmetry, consistent with Friedel's law[14]. In contrast, the presence of strain breaks the symmetry and introduces the local intensity variation in the diffraction pattern. Additionally, a slight shift in the Bragg peak happens.

By utilizing the sensitivity of X-ray diffraction to lattice displacements, X-ray diffraction imaging techniques provide critical insights into the internal structure and functional properties of crystal, especially in complex or integrated systems.

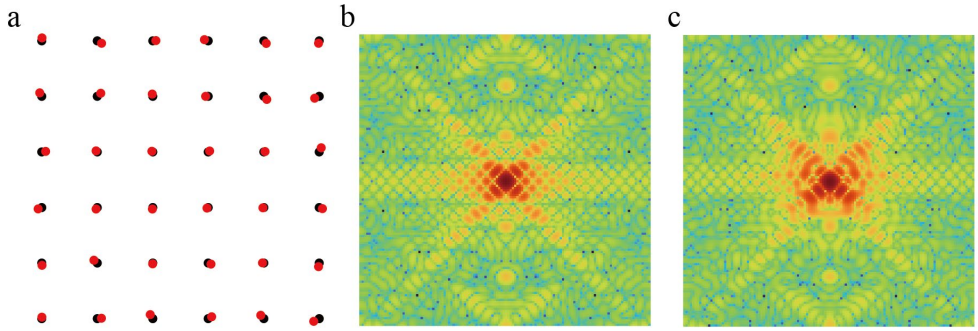

Figure 2.8 Simulated diffraction patterns from a perfect cubic crystal and a strained cubic crystal. a) Schematic illustration of the crystal lattices. The black lattice represents the perfect crystal, while the red lattice represents the strained crystal. b) Simulated diffraction pattern for a perfect crystal. c) Simulated diffraction pattern, displayed in logarithm, for the strained cubic crystal, with 2% strain applied in a harmonic distribution.

The theoretical framework introduced in this chapter is based on the kinematical approximation. This approximation is valid under the condition of weak scattering, typically satisfied in systems with small sample volumes or low atomic numbers. In this thesis, most of the samples studied are at the nanoscale, where the kinematical approach remains applicable. However, for thick crystalline materials, multiple scattering events become significant, and the kinematical approximation breaks down. In such cases, a more rigorous treatment using dynamical diffraction theory is required. Although this thesis does not cover dynamical diffraction theory, readers interested in a deeper understanding are referred to standard textbooks[2,15].

3 Bragg Diffraction Imaging Methods

The use of X-ray diffraction to investigate the internal structure materials dates back to the early 20th century, when scientist first recognized the crystalline materials diffract X-rays in predictable way[9,10]. The earliest studies was conducted using laboratory-based X-ray sources, such as *X-ray tubes* firstly invented by W. Crookes[16] in the 1870s-1880s. In this design, electrons emitted from a cathode are accelerated by an electric field and then collide with a fixed anode to produce X-ray waves. These devices were limited by low intensity, poor flux and insufficient coherence. As a result, the resulting diffraction patterns were often weak and blurred, restricting both spatial resolution and sensitivity to subtle structure features.

With the evolution of synchrotron light sources, these limitations have been largely overcome. Modern synchrotron light sources provide X-ray beams with exceptionally high quality, enabling detailed studies of materials with nanometer resolution.

This chapter begins with an introduction to synchrotron light sources, as all the experiments discussed in this thesis were conducted using synchrotron-based X-rays. The experimental configuration is then presented, followed by a discussion of the associated coordinate transformation. Two diffraction imaging techniques, *scanning X-ray diffraction imaging* (nano-XRD) and *Bragg coherent diffraction imaging* (BCDI), which share a similar experimental setup, are introduced in separate sections, with details on their underlying principles and applications.

3.1 Synchrotron Light Sources

Synchrotron radiation refers to the electromagnetic radiation emitted when relativistic electrons are accelerated along a curved trajectory by magnetic fields. It was first observed in 1947 as a secondary effect in a particle accelerator at General Electric Research Laboratory in New York. Since then, synchrotron technology has advanced significantly, progressing through several generations. Today, fourth-generation synchrotron light sources provide highly coherent, ultra-bright X-ray beams that have become indispensable tools in a wide range of scientific disciplines.

3.1.1 Production of X-ray Radiation

Figure 3.1 illustrates the MAX IV Laboratory[17–19], the world's first 4th generation synchrotron light source. It consists of two *storage rings*[20] and one *linear accelerator* (LINAC) for electron acceleration. Electrons are initially produced by the electron gun and then accelerated to the designated energy in LINAC before being injected into the target storage ring.

Inside the storage ring, electrons circulate along closed orbit, maintained by a magnetic lattice composed of *achromats*. Each achromat includes a specific arrangement of magnets serving different functions. For instance, *bending magnets*[21] are used to keep the electrons in a curved trajectory. The circulating electrons then emit synchrotron radiation in the shape of a cone in the direction of velocity, which is subsequently delivered to individual *beamlines* for specific scientific experiment. The energy lost by the electrons due to radiation emission is compensated by *radiofrequency* (RF) cavities placed around the storage ring, which re-accelerate the electrons to maintain their nominal energy. To sustain a constant electron current stable over time, fresh electrons are periodically injected from the LINAC in a process known as *top-up* injection, ensuring a continuous and consistent electron beam.

Compared to the traditional lab-based X-ray sources produced by X-ray tube, synchrotron light source can produce X-ray with much higher quality in terms of *brilliance*[2], intensity and energy range. Brilliance $B(\lambda)$ is a key parameter for evaluating an X-ray source, as it describes how the spectral X-ray *photon flux* $\Phi(\lambda)$ is distributed spatially and angularly. It is defined as:

$$B(\lambda) = \frac{\Phi(\lambda)}{(2\pi)^2 \varepsilon_h \varepsilon_v} = \left[\frac{\text{number of photon/s}}{\text{mrad}^2 \cdot \text{mm}^2 \cdot 0.1\% \text{ bandwidth}}\right]. \tag{3.1}$$

Here, ε_h and ε_v represents the emittance in horizontal and vertical directions, respectively. Emittance is determined by both the *beam size* σ and its *divergence* σ', such that $\varepsilon = \sigma\sigma'$.

To achieve higher brilliance, modern storage rings rely on *insertion devices* installed in the *straight sections* of the ring. These devices are classified into two types: wigglers and undulators[2]. Both share a similar structure, consisting of a series of alternating dipole magnets that force electrons to follow a sinusoidal trajectory. In undulators, the magnetic field strength and period are relatively small, allowing the radiation emitted from successive oscillations to interfere constructively. This produces a highly collimated, quasi-monochromatic X-ray beam with significantly enhanced brilliance.

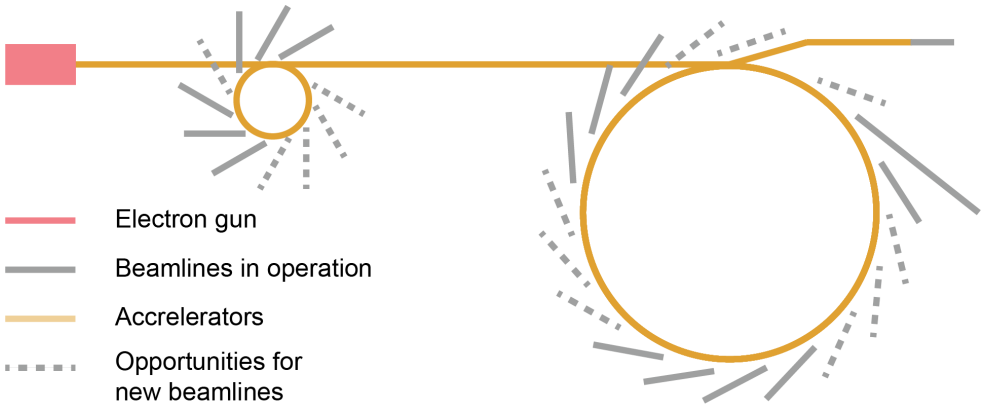

Figure 3.1 Illustration of the MAX IV synchrotron facility. The MAX IV synchrotron source features two rings: a smaller ring operating at 1.5 GeV for soft X-rays and a larger ring operating at 3GeV for hard X-rays. NanoMAX is the longest beamline at MAX IV.

One key advancement at the MAX IV Laboratory, compared to other third-generation synchrotron facilities, is the implementation of a diffraction-limited storage ring[22] (DLSR) in the hard X-ray ring. It employs a multi-bend achromat (MBA) lattice with denser magnetic arrangement to better control the size and divergence of the electron beam. This directly enhances the brilliance of emitted X-ray radiation.

The brilliance is tightly tied to another important property of the X-ray source, coherence, which is also essential for X-ray diffraction imaging techniques. The *coherent flux*[23] of an X-ray source is related to its brilliance $B(\lambda)$ by:

$$\Phi_c(\lambda) = B(\lambda)\left(\frac{\lambda}{2}\right)^2. \tag{3.2}$$

This equation shows that the coherent flux is directly proportional to the brilliance of the X-ray source. Therefore, high-brilliance sources, such as synchrotrons, can also produce high coherent flux, which is essential for advanced X-ray imaging techniques such as coherent diffraction imaging (CDI).

3.1.2 Beamline Configuration

Figure 3.2 illustrates the configuration of the NanoMAX beamline at MAX IV Laboratory, at which most work in this thesis was conducted. In this section, NanoMAX is used as a representative example to demonstrate how the emitted X-rays are tailored to meet specific experimental requirements.

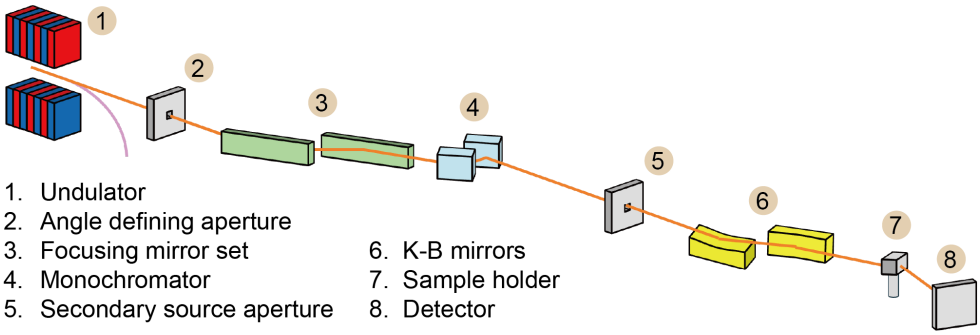

Figure 3.2 Sketch of the NanoMAX beamline. The beam from the storage ring is tailored to the experiment using a set of optical components.

The NanoMAX beamline is capable of providing a nano-sized focused beam with high coherence[24–26]. To satisfy these requirements, the radiation from the undulators is firstly collimated using a set of slits, followed by focusing to a smaller beam using focusing mirrors. A *monochromator* consisting of two Si <111> crystals is then used to select the desired wavelength of the X-ray by rotating the crystals to a specific angle that satisfies Bragg's law, thereby enhancing the temporal coherence of the beam. The beam is further spatially refined by a *secondary source aperture* (SSA), which improves its spatial coherence in an adjustable way. To achieve nanoscale focusing, a pair of *Kirkpatrick-Baez* (KB)[27] mirrors is used, with one focusing the beam vertically and another horizontally. For effective focusing, the incident angle of the beam on the KB mirror must be grazing to ensure the total external reflection.

In a beamtime experiment at NanoMAX, the sample is secured by a sample holder mounted on a scanning stage. The scanning stage has a three-layered structure. The bottom layer, a goniometer stage, allows the sample to be rotated in three directions to achieve the required Bragg geometry. Above it is a scanning stage, which provides coarse positioning. The piezoelectric scanning stage, mounted on the coarse scanning stage, moves the sample with high precision along three axes. Additionally, a Eiger 500K detector is mounted on the robot arm, providing the necessary degrees of freedom to collect diffraction patterns during a beamtime experiment.

3.2 Experimental Configuration

To collect the diffraction pattern indicated by Eq. (2.34) under beamline conditions, a special experimental configuration must be employed to satisfy the Bragg condition for the selected Bragg peak.

3.2.1 Configuration in Bragg Geometry

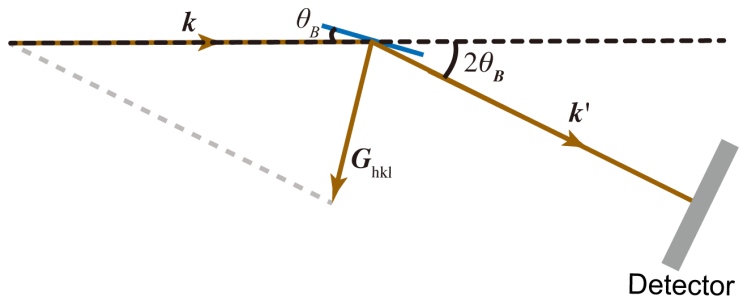

Figure 3.3. Illustration of CDI in Bragg geometry. The configuration is designed to capture the specific Bragg diffraction from crystal planes [hkl]. Blue line represents the targeted crystal planes.

Figure 3.3 illustrates a general configuration for the Bragg diffraction[28]. Since the incident beam $\boldsymbol{k}$ is fixed at the beamline, the detector is positioned at $2\theta_B$ with a detector-to-sample distance r to collect a sufficiently large diffraction pattern. To meet the Bragg condition, the sample is rotated using the stage so that the targeted reflected plane forms an angle θ_B with the incident beam $\boldsymbol{k}$. This configuration can be implemented in either transmission (Laue) or reflection (Bragg) geometry, depending on whether the X-rays pass through or are reflected by the sample. Both geometries are compatible with nano-XRD and BCDI, and the choice primarily depends on the sample. For simplicity, this setup will be referred to as the Bragg geometry throughout the remainder of this thesis.

In the context of the Ewald's sphere, as illustrated in Figure 2.7, the detector can be considered as a flat plane fixed at the angular position, where the Ewald's sphere intersects with the selected Bragg peak. To record the full 3D diffraction volume around this peak, the sample is rotated over a small angular range, known as the *rocking range*, along the rocking direction θ. As the sample is rocked, the detector on the Ewald's sphere moves correspondingly in and out of the Bragg peak, slicing the entire 3D diffraction pattern. Due to the long detector-to-sample distance r, these slices are effectively parallel with a step size defined by the nominated *rocking increment* $\Delta\theta$. The *rocking angles* refer to angles within the rocking range.

3.2.2 Coordinate Transformation

The coordinate system in an experimental setup plays a crucial role, not only in controlling motors and positioning the sample but also in ensuring consistency and accuracy in data analysis. In a configuration introduced by Figure 3.3, the sample is typically represented and controlled within an orthogonal coordinate system (x, y, z), referred to as the *lab coordinate* system. However, the recorded diffraction data follows a different coordinate convention, known as the *natural coordinate*[29] system

(r_1, r_2, r_3). This distinction arises due to the detector being tilted at an angular position of $2\theta_B$ to satisfy Bragg's law. The transformation between these two coordinate systems is essential for the data analysis.

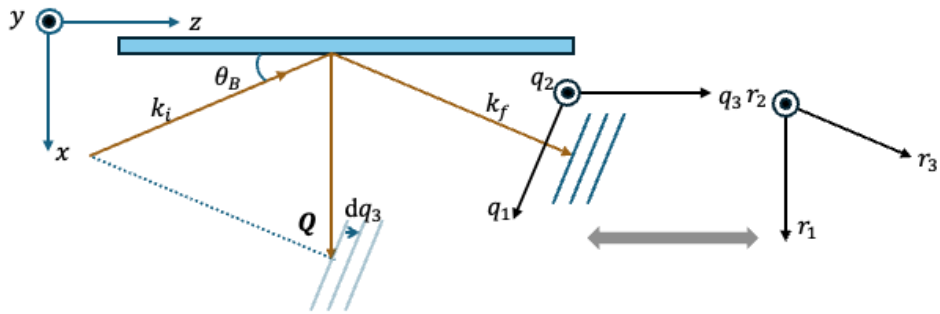

Figure 3.4 Illustration of lab and natural coordinate systems. Geometry relative to the selected reflecting crystal planes.

For convenience, a configuration relative to the selected reflecting crystal planes as shown in Figure 3.4 is employed to illustrate the coordinate transformation.

In this configuration, $q_1 \times q_2$ defines the detector plane, while q_3 corresponds to the rocking direction. Here, q_1 and q_2 represent the horizontal axis and vertical axes of the detector plane, respectively. The detector is pixelated with pixel size of (Δ_h, Δ_v) in the horizontal and vertical directions.

As shown in Figure 3.6 q_1 and q_3 are dependent, while both are independent of q_2. The reciprocal space resolution $(\mathrm{d}q_1, \mathrm{d}q_2, \mathrm{d}q_3)$ can be calculated based on the detector pixel size and the rocking angle increment $\Delta\theta$, as given by[30]:

$$\mathrm{d}q_{1,2} = k\frac{\Delta_{h,v}}{D}, \qquad \mathrm{d}q_3 = |\boldsymbol{Q}|\Delta\theta = 2k\sin\theta_B\,\Delta\theta. \tag{3.3}$$

Here, the scattering vector satisfies Laue condition, $\boldsymbol{Q} = \boldsymbol{H}_{hkl}$. D is the distance between sample and the detector, k is the wavenumber. The unit of $\Delta\theta$ is in radians.

Based on the geometric relationships between lab and natural coordinate systems, the coordinate transformation[29] from the natural coordinate system to the lab coordinate system is:

$$\begin{aligned} q_x &= q_1\cos\theta_B \\ q_y &= q_2 \\ q_z &= q_3 - q_1\sin\theta_B \end{aligned} \tag{3.4}$$

Similarly, the transformation of coordinates in real space from (r_1, r_2, r_3) to (r_x, r_y, r_z) can be written as:

$$\begin{aligned} r_x &= r_1 - r_3 \sin\theta_B \\ r_y &= r_2 \\ r_z &= r_3 \cos\theta_B \end{aligned} \tag{3.5}$$

Note that the coordinate transformations shown in Eq. (3.4) and (3.5) are approximations based purely on the geometric relationships, considering only rotation around the rocking axis. It is valid for the experiments presented in this thesis. For more complex experiments involving multiple rotational degree of freedom, a more accurate transformation method is to use a full rotation matrix formalism[31], though this is not detailed here.

3.3 Scanning X-ray Diffraction Imaging

As illustrated in Figure 2.8, the phase shift induced by lattice displacement directly results in variations in the diffraction patterns around a selected Bragg peak. Scanning X-ray diffraction imaging, also referred as to nano-XRD, is one of the X-ray diffraction imaging techniques that exploits this sensitivity to probe internal structural of crystalline materials. It integrates X-ray diffraction with precise scanning control using motorized stages, which makes it particularly well-suited for extended samples.

The real-space resolution of scanning XRD is limited by the focus size. Thanks to advancements in X-ray focusing optics and the high flux provided by state-of-the-art synchrotron light sources, the beam can now be focused down to the nanoscale[24,32]. Therefore, nano-XRD is capable of measuring fine structural inhomogeneities of nanoscale material with high resolution[32–42].

Paper I and Paper II employed nano-XRD on different material systems, which will be introduced in Chapter 4.

3.3.1 Process of Data Analysis

The idea of nano-XRD is to capture subtle shifts in the detected Bragg peak caused by lattice displacements, as discussed in Chapter 2. The lattice displacement can modify the lattice spacing d and the orientation of lattice planes (tilt), thereby changing the magnitude or the direction of the scattering vector $\boldsymbol{Q}$. Nano-XRD links these Bragg peak shifts to changes in $\boldsymbol{Q}$, enabling the mapping of lattice displacement distribution within the sample.

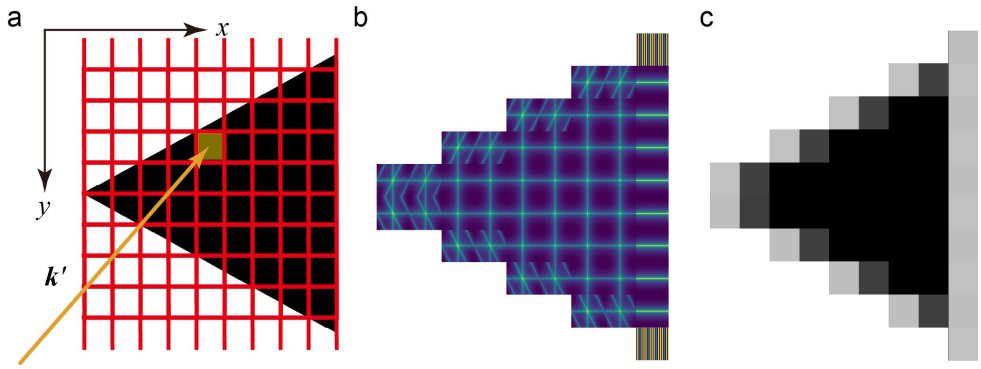

Figure 3.5 illustration of scanning X-ray diffraction. a) A simulated sample with a triangular shape. The red grid represents the scanning trajectory. The yellow shaded rectangle indicates the focus X-ray beam on the sample. b) Diffraction patterns at each scanning point. c) Map of diffraction intensity

As illustrated in Figure 3.5, the sample is moved along the horizontal (x) and vertical (y) axes using piezo motors. The scanning ensures that each grid point within the sample is systematically illuminated by the focused X-ray beam, producing diffraction patterns. By summing the intensity of each diffraction pattern and mapping it to its corresponding grip point, a diffraction intensity map is obtained that reveals the overall morphology of the sample. Nano-XRD normally includes rocking scans to collect 3D diffraction data, capturing Bragg peak shifts along the rocking direction. Note that while the method measures Bragg peak shifts in 3D reciprocal space, the real space imaging is 2D.

The diffraction data are recorded in the natural coordinate system. Prior to further analysis, they need to be mapped to the orthogonal reciprocal space using the coordinate transformation shown in Eq. (3.4).

The Bragg peak shifts in each diffraction can be determined using the *center-of-mass* (COM) method, which is defined as:

$$Q_j^{\mathrm{COM}} = \frac{\sum I_i q_{i,j}}{\sum I_i}. \tag{3.6}$$

Here, $j = (x, y, z)$ denotes the three orthogonal components of reciprocal space. I_i represents the photon counts at pixel i, and $q_{i,j}$ is the coordinate of pixel i along the j-th reciprocal space direction.

Since the diffraction data is already mapped in reciprocal space, the scattering vector $\boldsymbol{Q}$ can be represented by its COM components. Therefore, the magnitude of the scattering vector $\boldsymbol{Q}$ for each individual diffraction pattern is calculated as:

$$Q = |\boldsymbol{Q}| = \sqrt{Q_x^2 + Q_y^2 + Q_z^2}. \tag{3.7}$$

With the calculated Q at each scanning point, obtaining the d- spacing map becomes straightforward using Eq. (2.16). This map provides spatially resolved information about lattice spacing variations across the sample. To further convert the d-spacing map to a strain map, a reference lattice spacing d_0 is required, as described in Eq. (2.28). Typically, the bulk or theoretical lattice spacing for a given $[hkl]$ crystal direction is chosen as d_0. If an absolute reference is not available, an alternative approach is to take the average d- spacing from the measured map and use it as the reference.

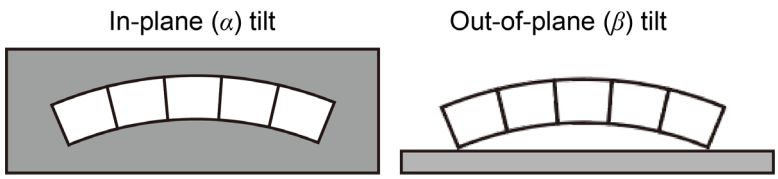

Figure 3.6 Illustration of lattice tilts. The gray rectangules indicate the substrates. Note that the experimental configuration is assumed to follow the transmission geometry. In this setup, an α tilt of the object causes a shift of diffraction in the detector plane, corresponding to an in-plane tilt with respect to the substrate plane. A β title results in a shift of diffraction along θ- axis, corresponding to an out-of-plane tilt relative to the substrate plane.

Shifts in the diffraction pattern can arise not only from changes in lattice spacing but also from lattice tilts within the sample. When the dataset includes rocking scans, the shifts along the rocking direction can also be captured, allowing for a more comprehensive analysis of lattice tilts. These tilts can be categorized into in-plane (IP, α) and out-of-plane (OOP, β) components relative to the detector plane, as illustrated in Figure 3.6. To quantify these tilts, one can evaluate the angular differences between the components of the scattering vector. Following the established notation, Q_x and Q_y represent the in-plane components, while Q_z corresponds to the out-of-plane component.

Based on these components, the definitions for the α and β tilts are defined as

$$\alpha = \sin^{-1}\frac{Q_y}{|\boldsymbol{Q}|}, \qquad \beta = \tan^{-1}\frac{Q_x}{Q_z}. \tag{3.8}$$

Following these definitions, α and β tilts are considered as rotation around Q_z and Q_y, respectively.

Summary of data processing steps for nano-XRD experiment:

1. Perform necessary coordinate transformation on the diffraction data to align it consistently with the sample's coordinate system.
2. Pre-process the diffraction data
3. (Optional) Generate the diffraction intensity map to show the overall morphology of sample.
4. Calculated COM and scattering vector $\boldsymbol{Q}$ for diffraction at each grip point
5. Generate the d-spacing map.
6. Compute the strain map.
7. Calculate the tilt maps.

The procedures outlined above also applied to the work presented in Chapter 4, as well as in Paper I & II.

3.3.2 Limitations

While nano-XRD reveals the internal strain distribution within the extended sample by analyzing the shifts of diffraction peaks, several limitations must be considered when interpreting the results. Chief among these are spatial resolution and the averaging effects inherent in the technique.

The real-space resolution of the reconstructed maps described above is fundamentally limited by the focused beam size. In practice, the resolution can also be constrained by the precision of the motorized stages used for scanning and the optics the beamline, including the stability and focusing performance of the X-ray beam.

At each grid point, the magnitude of the scattering vector $|\boldsymbol{Q}|$, derived from the corresponding diffraction data, reflects an average over a finite probe volume. This volume is determined by the beam footprint and the angular step size of the rocking scan. As a result, fine-scale strain variations within this region may be averaged out, potentially blurring local structural features. Moreover, nano-XRD is a 2D measurement technique, limiting its ability to fully resolve the three-dimensional internal structure of materials.

3.4 Bragg Coherent Diffraction Imaging

Bragg coherent diffraction imaging (BCDI) is an advanced coherent diffraction imaging (CDI) technique that fully leverages the high coherence of fourth-generation synchrotron light sources. Unlike nano-XRD, BCDI offers a 3D structural information by reconstructing the complex electron density of the object from its diffraction pattern. This approach enables higher spatial resolution and allows for detailed, 3D mapping of internal strain.

The foundation of CDI was established by Fienup[43] in 1978, who proposed iterative phase retrieval algorithms to address the 'lost phase' problem, which will be discussed later in this section. Building on this progress, Miao et al. demonstrated the first diffraction imaging (CDI) experiment in transmission geometry[44] with X-rays in 1999. Shortly after, Robinson and his collaborators demonstrated a 2D CDI experiment on a gold nanocrystal in Bragg geometry[45], leveraging the high penetration power of X-rays. They also highlighted the potential to extend this method to 3D to access full strain information in single crystalline grains.

Since then, advancements in brilliant synchrotron sources and detector technology have made BCDI a practical and powerful technique to study internal strain distributions of crystalline materials in a non-destructive manner[46–52].

Paper III, Paper IV and Paper V are related to BCDI, which will be discussed in detail in in Chapter 5 and Chapter 6.

3.4.1 Coherent Diffraction Imaging

In an traditional optical imaging system, the resolution d is fundamentally constrained by the Abbe diffraction limit[3],

$$d = \frac{\lambda}{2NA}. \tag{3.9}$$

Here, NA refers to the numerical aperture of the optical system. For visible light, the NA can easily exceed 1, meaning the resolution is primarily limited by the wavelength. In contrast, although X-rays have much shorter wavelengths, achieving a high NA with X-ray optics is extremely challenging due to the refractive index being very close to unity.

On the other hand, CDI, including BCDI, avoids the Abbe limit by extracting the structural information of illuminated crystal from the diffraction patterns using a phase retrieval process, which will be discussed in detail later. This method enables resolution far better than the optics can provide. Note that in practice, although CDI is a called a lensless technique, it normally uses lenses for collimation of the primary beam. However, the role of the optics in CDI is to increase the flux density on the sample, not to give spatial resolution.

The resolution of CDI is determined by the finest diffraction features, commonly referred to as fringes, that are recorded by the detector. As shown in Figure 2.8, the fringe intensity at higher Q-values (peripheral regions of the diffraction pattern) decays fast compared to that at the low Q-values (central region). In fact, the intensity of coherent diffraction, $I(\boldsymbol{Q})$, typically falls off[2] as $I(\boldsymbol{Q}) \propto 1/|\boldsymbol{Q}|^4$. This means that achieving high resolution in CDI requires an intense and brilliant X-ray source capable of capturing high-Q diffraction fringes. For this reason, synchrotrons

are considered as the ideal X-ray source for CDI due to their high flux and exceptional brilliance.

3.4.2 Phase Problem and Iterative Phase Retrieval

The *phase problem*[53,54] refers to the loss of phase information in diffraction experiments, as detectors can only record intensity. However, the high coherence of the X-ray beam used in BCDI enables the phase to be computationally retrieved.

Phase retrieval is the iterative computational algorithm used to reconstruct the phase from a coherent diffraction intensity pattern. The foundation of this approach was first proposed by Sayre[55], who demonstrated the possibility of reconstructing object from its well-sampled diffraction magnitude. Later, Fienup[56] and many others contributed to the development of phase retrieval algorithms.

Process of a Typical Phase Retrieval Algorithm

Here, the *Error-reduction* (ER) algorithm[43] is used as an example to illustrate the workflow of the iterative phase retrieval algorithm reconstruction, as shown in Figure 3.7. In this framework, $\rho(\boldsymbol{r})$ represents the reconstructed complex object in real space, while $A(\boldsymbol{Q})$ denotes the complex amplitude in reciprocal space.

The first step in ER is to initialize the phase estimate. A random initial phase is assigned to an initial guess of binary shape function representing the object ρ. This estimated object is then transformed into reciprocal space via a Fourier transform ($\mathcal{F}$), producing the estimated diffraction A. Next, the real part of A is replaced by the measured modulus of the diffraction intensity ($\sqrt{I}$), while the phase is left unchanged, generating an updated estimate A'. The inverse Fourier transform ($\mathcal{F}^{-1}$) is then applied to A', yielding a new complex object ρ' in real space. To refine the solution, a real-space *support constraint* is applied on ρ'. This updated ρ'' is used as the input for the next iteration. The algorithm iteratives this process until convergence, which is achieved when the reconstructed diffraction satisfies $|A| = \sqrt{I}$.

The support constraint in this process enforces the prior knowledge of the object, such as a finite size. This constraint is represented as a binary shape function, where values inside the support are set to one and those outside are set to zero. If no prior knowledge about the object's shape is available, the initial support is generally estimated as the autocorrelation function calculated from the measured diffraction intensity I. Since the autocorrelation is twice larger than the object and the exact object boundary is always unknown, an *adaptive support updating* strategy is necessary for refinement. One commonly used method is the *Shrink-wrap*[57] algorithm, where the support is updated by applying a Gaussian blur to the real-space estimate, followed by thresholding to refine the boundary.

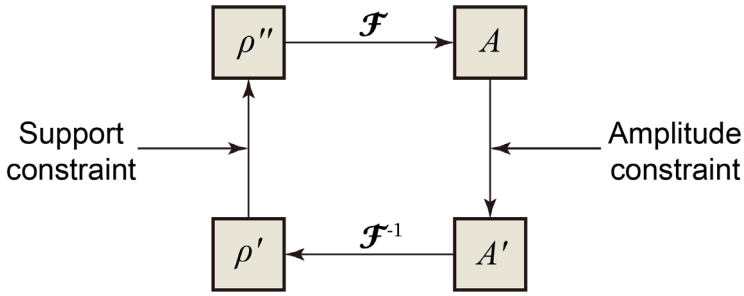

Figure 3.7 Basic steps in the Error-reduction phase retrieval algorithm. The illustration depicts a single iteration of the iterative reconstruction process.

Most other phase retrieval algorithms are developed based on the ER method, with necessary modifications in how real-space support constraints are applied. For example, the *hybrid input output* (HIO)[43] method introduces a feedback mechanism of the support constraint from the previous iterations. The *relaxed averaged alternating reflection* (RAAR)[58] algorithm introduces a weighting parameter to balance the behaviors of ER and HIO.

Phase retrieval is a powerful tool for reconstructing the missing phase information from coherent diffraction patterns. However, it is not the primary focus of this thesis. Instead, it is treated as a standard computational method for data analysis. To maintain consistency and minimize variability in the analysis, the involved phasing process is performed using the software *PyNx*[59] developed by Favre-Nicolin et al., applying default phase retrieval algorithms with the same preset parameters in most analysis discussed in this thesis.

Phase Wrap and Phase Ramp

Once the phase is reconstructed by the phase retrieval algorithm, certain considerations needed to be addressed before proceeding with analysis.

One such issue is the *phase wrap.* The reconstructed phase is inherently limited to the range of $(-\pi, \pi)$ due to the nature of the Fourier transform operation. However, the actual phase $\phi(\boldsymbol{r})$ may exceed this range, causing discontinuities known as phase wrap in the reconstruction. Since phase values are cyclic during phase retrieval process, exceeding the range results in abrupt jump between $-\pi$ and π. This issue can be corrected by phase unwrapping, where the phase range is extended by adding integer multiples of 2π to the region where abrupt phase jump occurs.

Another issue is the phase ramp. If the original diffraction is not centered correctly in reciprocal space, the corresponding reconstructed phase in real space will exhibit a phase ramp instead of a uniform phase distribution. This can be corrected by identifying the phase ramp over the reconstruct object and multiplying the object with a complex conjugate phase term.

Resolution of Reconstruction

Since BCDI relies on both diffraction data and phase retrieval, evaluating the resolution of the reconstruction is not straightforward[60]. Unlike nano-XRD, where the resolution is defined by the focused beam size, in BCDI the resolution depends on the quality of diffraction data and the accuracy of the phase retrieval process. Here, two methods are introduced to evaluate the resolution of BCDI reconstructions: the *phase retrieval transfer function* (PRTF)[61] and the *Gaussian fitting criteria*[62].

PRTF quantifies the reliability of the reconstructed phase at different spatial frequency Q. By radially integrating the diffraction volume over Q, the PRTF is defined as the ratio of the diffraction amplitude obtained from the reconstructed complex electron density to the measured amplitude over shells of constant spatial frequency Q:

$$PRTF(Q) = \frac{|\mathcal{F}\{\rho\}|(Q)}{\sqrt{I(Q)}}. \tag{3.10}$$

For a typical BCDI reconstruction, PRTF values are close to 1 at low Q, indicating that the phases at these spatial frequencies are consistently recovered. As Q increases, the PRTF drops, suggesting increasing uncertainty in the retrieved phase. The resolution is commonly defined as the point Q_e at which PRTF $< 1/e$, where e is Euler's number. The real-space resolution can be calculated as $\Delta r = 2\pi/Q_e$. This method was used in Paper III to evaluate the reconstruction resolution.

The Gaussian fitting criteria evaluates the resolution of phase retrieval reconstruction by analyzing the sharpness of reconstructed sample edges at different directions. This method involves a line read-out of intensity across edges in the reconstructed image. Edge locations are first determined by fitting the intensity profiles with error functions (erf functions). Gaussian fitting is then applied to the derivatives of the fitted edges, and the full widths at half maximum (FWHMs) of the fitted Gaussian functions provide a quantitative measure of the spatial resolution at different directions. This method was employed in Paper IV to assess the resolution of the reconstruction.

3.4.3 Data Acquisition and Data Analysis

Data Acquisition and Data Analysis

As described earlier, rotating the sample along the rocking direction allows the detector to slice and record the complete 3D diffraction pattern. In practice, BCDI involves rotating the sample over a small angular range (typically ~1°) in hundreds of steps. To accurately capture fine features of the diffraction pattern, the

measurement must satisfy the *Nyquist-Shannon* theorem. This ensures that the diffraction data are sufficiently sampled to retain all spatial frequency information necessary for phase-retrieval reconstruction. Additionally, the sample must be precisely positioned at the center of rotation to avoid real space shift of the sample during the measurement.

A simple way to illustrate the 3D diffraction volume is by using a *rocking curve*. To obtain a rocking curve, the intensities of each slice of the diffraction volume are summed up and plotted against the angular position along the rocking axis. Since the rocking curve is directly related to the intensity distribution of diffraction along rocking direction, it also reflects the strain situation to some extent.

The complex electron density of the sample is obtained after applying the phase retrieval algorithms. Before further analysis, the coordinate transformation (Eq. 3.5), also referred as to rectification, should be performed to the reconstruction. The phase term φ represents the projection of lattice displacement on the selected direction, as stated in Eq. (2.34). The strain can be obtained using Eq. (2.27)

In conclusion, the data analysis process for BCDI measurements can be summarized as follows:

1. Pre-process the diffraction data.
2. Perform phase retrieval on the data and rectify the reconstruction.
3. Visualize the reconstruction and unwrap the reconstructed phase if necessary.
4. Calculate the strain distribution.

The procedure outlined above applied to the work presented in Chapter 5 and Chapter 6, as well as in Paper III, Paper IV & V.

3.4.4 Limitations

BCDI typically requires that the probed sample be relatively small and fully illuminated by the coherent X-ray beam, and well-isolated from surrounding structures to avoid interference effects in the diffraction pattern. However, recent studies have demonstrated the feasibility of applying BCDI to extended samples[63,64], where only a portion of the sample is illuminated. In such cases, phase retrieval can still be successfully performed, as the targeted Bragg peaks remain well-isolated in the reciprocal space, even though the material is continuous in real space. In Paper IV, such a strategy was employed to measure the strain in a heterostructured nanowire.

Additionally, the accuracy of the BCDI results relies heavily on the recorded diffraction data. As mentioned earlier, satisfying the sampling condition[55] is crucial to ensure the correct reconstruction of fine details within the sample. Other than this, the quality of diffraction data also plays a significant role.

Any unpredicted angular distortions caused by unstable experimental conditions external factors, such as beam radiation pressure, heating or applied electromagnetic field[65–67] during data acquisition, can affect the measurements. These angular uncertainties may lead to unexpected artifacts[68] in the reconstructions. This issue is particularly common in complex setups, such as *in situ* experiments. Such limitations undoubtedly constrain the broader applicability of BCDI.

Methods to mitigate the effects of angular uncertainty have been studied recently[68,69]. In Paper III, we proposed a state-of-the-art algorithm capable of handling large angular distortions in diffraction datasets. This algorithm was subsequently applied in Paper IV to improve data quality. In Paper V, we introduced a novel strategy to reconstruct the diffraction volume from datasets with completely unknown angles.

4 Strain and Lattice Tilt Analysis via Scanning X-ray Diffraction

In this chapter, two studies are presented to demonstrate the application of nano-XRD in resolving different aspects of crystalline structure. The first focuses on a heterostructured metal halide perovskite nanowire, where nano-XRD is used to probe the lattice spacing across the entire nanowire (Paper I). The second investigates a bismuth ferrite ($BiFeO_3$, BFO) thin film, where nano-XRD enables imaging of ferroelectric domains by detecting variations in lattice orientation (Paper II). Notably, this work also highlights the capability of nano-XRD to resolve ferroelectric domains beneath metallic electrodes, an area inaccessible to conventional methods such as piezoresponse force microscopy (PFM), underscoring the unique advantages of X-rays.

Together, these studies illustrate how nano-XRD can be adapted to reveal both lattice spacing and orientation in complex nanostructured materials.

4.1 Heterostructures and Ferroic Domains

To aid the interpretation of the results discussed in the following sections, a brief overview of *heterostructures* and *ferroic domains* is presented below.

4.1.1 Heterostructures

Heterostructures are formed when two or more crystalline materials are joined together, generally with different lattice parameters. The lattice mismatch at the interface introduces strain, which can significantly alter the electronic band structure and carrier mobility of the system. This band structure engineering enables tunable optoelectronic properties, making heterostructures valuable in a wide range of applications such as photovoltaics[70,71], light-emitting diodes[72–74], and quantum devices[75–78].

However, if the lattice mismatch exceeds the elastic strain accommodation limit of the materials, i.e. the *coherency limit*[79], the system may form dislocations or other defects, which can degrade device performance or cause failure.

At the nanoscale, the devices often exhibit higher strain tolerance than in bulk[80,81], because their high surface-to-volume ratio allows more effective stain relaxation. This makes it possible to interface a broader range of materials, opening new opportunities for designing heterostructures with tailored functionalities.

4.1.2 Ferroic Domains

The ferroic family[82] of materials includes *ferromagnetic*, *ferroelastic* and *ferroelectric* materials.

In ferroelastic materials, a structural phase transition, for example, from cubic to tetragonal lattice, changes the shape of unit cell. This transformation creates domains with different lattice orientations coexisting within the same crystal. Each domain exhibits distinct spontaneous strain state, which can be modified by external mechanical stimuli, such as stress or temperature.

Analogous to the spontaneous strain state in ferroelastic materials, ferroelectric materials are characterized by spontaneous electric polarization, which arises from a relative displacement between positive and negative ions within the unit cell. When many unit cells align with the same polarization direction, ferroelectric domains form. These domains can be switched by the external electric field, and importantly, maintain their polarization state upon removal of the external field.

Domain walls are the boundaries that separate regions of different domain states and typically lie along preferred crystallographic directions. From a lattice perspective, these walls introduce local lattice mismatches due to discontinuities in strain or polarization. In ferroelastic system, such lattice mismatches are characterized as *spontaneous strain*. In ferroelectric system, the domains instead correspond to *spontaneous electric dipole moments*.

Ferroelectricity and ferroelasticity are often coupled, meaning for instance that strain can affect the ferroelectric properties. Thus, in some cases, information about the ferroelectric properties can be inferred by analyzing the variation in diffraction pattern induced by the strain or tilt.

4.2 Strain Mapping of Heterostructured Perovskite Nanowires

Semiconductor nanowires have emerged as a versatile platform for nanoscale electronics and optoelectronics[83–85]. While early research focused on silicon-based nanowires, the field quickly expanded to include III–V compound semiconductors such as InP, GaAs, and GaN. Compared to silicon, these materials offer higher electron mobility and direct, tunable bandgaps, making them well-suited for high-speed electronics, light emitting diodes, and laser applications. More recently, halide perovskite nanowires[86–89] have garnered significant interest due to their superior light absorption, low production costs, and scalability. Their defect-tolerant nature also gives them a competitive edge under non-ideal fabrication conditions.

A major advancement in nanowire technology has been the engineering of axial and radial heterostructures within individual nanowires. The strain can significantly affect the band structure, and in many cases, can be tuned to enhance device performance. Therefore, characterizing the internal structural state of heterostructured nanowires is critical for guiding device design.

In this section, nano-XRD has been employed to examinate the internal structure state of $CsPbBr_3$/ $CsPb(Br_{1-x}Cl_x)_3$ perovskite nanowires, as reported in Paper I.

4.2.1 Sample Synthesis

The synthesis of the heterostructured $CsPbBr_3$/ $CsPb(Br_{1-x}Cl_x)_3$ nanowire[90,91] was carried out by our colleague Nils Lamers. The overall process consists of two main steps: the growth of pure $CsPbBr_3$ nanowires and the subsequent anion exchange to create the heterostructure.

In the growth process[92,93], anodized aluminum oxide (AAO) membranes with cylindrical pores of 200 nm diameter are used as templates. Nanowires nucleate from a precursor solution containing CsBr and $PbBr_2$ and grow inside the pores of the AAO structure. After emerging from the template as free-standing nanowires, they are collected by gently scraping the AAO surface with a tissue. These nanowires are then transferred to a Si_3N_4 membrane substrate for further processing.

To form the heterostructure, a part of each nanowire is selectively masked with a polymer, while the exposed section is subjected to chlorine gas. During this anion exchange process, some bromide (Br) ions in the exposed regions are replaced by chloride (Cl) ions, resulting in the formation of a $CsPb(Br_{1-x}Cl_x)_3$ segment.

4.2.2 Results and Discussion

The research was conducted on both pure $CsPbBr_3$ and heterostructured $CsPb(Br_{1-x}Cl_x)_3$ nanowires. A 60 nm² focused X-ray beam with an energy of 15 keV was used for the measurements. The setup was configured to probe the (004) Bragg peak of the nanowires, which aligns with their growth axis. Additionally, X-ray fluorescence (XRF) was employed to assist in sample localization and to support elemental analysis. The 15 keV incident energy was sufficiently high to excite the K_α emission line of Br, enabling direct detection of its distribution.

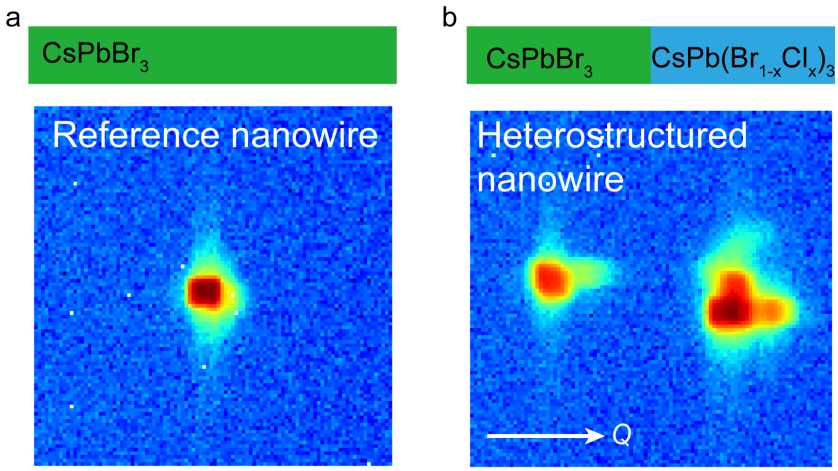

Figure 4.1 Illustration of nanowires and their corresponding diffraction patterns. a) Pure $CsPbBr_3$ nanowire and its corresponding (004) Bragg diffraction. b) Schematic of a heterostructured nanowire, showing two separated (004) diffraction peaks. The left diffraction peak corresponds to $CsPbBr_3$, and the right peak corresponds to $CsPb(Br_{1-x}Cl_x)_3$.

Figure 4.1 displays the diffraction patterns from a reference $CsPbBr_3$ nanowire and from the chlorinated ($CsPb(Br_{1-x}Cl_x)_3$) segment of a heterostructured nanowire. The rectangular shape of the Bragg peaks originates from the slits before KB mirrors. In Figure 4.1(b), two distinct peaks are observed, corresponding to the $CsPbBr_3$ and $CsPb(Br_{1-x}Cl_x)_3$ regions. The slight difference in their lattice spacings, originating from the smaller size of Cl compared to Br, leads to a separation of Bragg peaks in reciprocal space. The Bragg peak appearing at the high Q (right side) corresponds to $CsPb(Br_{1-x}Cl_x)_3$, which has a smaller lattice spacing. By also rotating the nanowires along the rocking direction, nano-XRD can extract the detailed lattice spacing map and tilt maps through COM analysis of the entire 3D reciprocal volume.

The results of the nano-XRD measurements of both the reference and heterostructured nanowires are presented in Figure 4.2. X-ray fluorescence (XRF)

maps for Br and Cl are also included to support the structural analysis. For the reference nanowire, only the central region is shown in Figure 4.2, as both ends are slightly bent and deviate from the Bragg condition.

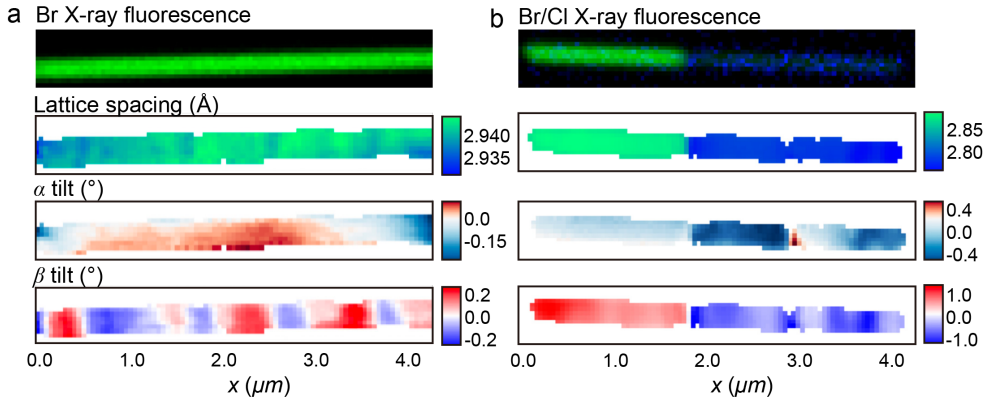

Figure 4.2 Nano-XRD results from perovskite nanowires. a) Pure $CsPbBr_3$ nanowire and b) $CsPbBr_3$/ $CsPb(Br_{1-x}Cl_x)_3$ heterostructured nanowire. The first row in both (a) and (b) shows X-ray fluorescence (XRF) maps. Green indicates the spatial distribution of bromine, while blue corresponds to chlorine.

The reference nanowire shows a highly uniform Br distribution in the XRF map. Consistent with this, its lattice spacing map also exhibits a homogeneous distribution, with an average of $d = 2.941$ Å, which is very close to the expected value d= 2.940 Å. In contrast, the heterostructured nanowire reveals a distinct deviation in lattice spacing between the unchlorinated and chlorinated regions. The transition boundary in lattice spacing map coincides with the compositional interface identified by XRF signal. The average lattice spacing in the unchlorinated region is $d = 2.928$ Å, while it decreases to $d = 2.845$ Å in the chlorinated segment. The slightly reduced lattice spacing in unchlorinated region compared to the pure $CsPbBr_3$ suggests partial diffusion of chlorine from the chlorinated side into the unchlorinated side.

Using the average value $d_{004} = 2.941$ Å as the lattice spacing for pure $CsPbBr_3$, the chlorine concentration x can be estimated by Vegard's law together with tabulated values for orthorhombic $CsPbCl_3$ and the measured lattice spacings. The calculation yields average values of $x = 9\%$ in the unchlorinated segment and $x = 66\%$ in the chlorinated segments. These calculations are in good agreement with the estimation from the XRF signal, which indicates $x = 3\%$ and $x = 70\%$, respectively.

The α tilt map clearly reveals the bending of the reference nanowire. In the case of the heterostructured nanowire, a distinct difference in tilt angle of approximately 0.2° is observed between the different segments. Additionally, a sharp positive peak

in α tilt appears around $x = 3\ \mu$m, which lies between the two plateau regions in the β tilt map where the tilt angle remains close to zero.

Similar periodic tilts with opposite signs, separated by a plateau, are observed in both the reference and the heterostructured nanowire in the β tilt map. When correlated with the lattice spacing map, it becomes evident that the regions exhibiting opposite tilt signs do not correspond to significant variations in lattice spacing. These observations suggest the formation of ferroelastic domains, which are widely reported for $CsPbBr_3$ in literature[39,94]. The regions with opposite tilt angles can be interpreted as domains with different crystal orientations, i.e., twin phases. In our configuration, these domains may be rotated around the *c*-axis of the crystal lattice. The plateau likely corresponds to a domain wall separating adjacent domains. In addition to these ferroelastic domains, a clear angular mismatch at the heterojunction interface is observed in the heterostructured nanowire.

While the structural features observed in the lattice spacing map and tilt maps offer valuable insights, it is important to acknowledge the limitations of the measurement technique. As explained in the previous chapter, the spatial resolution of nano-XRD maps is primarily constrained by the beam size. Even with a focused beam as small as 60 nm², the technique may still struggle to fully capture subtle, localized variations in lattice spacing or tilts. Additionally, the Bragg geometry inherently alters the beam footprint on the sample and skews the illumination geometry, potentially introducing further resolution limitations and spatial distortions. These factors should be considered when interpreting fine structural features.

4.3 Imaging Ferroelectric Domains in Bismuth Ferrite Thin Films

Ferroelectric thin films have been widely investigated for computing and data storage applications due to their switchable polarization[95]. The performance of such devices largely depends on the nano to microscale architectures of ferroelectric domains. These domain structures are typically complex. Given the possibility of domain switching under external stimuli like electric fields, multiple domain variants often coexist within a thin film. Imaging the domain structure is crucial for understanding its structure-property relation and is therefore essential for optimizing device performance.

Conventional optical microscopy struggles to achieve a resolution that is high enough for distinguishing domains. Piezoresponse force microscopy (PFM) is one of the most commonly used techniques for imaging ferroelectric domains. It is a scanning probe technique that image domains by detecting the piezoelectric response of a sample under an applied AC voltage. The voltage is applied through

a conductive cantilever tip, which also served as the detector. The resulting electric field induces mechanical deformation in the sample via the inverse-piezoelectric effect, causing it to expand or contract depending on the polarization direction. Out-of-plane polarization results in vertical surface deformation, while in-plane polarization leads to lateral (sideways) deformation. By measuring the corresponding cantilever deflections, PFM enables high-resolution imaging of ferroelectric domains.

Despite its high spatial resolution and sensitivity, PFM has limitations, particularly when characterizing the electrical properties of ferroelectric devices with top electrodes. In such cases, the presence of a top electrode not only blocks the direct mechanical contact between the cantilever tip and the sample surface but also prevents local electrical coupling, as any applied electric field is distributed across the entire electrode. As a result, PFM is unable to image or measure the domain state beneath the electrode. These limitations make it challenging to investigate domain behavior in fully integrated devices or capacitor structures where electrodes are necessary for electrical testing.

Nano-probe X-ray imaging techniques, such as scanning nano-XRD, shows great potential to fill the gap, as the X-ray source provides excellent penetration to pass through thick electrodes and offers high strain sensitivity. As discussed earlier in this chapter, ferroic domains may induce lattice distortion and orientation, which can be effectively detected by nano-XRD[96–99].

In the rest of this section, I will present the study employing nano-XRD to map ferroelectric domains in a bismuth ferrite ($BiFeO_3$, BFO) thin film[100]. For further details, readers are referred to Paper II.

4.3.1 Sample and Experimental Configurations

The rhombohedral (R3c) structured BFO thin film[101] was grown on a $SrRuO_3$ (SRO)-buffered $DyScO_3$ (DSO) substrate by our collaborators in the group of Morgan Trassin at ETH Zürich. In the BFO system, ferroelectric domains are coupled with ferroelastic domains. As illustrated by Figure 4.3(a), the epitaxial strain results in stripe-like ferroelastic domains orientated about 71° apart along DSO [001] directions, forming the overall ferroelectric domain architecture. The ferroelectric polarizations generally point along four distinct [111] pseudo-cubic (pc) directions, resulting in a total of eight possible polarization orientations in BFO. The small white arrows in Figure 4.3(a) display examples of these polarization directions.

Nano-XRD was conducted on these BFO thin films. The experimental configuration was set to align the BFO $(003)_{pc}$ Bragg peak and led to the beam footprint on the sample becoming elongated to 60 nm × 180 nm. Diffraction datasets for BFO sample were obtained by scanning with a step size of 50 nm in the xy- plane.

Figure 4.3(b–d) illustrates the experimental setups and the definitions of the tilts α and β, which is slightly different here compared with paper I. In the context of the BFO system, α represents tilts between ferroelectric domains (along the $[100]_{pc}$ direction), while β corresponds to tilts along the domains (along $[010]_{pc}$). Depending on how the sample is mounted relative to the incident beam direction $\boldsymbol{k}_i$, the measurement configuration can be classified as either parallel or perpendicular. Due to the differing sample orientations, the α and β tilts in this study are both calculated as rotations around q_z, but in parallel and perpendicular configurations, respectively.

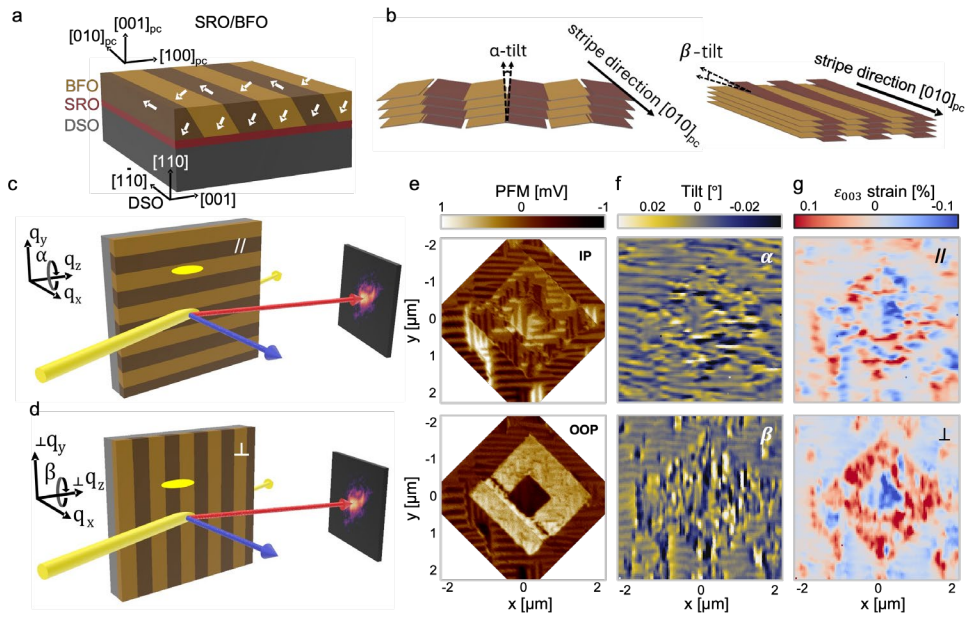

Figure 4.3 Schematic of the BFO sample and experimental configurations. a) Illustration of BFO thin film grown on SRO-buffered DSO substrate. b) Tilts α and β with respect to the stripe-like domain direction. c) Experimental setups of nano-XRD measurements with domains aligned either parallel (c) or perpendicular (d) to the incident beam $\boldsymbol{k}_i$ direction. The yellow ellipses on the sample represent the footprint of the incident beam. e) PFM results on a box-in-box region of BFO thin film and the corresponding f) tilt maps and g) strain maps.

The box-in-box feature observed in the measured BFO was created by PFM, applying opposite voltages to different regions, as clearly illustrated by the OOP PFM map in Figure 4.3(e). The area outside the box corresponds to the as-grown (AG) BFO. In the AG region, ferroelectric domains are clearly resolved in both the α and β tilt maps (see in Figure 4.3(f)). However, within the box areas, the tilt maps struggle to visualize the domain structures clearly. This limitation may be due to interference effects arising from complex domain structure in the poled (box)

regions. Even so, the tilt maps still reveal a strip-like structure that is consistent with the PFM results. Overall, α tends to correlate with the IP PFM, while β shows closer agreement with the OOP PFM, consistent with their respective definitions.

It is important to note that the α and β tilt maps presented in this study and in Paper II are approximations of the true tilt distributions. This is because the full 3D diffraction datasets typically required for accurate tilt calculations (as described in Equations (3.16) and (3.17)) were not measured in this case.

The strain maps displayed in Figure 4.3(g) exhibit high contrast in both the AG region and the box areas. In particular, under the perpendicular configuration, the strain map clearly reveals the edges of the boxes, where polarization switching occurs. As explained in Paper II, the X-ray beam footprint covers multiple domain stripes, and the inherent averaging effect enhances the contrast associated with polarization changes.

This example demonstrates that nano-XRD offers spatial resolution required to resolve comparable features to PFM, while additionally providing structural information such as strain.

4.3.2 Domains Underneath Electrodes

Here, the case of device integration is considered. The BFO thin film was configured in a capacitor structure, with a platinum (Pt) top electrode. During the measurement, the sample was aligned such that the majority of the stripe-like domains were aligned parallel to the incident beam direction.

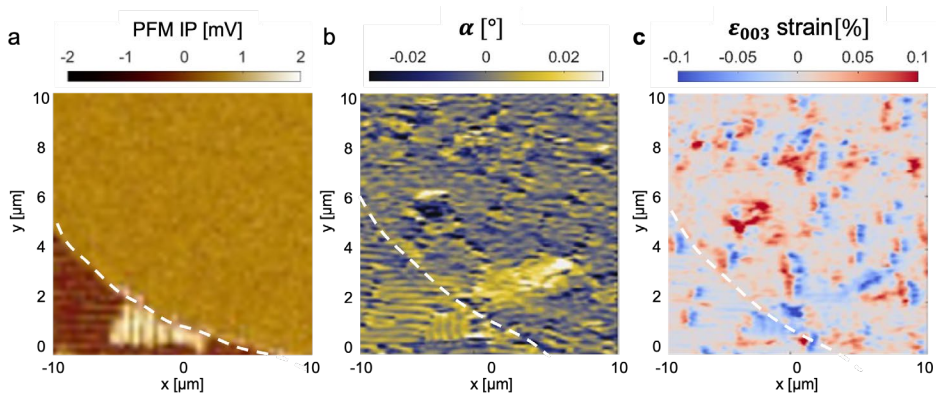

Figure 4.4 Microscopy of domains beneath a metal electrode. a) IP PFM result around the electrode area. b) α tilt map of the same region. c) Corresponding ε_{003} strain map. The white dashed lines indicate the boundary of the electrode.

As indicated by the Figure 4.4(a), the PFM fails to image the domains beneath the electrode area, whereas both α tilt map and the strain map successfully resolve the

domain structures under the Pt electrode. Outside the electrode, the α tilt and strain maps display high-contrast stripe patterns in AG region, that match well with the features observed with PFM.

In the α and strain maps, the domain structure under the electrode appears slightly different from that in the adjacent free as-grown (AG) region, with the stripes under the electrode showing a subtle tilt compared to the parallel stripes observed in the AG region. The domains are less ordered and well-defined underneath the electrode. This result shows that the electrode itself influences the underlying film structure, which potentially affects the performance of the device.

These examples demonstrate that nano-XRD is well-suited for imaging ferroelectric domains when the domain walls are comparable in size to the X-ray beam. This capability is particularly valuable for investigating integrated devices, where conventional PFM techniques often fall short. In Paper II, this method was further employed to study the reversal of ferroelectric domains in capacitor structures, helping to address the previously underexplored influence of electrodes and device integration on functional performance.

5 3D Strain Imaging under Angular Distortion

As mentioned in Chapter 3, any angular distortion introduced during data acquisition can lead to artifacts or even failure of phase retrieval in BCDI. This chapter introduces work focused on addressing such distortions.

First, a correction algorithm developed to mitigate these distortions is introduced, as detailed in Paper III. The performance and limitations of this approach are systematically evaluated. Following this, we present a BCDI study on a single segment of a barcode heterostructured nanowire, as described in Paper IV. In this work, a tailored data analysis strategy incorporating the proposed correction algorithm was employed to minimize the effects of possible angular uncertainty and enhance the data quality.

5.1 Likelihood-maximization Based Correction Algorithm

Adjacent diffraction slices of a 3D Bragg peak will generally be quite similar to each other. This property can be leveraged to extract orientation information within the dataset. Such an idea serves as the foundation of the expand-maximize-compress (EMC) algorithm[102,103], which is widely used to assemble diffraction slices from random orientations in a 3D diffraction volume. The EMC algorithm has been widely applied in experiments utilizing forward scattering geometries, such as those conducted with X-ray free electron lasers (XFELs), where individual diffraction must be merged to reconstruct a full 3D diffraction volume.

Unlike experiments with forward scattering geometries, where diffraction slices converge at the reciprocal origin, in BCDI, these slices are nearly parallel. Therefore, the uncertainty in sample orientation is reduced compared to forward scattering experiments. Instead of full angle variations, the primary unknown rotational components in BCDI measurements arise along three specific axes: the rocking angle θ, the roll angle ω, and the azimuthal angle ϕ.

As described earlier, the rocking angle θ systematically scans through the entire diffraction volume. Rotation in ω can shift the Bragg peak off the detector, significantly affecting data collection and quality. Meanwhile, rotation ϕ around the azimuth axis modifies the in-plane orientation of the diffraction pattern. Since a BDCI dataset is acquired from a single object, the azimuth rotation ϕ is generally assumed to be minimal to have an obvious impact on the recorded diffraction slices.

Due to the different geometry in BCDI and the negligible impact of the azimuthal rotation ϕ, the complexity of determining orientation information—specifically the rocking angle θ and roll angle ω—from the measured slices and reconstructing the 3D diffraction volume is significantly reduced. Björling *et al.* modified the original EMC algorithm and successfully implemented it in an extreme scenario in BCDI[69] where particle rotation was fully driven by the beam. The algorithm managed to recover the angles from these fully unknown and uncontrolled particle rotations and reconstruct a 3D diffraction intensity for further analysis.

In paper III, the method was further simplified by only focusing solely on θ, the most challenging direction to recognize and correct. We systematically explored how this algorithm could be applied in a scenario with both intentional and non-intentional rotations, assessing its robustness and effectiveness.

5.1.1 Theoretical Foundation for Algorithm

The algorithm seeks to reconstruct the 3D diffraction intensity volume (model) W from diffraction slices (statistical data) K, which is incomplete due to the unknown orientation in θ. This is achieved through an iterative process, where the update rule for $W \rightarrow W'$ is derived by maximizing the likelihood.

First, start with a likelihood function R_{jk}. The function R_{jk} describe the probability of observing the measured diffraction dataset K (index k), given the projection at offset positions θ (bin j) of the specific model W. Since photon detection by a pixelated detector follows a random process, one assumes Poisson counting statistics as the main noise contributor. Thus, the likelihood R_{jk} over each pixel i at the detector is expressed as:

$$R_{jk} = \prod_i W_{ij}^{K_{ik}} \exp\left(-W_{ij}\right). \tag{5.1}$$

To reduce computational effort and numerical instability, it is more convenient to calculate the logarithm of R_{jk} instead:

$$\log R_{jk} = \sum_i \left[K_{ik} \log\left(W_{ij}\right) - W_{ij}\right]. \tag{5.2}$$

The term $K_{ik}\log(W_{ij})$ in Eq. (5.2) computes the cross correlation (later sum on i) between photon counts in each measurement K and the logarithm of the model at angular offsets θ. In this context, cross correlation is a direct way to access the similarity of two data sets.

The conventional way to determine the missing orientation information is classifying the entire diffraction dataset by comparing frame-to-frame cross correlation, which is highly sensitive to noise. The criterion of noise for this conventional method introduced in Loh et al.[102] is that the number of total photon counts must be much larger than the square root of the total number of pixels. In 3D diffraction datasets, this criterion becomes significantly stricter, leading to an algebraical growth in computational complexity.

By replacing direct frame comparisons with statistical alignment in a shared model W, the algorithm remains stable even for low-photon-counts scenarios and sufficiently reduces the computational complexity. However, to accurately retrieve the implicit orientation information, the algorithm relies on sufficient oversampling, meaning that the dataset should contain enough redundancy across diffraction slices K_k.

A normalized probability P_{jk} distribution can then be calculated from the likelihood function R_{jk}:

$$P_{jk} = \frac{(R_{jk})^{\beta}}{\sum_j (R_{jk})^{\beta}}. \tag{5.3}$$

Here, β is an annealing parameter used to avoid the local optima during the iteration process. Based on the definition of P_{jk}, it can be interpreted as the orientation trajectory $\theta(k)$ to show where each single measurement K_k belongs in rocking direction θ of the 3D diffraction volume.

Due to the center-symmetry property of Fourier transform, frames at the same distance but on either side of the Bragg peak center can be very similar. As a result, the algorithm might struggle to determine whether a given single measurement K_k belongs to positive or negative side of the rocking direction, potentially introducing an artificial symmetry in the model W and resulting in an X-shaped probability matrix P_{jk}.

To break this symmetry and ensure that the trajectory $\theta(k)$ remains single-valued, a Gaussian bias with width n_σ is imposed onto R_{jk} before normalization. However, this modification introduces an assumption into the algorithm: the measurement K_k should exhibit a certain degree of continuity within the diffraction dataset.

During the iteration process, the normalized probability P_{jk} is calculated based on the current model W_j. Substituting it into the log-likelihood function from Eq. (5.2), the log-likelihood function for the algorithm can be written as

$$\sum_k P_{jk}(W_j) \cdot \log R_{jk}{}' = \sum_k \sum_i \left[P_{jk}(W_j)\, K_{ik} \log(W_{ij}{}') - P_{jk}(W_j)\, W_{ij}{}'\right] = \sum_i \left[A_{ij} \log(W_{ij}{}') - B_j\, W_{ij}{}'\right]. \tag{5.4}$$

Maximizing the log-likelihood is an optimization process[102]. Here, only the conclusion is presented: the global maximum of Eq. (5.4) is achieved when:

$$W_j' = \frac{A_{ij}}{B_j} = \frac{\sum_k P_{jk} K_k}{\sum_k P_{jk}}. \tag{5.5}$$

The Patterson function of a diffraction pattern represents the autocorrelation of the object in real space, resulting in a reconstructed volume that is twice the size of the original object. In the final step of the update process, a physical constraint is applied in real space, effectively limiting the field of view in reciprocal space. This constraint accounts for the fact that the spatial range in the q_3 (rocking direction) is generally much smaller compared to the other two directions. By imposing this constraint, the reconstruction remains physically meaningful while improving the convergence of the algorithm.

Denoting the extent in real space as D, the envelop constraint for model W can be expressed as:

$$\mathcal{F}(W'') = \begin{cases} \mathcal{F}(W'), & \text{where } |r_3| \leqq D, \\ 0, & \text{elsewhere.} \end{cases} \tag{5.6}$$

Generally, the extent D is related to the size of the object. While constraint is applied only in r_3 direction here, it is feasible to extend it to all three spatial directions when necessary.

In conclusion, a single iteration of the algorithm consists of the following steps:

1. If first iteration, generate an initial guess of the model W with Gaussian distribution.
2. Calculate the log-likelihood function $\log R_{jk}$ based on the current model W and the measured dataset K.
3. Calculate the normalized probability distribution matrix P_{jk} from the log-likelihood function $\log R_{jk}$, considering the annealing parameter β and the Gaussian bias n_σ.

4. Update the model to W' based on the update rule (Eq. (5.5)).
5. Apply the envelope constraint to get the new iterate W''.

5.1.2 Impact of Angular Uncertainty

Before investigating of algorithm's performance, it is essential to quantify the degree of unintended rotation. In paper III, this is described by the factor Γ_θ as:

$$\Gamma_\theta = \frac{< \delta\theta >}{\Delta\theta}, \tag{5.7}$$

where $\delta\theta$ represents angular perturbation at each θ position, and $\Delta\theta$ is the nominal step size of the rocking scan.

A truncated-octahedral gold nanoparticle was simulated to evaluate the performance of the algorithm. The simulation details and the subsequent phase retrieval strategy using *PyNx* software[59] are described in the paper III. A dataset with an average distortion level of Γ_θ = 2.81 (281%) was generated to demonstrate the impact of angular uncertainty and to serve as a representative example to show the effectiveness of the algorithm.

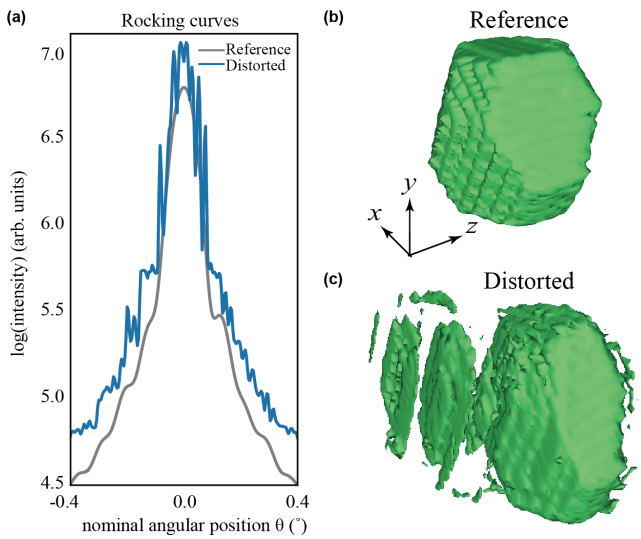

Figure 5.1 Impact of angular distortion. a) Rocking curves (*i.e.* total intensity or total photon counts over each frame) plotted in logarithmic scale as a function of nominal angle. For clarity, the curve of the distorted dataset was vertically shifted by 0.25. b) Ground-truth morphology of the simulated nanoparticle. c) Reconstruction result obtained directly from phase retrieval applied to the distorted dataset.

The angular distortion manifests as intensity fluctuations, as illustrated in Figure 5.1(a). These fluctuations lead to a poor reconstruction, with multiple side-blobs appearing in the reconstructed morphology, as shown in Figure 5.1(c). Although the main feature of this poor reconstruction still bears some resemblance to the reference, it is important to note that this example represents a relatively mild level of angular uncertainty, with the distortion level of $\Gamma_\theta = 2.81$. At the higher distortion levels, the phase retrieval algorithm may fail to converge, making it difficult to obtain a meaningful reconstruction.

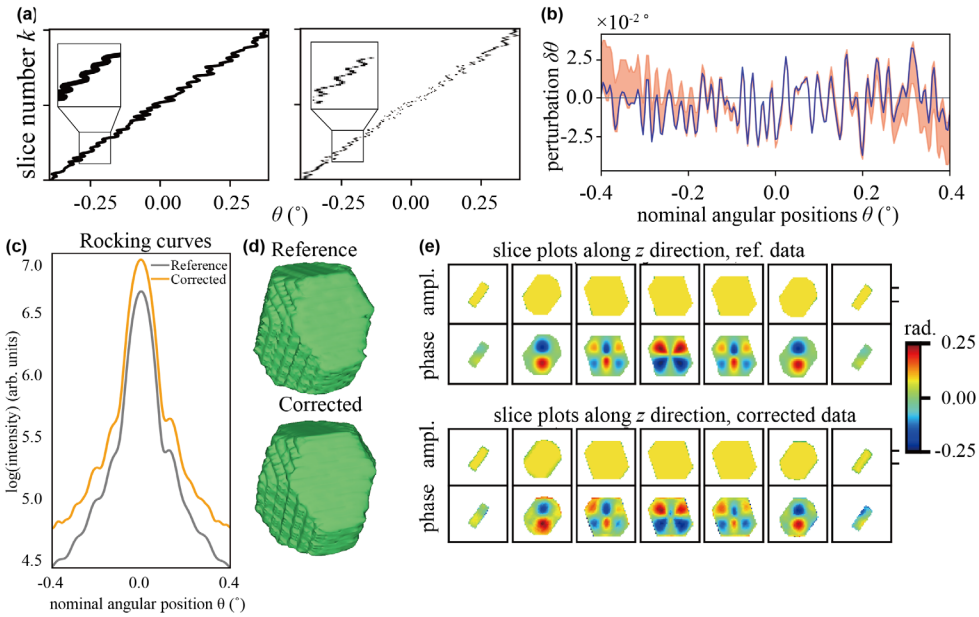

Figure 5.2 Phase retrieval result for case Γ_θ=2.81. a) Ground-truth orientation trajectory (left panel) and probability P_{jk} (right panel). b) Estimated perturbation $\delta\theta$ distribution (orange shaded area) and the ground truth (solid blue line). c) Rocking curves (*i.e.* total intensity or total photon counts over each frame) plotted in logarithmic scale as a function of nominal angle. For clarity, the curves corresponding to corrected datasets were vertically shifted by 0.25. d) Ground-truth morphology of the simulated nanoparticle and reconstructed particle morphology from the corrected dataset. e) Reference internal phase distribution (top panel) and reconstructed phase distribution (bottom panel) from the corrected dataset, shown at same positions along the z direction.

The correction algorithm was then applied to the distorted dataset. The probability matrix P_{jk}, shown in Figure 5.2(a), captures the orientation trajectory recovered by the algorithm and shows excellent agreement with the ground-truth orientations, even in fine details. As illustrated in Figure 5.2(d), the estimated perturbation $\delta\theta$ region, obtained by applying a threshold of 10^{-3} on the probability matrix, effectively overlaps with the preset $\delta\theta$. The correction algorithm benefits from the redundant information within the dataset, which is reflected in the shape of

perturbation distribution: it is narrow and well-defined in the central region, where photon counts are high, and gradually broadens toward both ends, but shows reduced accuracy in low-photon-count regions.

A similar trend is observed in the rocking curves shown in Figure 5.2(c). The corrected dataset closely matches the reference within the high-intensity rocking range $\theta = [-0.3°, 0.3°]$, while small fluctuations appear outside this central region, corresponding to lower photon-count areas.

The high intensity rocking range ($\theta = [-0.3°, 0.3°]$) from the corrected dataset was selected for phase retrieval reconstruction. As shown in Figure 5.2(d-e), the resulting reconstruction accurately recovers both the morphology and internal phase distribution of the particle, closely resembling the reference case without any angular distortion. The reconstructed harmonic phase distribution aligns well with the preset internal phase, confirming the effectiveness of the correction.

5.1.3 Investigation of the Algorithm's Robustness

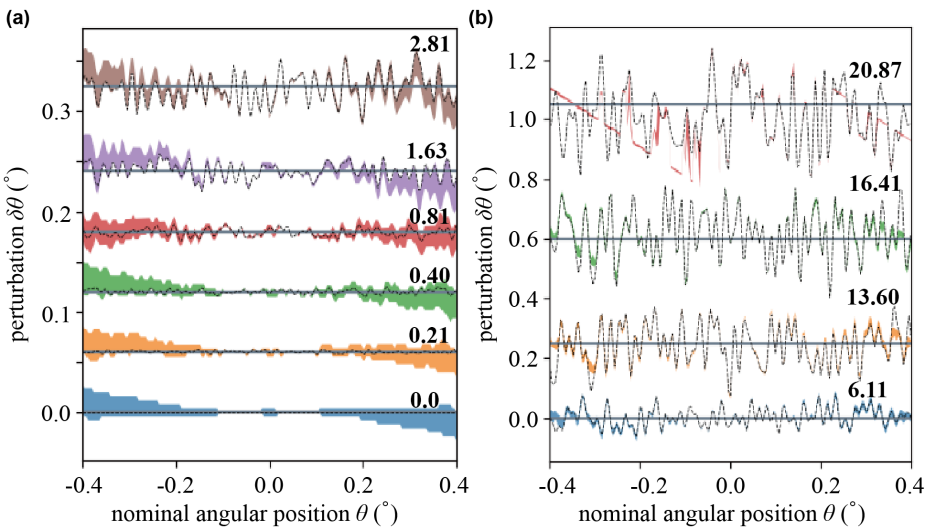

Figure 5.3 Recovered perturbation $\delta\theta$ for different distortion level Γ_θ. The angular perturbation $\delta\theta$ is shown for each frame in datasets with increasing distortion level Γ_θ, ranging from a) 0 up to 2.81, and b) further up to 20.87. For clarity, each distributions is vertically offset. The dash black lines indicate the preset $\delta\theta$ for each case, while the coloured shaded areas represent the estimated perturbation distributions calculated from probabilities P_{jk} after applying a threshold of 10^{-3}.

To evaluate the robustness of the algorithm, a series of numerical simulations was conducted across a range of distortion levels Γ_θ. These simulations span values of

Γ_θ from 0 to 20.87 and were processed by the algorithm to assess the effectiveness of algorithm under varying levels of angular distortion. For each case, the field of view in reciprocal space, defined by the parameter pair $(\mathrm{d}q_3, D)$, was adjusted accordingly to optimize the correction performance.

The perturbation distributions $\delta\theta$ shown in Figure 5.3 indicate that the algorithm performs extremely well up to the distortion level $\Gamma_\theta = 6.11$, especially in the central regions with high photon counts ($\theta = [-0.3°, 0.3°]$). For mild angular uncertainty ($\Gamma_\theta \leq 2.81$), the recovered distributions $\delta\theta$ exhibit a similar systematic linear deviation outside the central region. This behavior may stem from the imposed Gaussian bias n_σ or other high-order errors introduced during the calculation of probability P_{jk}.

For the case with even higher distortion level, the algorithm still gives a good correction result up to $\Gamma_\theta = 16.41$. At both ends of the recovered distributions, truncation effects become visible. These truncations are directly linked to the field of view defined by the parameter pair $(\mathrm{d}q_3, D)$. They demonstrate that, in these cases, the diffraction datasets cover a larger reciprocal space than expected. This phenomenon is particularly pronounced at $\Gamma_\theta = 20.87$, where the trajectory $\theta(k)$ can almost be considered as random. Nevertheless, even under such an extreme scenario, the algorithm successfully recovers the central portion of the dataset, where the photon counts are higher.

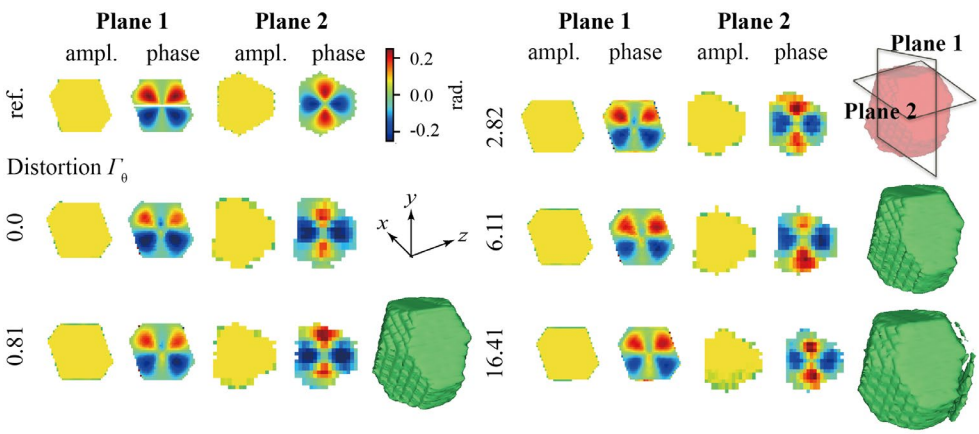

Figure 5.4 Phase retrieval reconstruction for different levels of distortion Γ_θ. Plane 1 and Plane 2 show two perpendicular slices through the particle. Plane 1 corresponds to the central cross-section, while Plane 2 is slightly offset from the center to better highlight phase features.

The high intensity rocking range ($\theta = [-0.3°, 0.3°]$) from the corrected datasets was selected for phase retrieval reconstruction. As shown in Figure 5.4, the resulting

reconstructions exhibit consistent morphology and internal phase across different distortion levels, demonstrating the robustness of the algorithm.

Readers interested in more details, including intentioned angular uncertainty under fly scan mode and the distortion cases considering Poisson noise, are referred to Paper III.

5.2 Strained Single Segments in Heterostructured Nanowire

As discussed earlier, lattice mismatch at heterointerfaces can induce strain, which in turn shifts the electronic bandgap. While this strain can be engineered to improve device performance, it also risks creating defects when the mismatch exceeds the coherency limit.

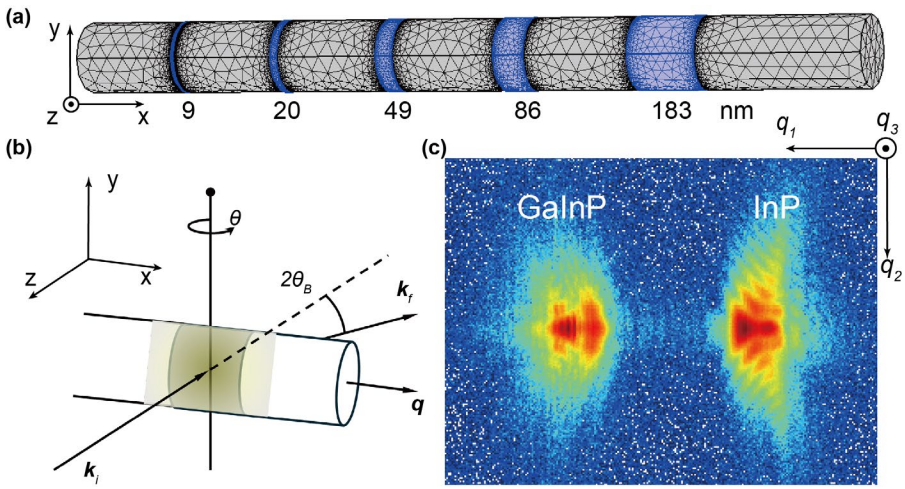

Figure 5.5 Illustration of BCDI for an axially heterostructured nanowire. a) Schematic of a single barcode-type InP/GaInP nanowire. The nanowire consists of 5 InP segments with varying lengths along the axial direction. b) Geometry for BCDI measurement. The yellow shaded area denotes the area illuminated by the focused coherent X-ray beam. c) Logarithmic-scale integrated diffraction pattern for a single angular scan. Note that the coordinate system appears flipped compared to the setup in (b), due to the inverted mounting configuration of the detector at the NanoMAX beamline.

In Paper IV, Bragg Coherent Diffraction Imaging (BCDI) with a nanofocused X-ray beam was applied to investigate a single InP/$Ga_xIn_{(1-x)}P$ axially heterostructured nanowire. Its bandgap can be tuned from the near infrared to the visible range by

adjusting the gallium composition, making these structures highly promising for photovoltaic applications.

The nanowire studied in this work has a reported gallium composition of $x = 0.21$, corresponding to a nominal mismatch of 1.52% - close to the predicted limit for defect formation[79]. Under such conditions, probing the internal strain distribution becomes critical for understanding material behavior and guiding device design.

In addition to its technological relevance, this sample offers a practical advantage for BCDI measurements. Typically, BCDI requires isolated samples to avoid interference effects under a coherent beam. However, as shown in Figure 5.5(a), this nanowire has 5 InP segments embedded in a GaInP matrix, with varying segment lengths along x- direction. Although these segments cannot be physically separated in real space, the difference in lattice constants between InP and GaInP allows their respective Bragg peaks to be well separated in reciprocal space, as illustrated in Figure 5.5(c). This makes it possible to isolate and analyze diffraction from individual InP segments.

This section presents the work published in Paper IV, where the internal 3D strain distribution of the largest InP segment with approximately 180 nm length along the growth direction ([111]) is reconstructed and analyzed.

5.2.1 Data Processing

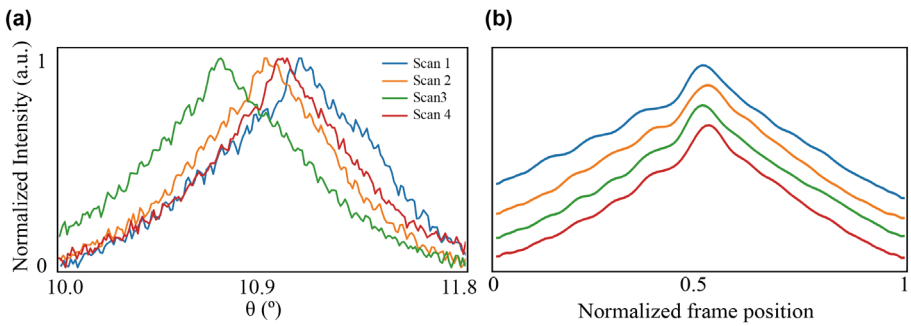

Figure 5.6 Observed spontaneous particle rotations. a) Rocking curves of the raw datasets collected from different scans. b) Rocking curves of the corrected datasets after applying correction algorithm to the corresponding raw datasets. A vertical shift of 0.15 was applied for clarity.

As illustrated in Figure 5.5(b), multiple rocking scans were performed on the same InP segment under identical experimental conditions. Figure 5.5(c) displayed the integrated diffraction pattern for one of these scans. Since the lattice constant of InP (a_{InP}) is larger than that of the GaInP (a_{GaInP}), the Bragg peak at high Q (left)

corresponds to the adjacent GaInP segments, while the diffraction pattern at low Q (right) originates from the targeted InP segments. In the following, only the diffraction corresponding to InP will be discussed.

Figure 5.6(a) shows the rocking curves obtained from each scan. Although all scans were performed under identical experimental conditions and targeted the same InP segment, a significant angular shift along the rocking direction (θ) is clearly observed. A possible explanation for this shift is the torque induced by the beam pressure, which could cause the nanowire to rotate. This is reasonable considering that the nanowire is only weakly fixed to the Si_3N_4 window by van der Waal forces.

Additionally, periodic fluctuations with an approximate spacing of 0.05° can also be observed in the rocking curves for the raw datasets. Considering the experimental geometry, a 0.05° oscillation in the rocking direction corresponds to about 370 nm in the real space, roughly center to center distance of two InP segments. Therefore, these fluctuations are attributed to interference effects from neighboring InP segments, caused by the long tail of the incident beam.

To mitigate the possible impact from the angular shifts, the correction algorithm introduced in the previous section was applied to the raw datasets. The resulting rocking curves of the corresponding corrected datasets are plotted in Figure 5.6(b). After correction, similar features align consistently among the corrected datasets. From the perspective of signal processing, the constraint on Patterson function of the diffraction datasets (Eq. 5.6) acts effectively as a low-pass filter, suppressing high-frequency components and thereby reducing the observed fluctuations.

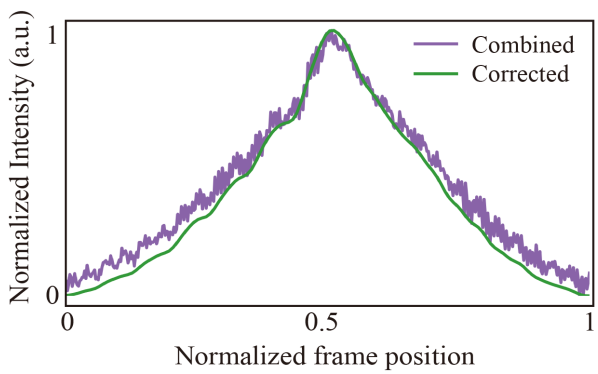

Figure 5.7 Merging datasets. The purple rocking curve corresponds to the combined dataset. After combination, the correction algorithm was applied to the combined dataset. The green rocking curve represent the resulting corrected dataset.

Apart from directly applying the correction algorithm to each individual scan, a merging strategy was proposed to further enhance data quality. Since all scans

measured the same InP segment and showed similar features after correction, the raw datasets from scans 2–4 were selected for merging. The frames were aligned based on their relative angular positions, as illustrated in Figure 5.7. Merging the datasets can in principle increase the signal-to-noise ratio and provide greater redundancy of information, which improves the robustness of the reconstruction. After merging, the correction algorithm was applied to the combined dataset. The resulting rocking curve shows good agreement with those from the individually corrected scans.

5.2.2 Reconstruction and Strain Analysis

Here, the scan 3 dataset was selected as a representative example. The *PyNx* software was employed to perform phase retrieval reconstructions on the raw (uncorrected) scan 3 dataset, its corrected dataset, and the corrected combined dataset.

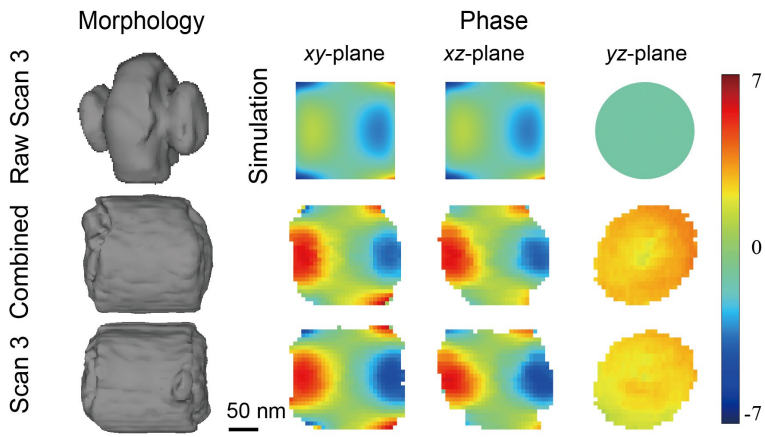

Figure 5.8 Reconstructions obtained from phase retrieval algorithm. The phase has been unwrapped for all datasets.

As shown in Figure 5.8, the reconstructed morphologies from both corrected scan 3 dataset and corrected combined dataset accurately preserve the cylindrical feature of the nanowire, demonstrating a significant improvement in data quality compared to the reconstruction from the raw (uncorrected) scan 3 dataset. Additionally, reconstructions from the corrected datasets exhibit similar unexpected features: Instead of sharp, flat interfaces, the middle section appears slightly elongated compared to the region near the surface. The estimated spatial resolutions for these reconstructions are approximately 14 nm and 13 nm in the x- and y- directions, respectively.

The reconstructed phase distributions from corrected datasets are also shown in Figure 5.8. For comparison, a *Finite Element Method* (FEM) simulation, conducted using the commercial software COMSOL, is presented alongside. Details of simulation setup and parameters are described in Paper IV. Both reconstructed phases successfully recover the harmonic variation observed in the central region and at the corners, consistent with the FEM result. However, the reconstructed phase range (–3.8 to +5.6) is broader than that of the simulation (–3.5 to +1.1).

The strain distribution was obtained from the phase distribution using Eq. 3.16, as shown in Figure 5.9(a). The calculated strain distributions from the reconstructed phases show excellent agreement with the simulation. In general, a sign reversal is observed between the central region and the edges, accompanied by a gradual strain variation toward the center along the top and bottom boundaries. Although the simulation predicts symmetric strain distributions in xy- and xz- planes in the simulation, the reconstructed strain distribution in xz - planes shows more asymmetry. This deviation is likely attributed to an inhomogeneous gallium distribution, leading a slightly higher lattice mismatch on one side of the nanowire.

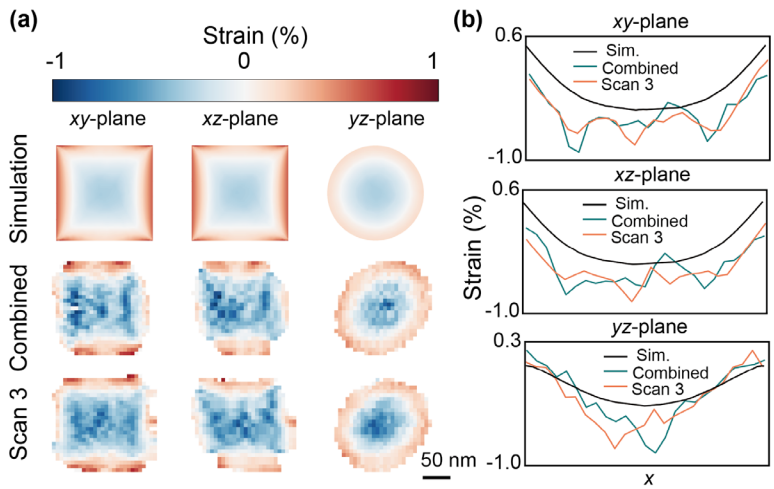

Figure 5.9 Reconstructed strain distribution. a) 2D strain maps extracted from the reconstructed 3D phase distributions.b) Lineouts of the strain distributions calculated from: center for xy- and yz- planes and slight offsets from the center for xz- plane.

The lineouts shown in Figure 5.9(b) clearly indicate that the experimentally reconstructed dataset exhibits a higher strain magnitude compared to the simulation. In the xy- and xz- planes, the average reconstructed strains in the central region are around -0.5%, compared to -0.3% in the simulation. In the yz - plane, the reconstructed strains are closer to the simulated value, with an average of -0.4% compared to -0.25%. The larger measured strain is consistent with the broader phase

variation discussed above. This difference is likely attributed to a higher actual average gallium composition in the nanowire than the nominal value of 21%, leading to an increased mismatch.

The skewing observed in the yz- plane in Figures 5.8 and 5.9 is attributed to the unintended spontaneous rotation of the sample around the rocking axis. Such rotation leads to a deviation from the correct Bragg angle θ_B, which is critical for the rectification process. As a result, a geometric distortion appears in the reconstructed real-space object. A detailed investigation of this skewing effect, together with the FEM simulations, phase retrieval strategy, and reconstructions from other scans, is presented in Paper IV.

6 Bragg CDI for Unknown Angles with Deep Learning

Consider a scenario in which the measured object in a Bragg coherent diffraction imaging (BCDI) experiment is extremely unstable. The resulting spontaneous rotations drive the object in and out of the Bragg condition very quickly, allowing only a few diffraction slices to be collected during a single rocking scan. Even worse, these collected slices correspond to unknown orientations, further complicating the subsequent analysis process. Such scenarios are becoming increasingly common as more complex in-situ BCDI experiments are performed using advanced facilities like 4th-generation synchrotron sources and X-ray Free Electron Lasers (XFELs).

The correction algorithm introduced in the previous chapter is capable of effectively handling the dataset with angular distortion. However, the approach does require a certain degree of continuity in the angular sampling. This limitation makes the method unreliable for datasets with completely random orientations, such as the scenario described above.

Meanwhile, deep learning techniques have demonstrated outstanding capabilities in handling complex data within the field of X-ray imaging. Recent published studies have shown its successful applications in 2D and 3D phase retrieval[104,105], as well as in 4D imaging for X-ray computed tomography[106,107]. Moreover, deep learning has been employed to enhance data quality, including denoising[108] and correcting artifacts[109]. This broad applicability stems from the ability of deep neural networks (DNNs) to automatically extract meaningful features from raw data and learn complex mappings to desired outputs.

Given its remarkable potential, deep learning presents a possible solution to solve the challenge of completely unknown or random orientations in BCDI datasets. In our sketch, the trained neural network (NN) is designed to independently predict the angular orientation of individual diffraction slices. Rather than treating the BCDI dataset as a single coherent volume, analyzing each frame independently introduces greater flexibility and robustness to the subsequent reconstruction process.

This solution lays the groundwork for a new data acquisition strategy, which we refer to as serial BCDI as mentioned in Paper V. In this method, diffraction data is collected from single or multiple identical objects. Statistically, if a sufficient

number of diffraction slices with random orientations are collected, they can together cover the full diffraction volume and meet the sampling condition. This strategy has the potential to relax the strict experimental constraints of conventional BCDI and may further extend its use to pump-probe experiments using XFELs, which offer outstanding high temporal resolution.

In Paper V, the feasibility of this approach is demonstrated. A neural network was trained to predict the angular orientation of individual diffraction slices in the serial BCDI setting, focusing on the rocking direction (θ). Combined with the correction algorithm introduced earlier, our method shows promising results in reconstructing the diffraction volume. The potential to extend this method to predict both azimuthal and rocking angles was also explored in Paper V.

The rest of this chapter introduces the basic concepts of deep learning and explains the proposed strategy in more detail.

6.1 Basic Concept of Deep Learning

In our daily life, you can easily find the trace of artificial intelligence (AI). One familiar example is voice assistants such as Siri, Alexa, or Google Assistant. When you say, "Hey Siri", "OK Google" or "Alexa", the program recognizes the *wake words* and makes a simple prediction, yes or no, to activate the assistant. If you then say, "Call my mother", the machine not only understands the action "call" and the object "mother," but can also associate "mother" with the correct person in your contacts, even if you haven't explicitly labeled someone as "mother" in your phone. This capability relates to machine learning, where the system extracts relevant features from the data and makes the predictions based on them. However, in traditional machine learning, feature selection often relies on human input. Thus, the final prediction might be strongly biased by the human.

Tools like ChatGPT, Claude or Gemini can generate human-like responses and process more complex tasks than the voice assistant. These advancements are made possible by deep learning, a subset of machine learning. Deep learning[110,111] relies on deep neural networks (DNNs) to process vast amounts of data and automatically learn meaningful representations. It is a data-driven technique. For example, the neural networks behind ChatGPT require an incredibly large amount of high-quality data to understand language and context at a deep level, which also demands powerful hardware. In fact, although the concept[112] of deep learning dates back to the 1950s, it didn't gain widespread attention and rapid development until the introduction of AlexNet[113] in 2012. The success of AlexNet, and deep learning itself, was made possible by access to large, high-quality datasets like ImageNet[114] and the growing use of graphics processing units (GPUs), marking the beginning of the "big data era." Recognizing the transformative impact of these developments, the 2024

Nobel Prize in Physics was awarded to J. J. Hopfield and G. Hinton, whose pioneering contributions[115,116] laid the foundation for today's AI revolution.

In mathematical terms, the deep learning process can be formulated as an optimization problem. It aims to find the optimal set of parameters (ξ) for a neural network that minimizes the difference between its predictions and the target outputs. This difference is quantified by a loss function $\mathcal{L}$, which measures the expected error over the input data. A typical expression of $\mathcal{L}$ is

$$\mathcal{L}(\xi) = \mathcal{E}_{\boldsymbol{x},\boldsymbol{y}\sim p_{\text{data}}} L(f(\boldsymbol{x},\boldsymbol{\xi}),\boldsymbol{y}), \tag{6.1}$$

where $f(\boldsymbol{x},\boldsymbol{\xi})$ represents the prediction made by the network for the input $\boldsymbol{x}$, while $\boldsymbol{y}$ is the ground truth or target output. L is the specific loss function (e.g. mean squared error or cross-entropy) used to evaluate the prediction error for each sample. $\mathcal{E}_{\boldsymbol{x},\boldsymbol{y}\sim p_{\text{data}}}$ denotes the expectation over the true data distribution p_{data}. This expectation can be interpreted as a weighted average, where each sample's contribution to the total loss $\mathcal{L}$ is implicitly weighted by its likelihood under the data distribution.

The choice or design of the loss function $\mathcal{L}$ is crucial in determining the performance of the network, and it is typically task-oriented. Once the loss function is defined, the process of minimizing it is referred to as the *training* process. During training, the parameter set (ξ) is iteratively updated toward an optimal solution using optimization methods such as backpropagation and gradient descent. The size of each update step is controlled by a parameter known as the *learning rate*. Because datasets are often large, it is common practice to divide them into smaller subsets called *batches*. Batch training not only accelerates computation but can also help the model escape local minima by introducing stochasticity into the optimization. A full pass through the entire training dataset is referred to as an *epoch*.

6.1.1 Supervised Learning and Unsupervised Learning

Deep learning can be further categorized into *supervised learning* and *unsupervised learning*, depending on the data used to train the model. As the name suggests, supervised learning involves training on a dataset that includes both input data and corresponding labels. The model learns to map inputs to their correct outputs and is then used to predict labels for new, unseen data. In contrast, unsupervised learning involves only input data without any labels. The neural network attempts to uncover hidden patterns or relationships within the data on its own.

In supervised learning, the input data is typically divided into three subsets: training, validation and test datasets. The model is trained using the training dataset while the validation dataset is used to tune model parameters and select the best-performing version of the model. Finally, the test dataset, which should be completely unseen

by the model during training process, is used to evaluate its generalization performance. On the other hand, unsupervised learning doesn't require the input data to be divided. The entire dataset can be used in both training and evaluation.

Given the nature of these two learning types, supervised learning typically offers faster training and higher accuracy for well-defined tasks, while unsupervised learning tends to be more flexible and generalizable, making it better suited for complex or poorly defined problems where labeled data is unavailable. In Paper V, a supervised learning approach to train the neural network as adopted.

6.1.2 Deep Neural Networks

Deep neural networks (DNNs) are the core computational models behind deep learning, enabling machines to automatically extract relevant features from raw data and make complex predictions. In this section, two fundamental layered model architectures, fully connected networks and convolutional neural networks (CNNs), are introduced and discussed.

Fully Connected Networks

The basic unit of a fully connected networks is called a neuron, also known as a perceptron. The calculation processed in a neuron can be expressed as

$$y = f(\boldsymbol{w} \cdot \boldsymbol{x} + b), \tag{6.2}$$

where $\boldsymbol{x}$ represents the input vector, $\boldsymbol{w}$ is the corresponding weight vector and b is the bias term. The output y is obtained by applying an activation function f to the weighted sum of inputs and bias. This process is illustrated in Figure 6.1(a).

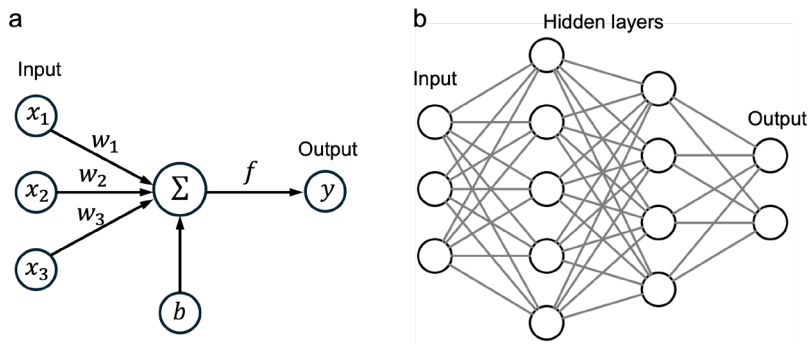

Figure 6.1 Schematic of a fully connected network. a) Illustration of a neuron. The input vector consists of three elements (x_1, x_2, x_3), and the weight vector includes the corresponding weights (w_1, w_2, w_3). b) An example of fully connected network with three inputs nodes, two hidden layers and two outputs nodes. Every neuron in a layer is connected to every neuron in the adjacent layer.

Figure 6.1(b) shows an example of multi-layer fully connected network, also referred as to multi-layer perceptron (MLP)[117]. In a neural network, nodes at the same depth form one layer. The role of a node depends on its layer: in the input layer, each node represents one element of the input data; in the output layer, each node corresponds to one output value; in the hidden layers, nodes are often referred as to neurons.

As illustrated in Figure 6.1(b), the output of each neuron serves as the input to neurons in the adjacent layer. If the activation functions are linear, the entire network reduces to a single linear transformation, and the final output becomes a linear combination of the input elements. This severely limits the capability of the network to model complex, nonlinear relationships in the data. By contrast, the introduction of nonlinearity through activation functions allows the MLP to act as a universal approximator, which can approximate any continuous functions. Common activation functions include the sigmoid function, rectified linear unit (ReLU), and the softmax function. The selection of appropriate activation functions depends on the specific task and the desired output behavior.

For image data, such as the diffraction data discussed in this thesis and in Paper V, fully connected networks (or MLP) are not ideal. In an MLP, each node is connected to every node in the adjacent layer, resulting in a large number of parameters. This dense connectivity demands significant computational resources and can quickly lead to memory issues, especially when processing high-dimensional data like images. Furthermore, the architecture of MLPs inherently treats all input features independently and equally, ignoring the spatial structure and local correlations inherent in image data. Adjacent pixels in an image often contain related information. Ignoring these local dependencies not only prevents MLPs from effectively capturing meaningful features but also leads to unnecessarily complex models.

Convolutional Neural Networks

Convolutional neural networks[118] (CNNs) are specifically designed to capture local correlations and hierarchical features[119] in data, making them particularly effective for spatially structured inputs such as images or diffraction patterns.

The basic architecture of a CNN model, as illustrated in Figure 6.2(a), involves two types of layers: convolution and pooling. Feature maps are generated by applying convolution kernels to the input data in the convolution layer. These feature maps are then downsampled into pooled feature maps through max pooling operations in the pooling layer. The number of feature maps at each stage corresponds to the number of different kernels included in one convolutional layer. The use of convolutional kernels and pooling layers not only reduce the computing demands but also effectively captures multi-scale features from local to global.

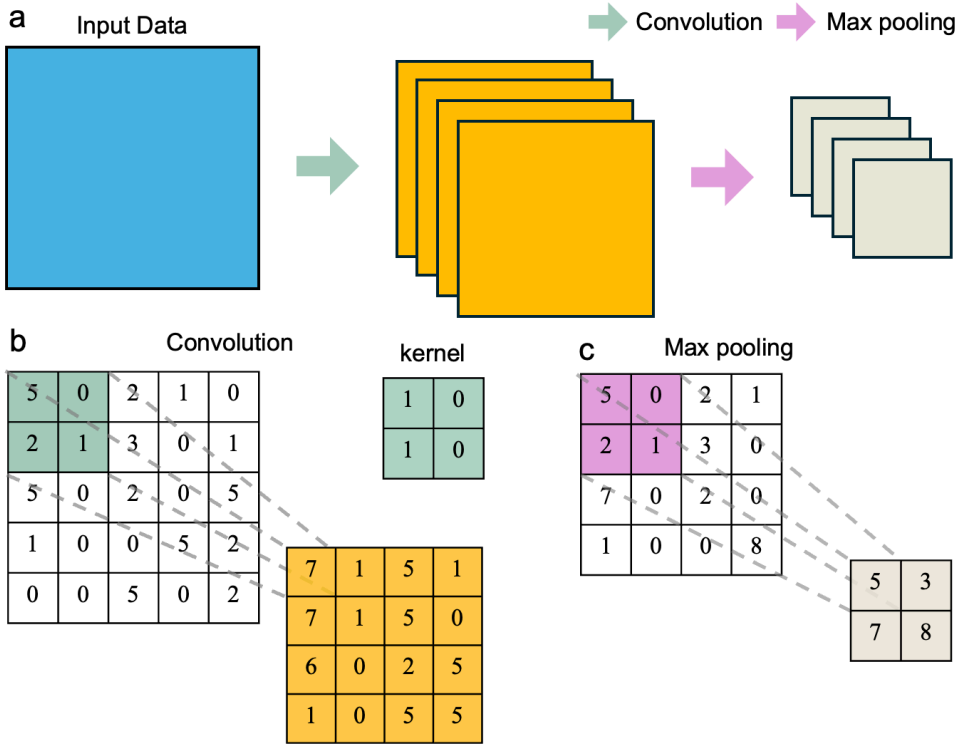

Figure 6.2 Convolution neural network. a) Basic architecture of a CNN. Different colors represent different types of data: blue means the input data; orange is the feature map after convolutional operation; beige denotes the pooled feature map after pooling (downsampling) operation. b) Illustration of convolutional operation. The matrix with white background is the input. The beige-shaded area indicates the region where the convolutional kernel is applied. The isolated 2×2 brown matrix is an example of the convolution kernel. c) Illustration of max pooling operation. The dark-shaded area is an example region where max pooling is applied.

Figure 6.2(b–c) illustrate examples of convolutional and pooling operations. A convolutional kernel performs element-wise multiplication over a local region of the input, followed by summation, to produce a single value in the output feature map. The complete feature map is obtained by sliding the kernel across the input data, and this stepwise movement is controlled by a parameter called the *stride*. Interestingly, although referred to as a "convolutional" kernel, the operation is technically a cross-correlation rather than a true mathematical convolution. Typically, the resulting output feature map is smaller than the input unless padding is applied to preserve the spatial dimensions. The pooling operation further reduces the dimensionality of the feature map by binning the elements. One of the most commonly used methods is max pooling, which selects the maximum value within each sub region to represent that area in the downsampled output.

In Paper V, a CNN was used as an encoder to extract the features from the diffraction data, while a subsequent MLP was employed to predict the orientation information of the input diffraction pattern based on the extracted features.

6.2 Orientation Prediction Using Neural Network

Based on convolutional neural networks and fully connected layers, the model's architecture is illustrated in Figure 6.3. Each convolutional layer contains multiple distinct 3×3 kernels and is followed by a batch normalization operator. Batch normalization helps stabilize and accelerate the training process by normalizing the output of each layer to have a consistent mean and variance, which prevents large shifting in the data as it passes through the network. The activation function used in both the convolution and the fully connected layers is ReLU.

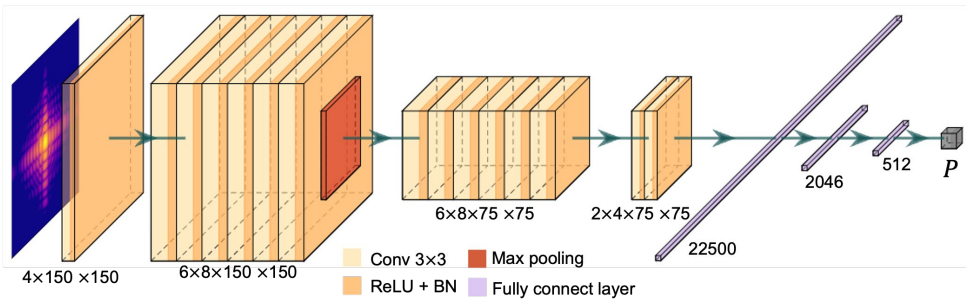

Figure 6.3 Neural network architecture. The model begins with an encoder that extracts features from the input data. These features are then passed through a multilayer perceptron to predict the angular position of the input diffraction pattern.

Returning to the scenario described at the beginning of this chapter, the dataset collected under such conditions consists of diffraction slices with completely random orientations. This poses a significant challenge for the EMC angular correction algorithm introduced in the previous chapter, as it relies on continuity between frames. The strategy proposed in Paper V aims to predict the angular orientation of each individual diffraction using the network described above. These predicted orientations are then used to assemble the full 3D diffraction volume from the set of randomly oriented frames.

Since large amounts of real experimental data are not accessible for training, a simulation-based method was adopted in Paper V to generate the training dataset. A key challenge in this method is bridging the gap between simulated data and real experimental data, particularly in ensuring the model trained on synthetic data can generalize effectively to real diffraction measurements.

Several key factors have been considered in designing the simulation approach. Each factor poses specific demands on the robustness and effectiveness of the network.

The first is the shape of the object, as it largely determines the overall diffraction pattern. In the proposed approach, the 3D shape of object used for simulation can be obtained from other complementary method, such as scanning electron microscopy (SEM) or by assuming an idealized morphology. However, differences between the simulated shape and the true object may directly affect the performance of the network.

Another important factor is the phase distribution, which introduces local variations in the diffraction pattern. While the overall shape of a sample can often be estimated from complementary techniques, accessing the internal phase distribution of a real object remains highly challenging. Therefore, the network must be capable of generalizing to "unseen" phase distributions that were not part of the training data.

The final factor considered is the signal-to-noise ratio (SNR). The measured diffraction intensity depends on the flux intensity and the possible air scattering and absorption. From an information theory perspective, each detected photon in a diffraction pattern contributes with information. Therefore, the SNR directly impacts the information encoded in the diffraction pattern and thus affect the performance of the network.

In Paper V, the network's robustness with respect to these factors was systematically studied. The model showed tolerance to moderate variations in object shape. For the SNR challenge, the network was trained using datasets with noise levels matched to experimental conditions. To address the unseen phase problem, the training dataset included a variety of phase distributions to help the network generalize.

6.2.1 Performance on the simulated data

To assess the baseline performance of the proposed method, it was first applied to a noiseless dataset composed of diffraction slices with completely random rocking angles θ. The results are presented in Figure 6.3.

The predictions shown in Figure 6.3(c) deviate noticeably at both ends of the preset rocking angle range, while exhibiting a more linear trend in the central region. This behavior is also reflected in the cross-section of the CNN-processed dataset. Although the overall diffraction pattern appears smooth and continuous, the prediction inaccuracies at both ends lead to local fluctuations in the reordered data.

The mismatches in the predictions are primarily attributed to differences in shape between the simulated morphology used for training and the actual ground truth. Although the predictions are not perfectly accurate, the network still achieves a significant improvement by imposing a certain degree of order on an otherwise

completely random dataset. The continuity shown in the CNN-processed dataset enables the subsequent application of the EMC angular correction algorithm discussed in the previous chapter, providing a chance to further refine the reordered data and improve the result.

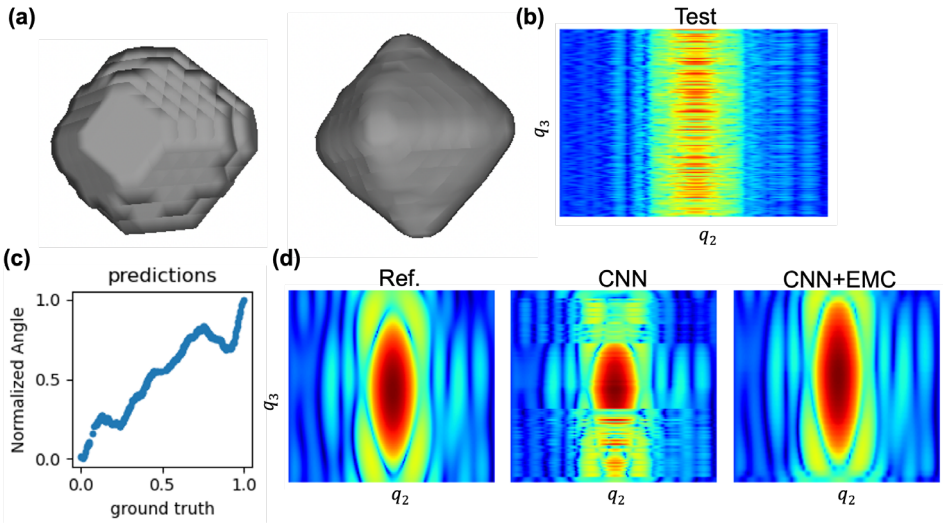

Figure 6.3 Network performance on simulated dataset. a) Ground-truth particle and ideal particle. The test data was generated from the ground-truth particle illustrated at the left, while the training data was generated using the ideal particle shown at the right. Both training data and test data are noise-free. The test data contains one single phase distribution that is distinct from any phase distributions used in training. b) Cross-sectional plot along the rocking direction q_3 of the test data. c) Normalized rediction results from the NN. d)Cross-section plots along the rocking direction q_3 of different datasets. The reference was generated with ordered rocking angles θ from the ground-truth particle shown in (a). Note that the CNN-process predicts the angle of each frame individually, unlike the EMC angular correction algorithm. The corrected data (CNN+EMC) was produced by applying the EMC angular correction algorithm to the CNN-processed data.

In Paper V, the EMC angular correction algorithm presented was applied to the CNN-processed dataset, and it proved to be highly effective in further improving the data quality. As shown in Figure 6.3(d), the cross section of the corrected dataset after angular correction shows a strong alignment with the reference. The slightly narrower field of view was from the setting of the correction algorithm.

6.2.2 Experimental Serial Bragg Coherent Diffraction Imaging

The proposed strategy worked successfully on simulated data with the assistance of the EMC angular correction algorithm. It is now time to evaluate its effectiveness on real experimental data. For this purpose, the network was trained on a dataset with a SNR matched to that estimated from the real experimental measurements.

The BCDI experiment was conducted on (111) reflection planes of 60 nm gold particles. The data were collected by Alexander Björling at the NanoMAX beamline, MAX IV Laboratory, Sweden, and they were also used for the first paper using the EMC angular correction algorithm[69]. Unlike the regular BCDI, this measurement relies on the spontaneous rotations of the small particles by the intense flux. Björling and his colleagues reported that such spontaneous rotations in θ can cover the entire diffraction volume. In this measurement, the detector mode operated at burst mode with 100 Hz frame rate. The gold particles, assumed to be identical, were mounted on a sample holder and spatially scanned in both the x- and y-directions with a step size of 0.1μm, controlled by piezo motors. At each position, the detector collected 1000 frames. A post-processing program was used to extract sufficient diffraction dataset by selecting continuous diffraction slices.

Two datasets from the experiment were used to evaluate the proposed strategy presented in Paper V. Figure 6.4 shows one of the datasets as an example.

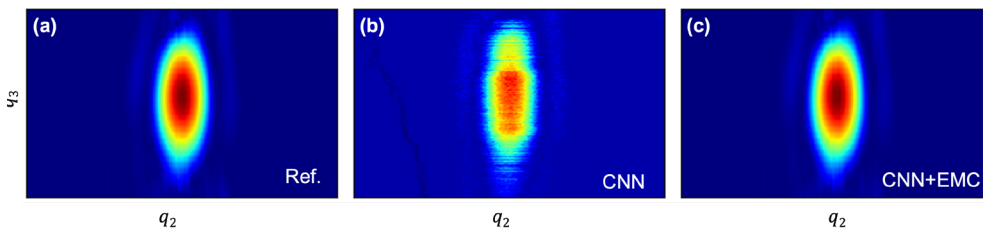

Figure 6.4 Network performance on experimental data. The cross-section plots along rocking direction q_3 for different datasets: a) the reference dataset, b) the CNN-processed dataset and c) the corrected dataset processed by CNN and EMC angular correction algorithm.

The reference dataset was generated by applying the EMC angular correction algorithm directly to an experimental dataset, in which the frames were sampled continuously. To test the CNN approach, each frame from the raw dataset was processed individually to estimate its corresponding θ position. The CNN-processed dataset was then obtained by combining the frames based on these predicted positions. Compared to the reference, the CNN-processed dataset already shows a good overall alignment, though minor fluctuations remain due to residual prediction errors. After applying further refinement using the EMC angular correction algorithm, the corrected dataset aligns very closely with the reference. The results shown in Figure 6.4 highlight the promising performance of this combined approach.

Since the diffraction slices collected in this measurement are, in principle, from identical particles, the concept of serial BCDI was explored by merging the raw diffraction slices from the two datasets and randomizing their order, before any processing by the proposed strategy. The merged dataset was then used to test the

strategy, while the reconstruction from original datasets (particle 1 & particle 2), processed by the proposed strategy and the correction algorithm, served as the reference.

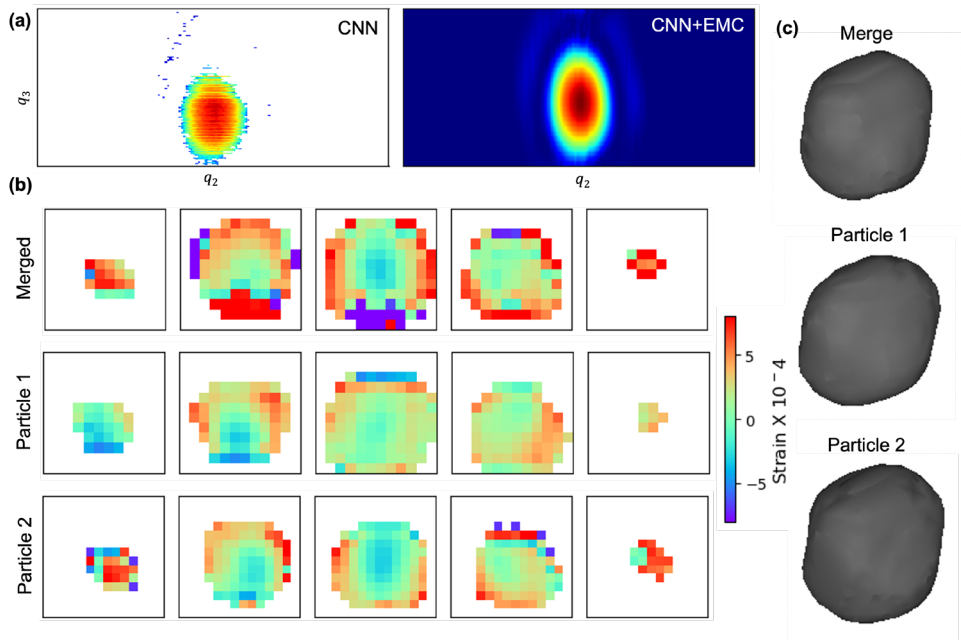

Figure 6.4 Network performance on serial BCDI-type data. a) Cross-section plots along rocking direction q_3 for different datasets. c) Slices of the reconstructed strain distribution from the corrected dataset (CNN+ EMC) and its original datasets after being processed by the proposed strategy. c) Reconstructed morphologies for different datasets obtained after phase retrieval. The parameters used in the phase retrieval are the same for all datasets.

As indicated by the cross-section plots in Figure 6.4(a), the predictions from the network successfully reordered the raw input datasets. The CNN-processed dataset reveals a generally correct diffraction pattern, although some fluctuations remain. The long tails and irregular (compressed-like) shape observed in the corresponding cross-section plot are attributed to unequal step sizes between adjacent frames. After refinement using the correction algorithm, the reassembled dataset demonstrates enhanced data quality.

The reconstruction of the CNN+EMC dataset obtained through phase retrieval is shown in Figure 6.4(b-c). The reconstructed morphology exhibits very similar features to the reference as shown in Figure 6 (particle 1) and S10 (particle 2) of Paper V. Compared to the reference, the reconstructed strain distribution appears to be grainier at edges. This noise might originate from the differing intensities of two

original datasets as shown in Figure S10 of Paper V. Aside from this, the reconstructed strain shows similar gradient-like distribution to that of the references.

The example shown above demonstrates the potential of a deep learning-based approach, combined with angular correction, to handle complex data that would be expected in a serial BCDI experiment. In this work, we focused only on the rocking angle θ. However, Paper V also explored the model's performance with respect to additional azimuthal angles ϕ, which represents the next step toward refining this approach for full serial BCDI applications. The success of this method relaxes experimental constraints in conventional BCDI measurement and increased the robustness of BCDI to the extreme experimental conditions. We believe it opens significant opportunities for advancing the science, particularly in fields such as material science and catalyst.

7 Conclusions and Outlook

In this thesis, I have illustrated the capabilities of synchrotron-based X-ray diffraction imaging techniques, specifically, nano-XRD and BCDI, for probing the internal structure of crystalline materials. In particular, methods to address the angular distortion problem in BCDI have been introduced.

To begin, I presented studies using nano-XRD on axially heterostructured nanowires and ferroic thin films. These works demonstrate that nano-XRD not only enables quantitative mapping of lattice spacing and tilt but also the imaging of ferroic domains with a resolution defined by the focused beam size. Notably, nano-XRD is particularly effective in scenarios where conventional microscopy falls short. For instance, nano-XRD can image ferroelectric domains beneath metallic electrodes, where techniques such as piezoresponse force microscopy (PFM) are ineffective.

A major component of this work is the development of a robust algorithm to correct angular distortions in diffraction datasets. This method significantly improves the reliability of BCDI in scenarios involving intense beam flux, heating from nano-focused synchrotron radiation, or external factors such as sample charging. Notably, the algorithm remains effective even when angular deviations reach up to 16.4 times the nominal rocking increment.

This correction method was also applied in the study of a single segment within a barcode heterostructured nanowire. Although BCDI is generally challenging to apply to extended samples, the well-separated Bragg peaks resulting from lattice mismatch between the segments made the measurement feasible. The reconstructed 3D strain distribution revealed a unique gradient pattern in excellent agreement with finite element method (FEM) simulations. A merging strategy was also employed alongside the angular correction to enhance the quality of the phase retrieval reconstruction.

Another key advancement presented in this thesis is a deep learning–based strategy to predict the angular positions of individual diffraction frames. When combined with the angular correction algorithm, this approach enables reconstruction of a 3D diffraction volume from frames acquired in completely random order. I demonstrated this method on a serial BCDI-type dataset, created by merging two datasets from identical particles. The success of this approach shows strong

potential for relaxing the strict data acquisition requirements in BCDI, thus enabling its use under extreme or dynamic experimental conditions.

Looking forward, the ongoing transition to fourth-generation sources will provide even brighter and more coherent X-ray beams. Advances in X-ray optics and detector technology allow for smaller spot sizes and more sensitive diffraction measurements. Together, these developments will push the resolution and applicability of both nano-XRD and BCDI further.

For BCDI in particular, the methods presented in this thesis (Papers III, IV, and V) establish a foundation that empowers the technique to operate under more complex and challenging experimental conditions. More importantly, they also provide a roadmap toward a new data acquisition and processing method, serial BCDI, which has potential to enable more versatile and comprehensive structural investigations.

One envisioned application of serial BCDI is the study of catalytic nanoparticles. These particles, often just a few or tens of nanometers in size, are sensitive to intense X-ray beam illumination. Serial BCDI could enable tracking of morphology changes and strain evolution in such particles during the catalytic process, by sharing the dose over multiple particles. Furthermore, adapting serial BCDI to X-ray free-electron lasers (XFELs) could unlock ultrafast structural dynamics studies with femtosecond resolution.

To realize this vision, several developments are needed. First, the deep learning framework must be expanded to accommodate additional rotational degrees of freedom. Second, an effective interpolation method must be devised to map arbitrarily rotated diffraction frames into a unified 3D volume. Lastly, an automated pre-processing pipeline will be essential for filtering high-quality frames from large, unordered datasets.

X-ray diffraction imaging will continue to benefit from advances in synchrotron light sources, optics, detectors, and computational techniques. The work presented in this thesis contributes a small step toward making these techniques more robust and adaptable to complex experimental conditions. As we are in an era where materials are engineered with ever-increasing complexity and precision, the ability to visualize internal structure and strain becomes not just valuable, but essential. With continued innovation, X-ray diffraction imaging will remain at the forefront of materials characterization.

8 References

1. Röntgen, W. C. Uber eine neue Art von Strahlen. *Sitzung Physikal-Medicin Gesellschaft* **137,** 132–141 (1895).
2. Als-Nielsen, J. & McMorrow, D. *Elements of Modern X-ray Physics*. (Wiley, 2011). at <https://doi.org/10.1002/9781119998365>
3. Hecht, E. *Optics*. (Pearson Education India, 2012).
4. Bambynek, W., Crasemann, B., Fink, R., Freund, H.-U., Mark, H., Swift, C., Price, R. & Rao, P. V. X-ray fluorescence yields, Auger, and Coster-Kronig transition probabilities. *Reviews of modern physics* **44,** 716 (1972).
5. Krause, M. O. Atomic radiative and radiationless yields for K and L shells. *Journal of physical and chemical reference data* **8,** 307–327 (1979).
6. Berger, M., Hubbell, J., Seltzer, S., Coursey, J. & Zucker, D. XCOM: Photon Cross Section Database. (1999).
7. Kahnt, M., Selberg, J., Vogt, U., Åstrand, M., Björling, A., Kalbfleisch, S., Andreasen, J. W., Thånell, K. & Johansson, U. Current capabilities of the imaging endstation at the NanoMAX beamline. in *AIP Conference Proceedings* **2995,** 040018 (AIP Publishing, 2023).
8. Dzhigaev, D. Characterization of nanowires by coherent X-ray diffractive imaging and ptychography. (2017).
9. Friedrich, W., Knipping, P. & Laue, M. Interferenzerscheinungen bei roentgenstrahlen. *Annalen der Physik* **346,** 971–988 (1913).
10. Bragg, W. H. & Bragg, W. L. The reflection of X-rays by crystals. *Proceedings of the Royal Society of London. Series A, Containing Papers of a Mathematical and Physical Character* **88,** 428–438 (1913).
11. Ewald, P. P. Introduction to the dynamical theory of X-ray diffraction. *Acta Crystallographica Section A* **25,** 103–108 (1969).
12. Vartanyants, I. A. & Robinson, I. K. Partial coherence effects on the imaging of small crystals using coherent x-ray diffraction. *J. Phys.: Condens. Matter* **13,** 10593–10611 (2001).
13. In *X-Ray Diffraction* 341–384 (Pan Stanford, 2015). doi:10.1201/b15674-13
14. Friedel, G. Sur les symétries cristallines que peut révéler la diffraction des rayons Röntgen. *CR Acad. Sci. Paris* **157,** 1533–1536 (1913).
15. Attwood, D. T., Sakdinawat, A. & Geniesse, L. *X-rays and extreme ultraviolet radiation: principles and applications*. (Cambridge University Press, 2016).

16. Crookes, W. On the illumination of lines of molecular pressure, and the trajectory of molecules. *Phil. Trans. R. Soc.* **170,** 135–164 (1879).
17. Leemann, S. & Wurtz, W. Pushing the MAX IV 3 GeV storage ring brightness and coherence towards the limit of its magnetic lattice. *Nuclear Instruments and Methods in Physics Research Section A: Accelerators, Spectrometers, Detectors and Associated Equipment* **884,** 92–96 (2018).
18. Robert, A., Cerenius, Y., Tavares, P. F., Hultin Stigenberg, A., Karis, O., Lloyd Whelan, A.-C., Runéus, C. & Thunnissen, M. MAX IV Laboratory. *Eur. Phys. J. Plus* **138,** 495 (2023).
19. Tavares, P. F., Leemann, S. C., Sjöström, M. & Andersson, Å. The MAX IV storage ring project. *J Synchrotron Rad* **21,** 862–877 (2014).
20. Paganin, D. *Coherent X-Ray Optics*. (Oxford University Press, 2006). doi:10.1093/acprof:oso/9780198567288.001.0001
21. Willmott, P. *An introduction to synchrotron radiation: techniques and applications*. **49,** (John Wiley & Sons, 2019).
22. Eriksson, M., Van Der Veen, J. F. & Quitmann, C. Diffraction-limited storage rings – a window to the science of tomorrow. *J Synchrotron Rad* **21,** 837–842 (2014).
23. Thompson, A. C. & Vaughan, D. *X-ray data booklet*. **8,** (Lawrence Berkeley National Laboratory, University of California Berkeley, CA, 2001).
24. Björling, A., Kalbfleisch, S., Kahnt, M., Sala, S., Parfeniukas, K., Vogt, U., Carbone, D. & Johansson, U. Ptychographic characterization of a coherent nanofocused X-ray beam. *Opt. Express* **28,** 5069 (2020).
25. Johansson, U., Carbone, D., Kalbfleisch, S., Björling, A., Kahnt, M., Sala, S., Stankevic, T., Liebi, M., Rodriguez Fernandez, A., Bring, B., Paterson, D., Thånell, K., Bell, P., Erb, D., Weninger, C., Matej, Z., Roslund, L., Åhnberg, K., Norsk Jensen, B., Tarawneh, H., Mikkelsen, A. & Vogt, U. NanoMAX: the hard X-ray nanoprobe beamline at the MAX IV Laboratory. *J Synchrotron Rad* **28,** 1935–1947 (2021).
26. Carbone, D., Kalbfleisch, S., Johansson, U., Björling, A., Kahnt, M., Sala, S., Stankevic, T., Rodriguez-Fernandez, A., Bring, B. & Matej, Z. Design and performance of a dedicated coherent X-ray scanning diffraction instrument at beamline NanoMAX of MAX IV. *Synchrotron Radiation* **29,** 876–887 (2022).
27. Kirkpatrick, P. & Baez, A. V. Formation of optical images by X-rays. *Journal of the optical society of America* **38,** 766–774 (1948).
28. Mancuso, A. P. & Williams, G. J. High-resolution surface structures. *Nature Photonics* **6,** 574–575 (2012).
29. Berenguer, F., Godard, P., Allain, M., Belloir, J. M., Talneau, A., Ravy, S. & Chamard, V. X-ray lensless microscopy from undersampled diffraction intensities. *Physical Review B* **88,** 144101 (2013).
30. Hammarberg, S. Strain Mapping of Single Nanowires using Nano X-ray Diffraction.

31. Maddali, S., Li, P., Pateras, A., Timbie, D., Delegan, N., Crook, A., Lee, H., Calvo-Almazan, I., Sheyfer, D. & Cha, W. General approaches for shear-correcting coordinate transformations in Bragg coherent diffraction imaging. Part I. *Applied Crystallography* **53,** 393–403 (2020).

32. Chayanun, L., Hammarberg, S., Dierks, H., Otnes, G., Björling, A., Borgström, M. T. & Wallentin, J. Combining nanofocused x-rays with electrical measurements at the NanoMAX beamline. *Crystals* **9,** 432 (2019).

33. Chahine, G. A., Richard, M.-I., Homs-Regojo, R. A., Tran-Caliste, T. N., Carbone, D., Jacques, V. L. R., Grifone, R., Boesecke, P., Katzer, J., Costina, I., Djazouli, H., Schroeder, T. & Schülli, T. U. Imaging of strain and lattice orientation by quick scanning X-ray microscopy combined with three-dimensional reciprocal space mapping. *Journal of Applied Crystallography* **47,** 762–769 (2014).

34. Corley-Wiciak, C., Zoellner, M. H., Corley-Wiciak, A. A., Rovaris, F., Zatterin, E., Zaitsev, I., Sfuncia, G., Nicotra, G., Spirito, D., Von Den Driesch, N., Manganelli, C. L., Marzegalli, A., Schulli, T. U., Buca, D., Montalenti, F., Capellini, G. & Richter, C. Full Picture of Lattice Deformation in a $Ge_{1-x}Sn_x$ Micro-Disk by 5D X-ray Diffraction Microscopy. *Small Methods* **8,** 2400598 (2024).

35. Martens, I., Vostrov, N., Mirolo, M., Leake, S., Zatterin, E., Zhu, X., Wang, L., Drnec, J., Richard, M.-I. & Schulli, T. *Nanoimaging of solid solution domains during phase transitions inside LiNi0.5Mn1.5O4*. (Chemistry, 2022). doi:10.26434/chemrxiv-2022-lkzbj

36. Wallentin, J., Osterhoff, M. & Salditt, T. In Operando X-Ray Nanodiffraction Reveals Electrically Induced Bending and Lattice Contraction in a Single Nanowire Device. *Advanced Materials* **28,** 1788–1792 (2016).

37. Krause, T., Hanke, M., Cheng, Z., Niehle, M., Trampert, A., Rosenthal, M., Burghammer, M., Ledig, J., Hartmann, J. & Zhou, H. Nanofocus x-ray diffraction and cathodoluminescence investigations into individual core–shell (In, Ga) N/GaN rod light-emitting diodes. *Nanotechnology* **27,** 325707 (2016).

38. Schülli, T. U. & Leake, S. J. X-ray nanobeam diffraction imaging of materials. *Current Opinion in Solid State and Materials Science* **22,** 188–201 (2018).

39. Marçal, L. A. B., Oksenberg, E., Dzhigaev, D., Hammarberg, S., Rothman, A., Björling, A., Unger, E., Mikkelsen, A., Joselevich, E. & Wallentin, J. *In Situ* Imaging of Ferroelastic Domain Dynamics in $CsPbBr_3$ Perovskite Nanowires by Nanofocused Scanning X-ray Diffraction. *ACS Nano* **14,** 15973–15982 (2020).

40. Dzhigaev, D., Svensson, J., Krishnaraja, A., Zhu, Z., Ren, Z., Liu, Y., Kalbfleisch, S., Björling, A., Lenrick, F., Balogh, Z. I., Hammarberg, S., Wallentin, J., Timm, R., Wernersson, L.-E. & Mikkelsen, A. Strain mapping inside an individual processed vertical nanowire transistor using scanning X-ray nanodiffraction. *Nanoscale* **12,** 14487–14493 (2020).

41. Marçal, L. A., Benter, S., Irish, A., Dzhigaev, D., Oksenberg, E., Rothman, A., Sanders, E., Hammarberg, S., Zhang, Z. & Sala, S. Inducing ferroelastic domains in single-crystal CsPbBr 3 perovskite nanowires using atomic force microscopy. *Physical review materials* **5,** L063001 (2021).

42. Shin, J., Cornelius, T., Labat, S., Lauraux, F., Richard, M.-I., Richter, G., Blanchard, N., Gianola, D. & Thomas, O. In situ Bragg coherent X-ray diffraction during tensile testing of an individual Au nanowire. *Applied Crystallography* **51,** 781–788 (2018).
43. Fienup, J. R. Reconstruction of an object from the modulus of its Fourier transform. *Opt. Lett.* **3,** 27 (1978).
44. Miao, J., Charalambous, P., Kirz, J. & Sayre, D. Extending the methodology of X-ray crystallography to allow imaging of micrometre-sized non-crystalline specimens. *Nature* **400,** 342–344 (1999).
45. Robinson, I. K., Vartanyants, I. A., Williams, G. J., Pfeifer, M. A. & Pitney, J. A. Reconstruction of the shapes of gold nanocrystals using coherent x-ray diffraction. *Phys Rev Lett* **87,** (2001).
46. Suzana, A. F., Lee, S. S., Calvo-Almazán, I., Cha, W., Harder, R. & Fenter, P. Visualizing the Internal Nanocrystallinity of Calcite Due to Nonclassical Crystallization by 3D Coherent X-Ray Diffraction Imaging. *Advanced Materials* **36,** 2310672 (2024).
47. Atlan, C., Chatelier, C., Martens, I., Dupraz, M., Viola, A., Li, N., Gao, L., Leake, S. J., Schülli, T. U., Eymery, J., Maillard, F. & Richard, M.-I. Imaging the strain evolution of a platinum nanoparticle under electrochemical control. *Nat. Mater.* **22,** 754–761 (2023).
48. Miao, J. W., Ishikawa, T., Robinson, I. K. & Murnane, M. M. Beyond crystallography: Diffractive imaging using coherent x-ray light sources. *Science* **348,** 530–535 (2015).
49. Pfeifer, M. A., Williams, G. J., Vartanyants, I. A., Harder, R. & Robinson, I. K. Three-dimensional mapping of a deformation field inside a nanocrystal. *Nature* **442,** 63–66 (2006).
50. Newton, M. C., Leake, S. J., Harder, R. & Robinson, I. K. Three-dimensional imaging of strain in a single ZnO nanorod. *Nat Mater* **9,** 120–124 (2010).
51. Diao, J., Wu, L., Suzana, A. F., Bozin, E. S., Zatterin, E. M., Leake, S. J., Harder, R. J., Cha, W., Abeykoon, M., Fan, J., Jiang, H. & Robinson, I. K. Behavior of strain stripe networks in barium titanate nanocrystals on crossing its ferroelectric phase transition. *Phys. Rev. Materials* **8,** 016002 (2024).
52. Hruszkewycz, S. O., Maddali, S., Anderson, C. P., Cha, W., Miao, K. C., Highland, M. J., Ulvestad, A., Awschalom, D. D. & Heremans, F. J. Strain annealing of SiC nanoparticles revealed through Bragg coherent diffraction imaging for quantum technologies. *Phys. Rev. Materials* **2,** 086001 (2018).
53. Marchesini, S. Invited Article: A unified evaluation of iterative projection algorithms for phase retrieval. *Review of Scientific Instruments* **78,** 011301 (2007).
54. Marchesini, S. Phase retrieval and saddle-point optimization. *Journal of the Optical Society of America A* **24,** 3289–3296 (2007).
55. Sayre, D. & Schlenker, M. Imaging processes and coherence in physics. *Springer Lecture Notes in Physics* **112,** 229–235 (1980).
56. Fienup, J. R. Phase retrieval algorithms: a comparison. *Appl. Opt.* **21,** 2758 (1982).

57. Marchesini, S., He, H., Chapman, H. N., Hau-Riege, S. P., Noy, A., Howells, M. R., Weierstall, U. & Spence, J. C. H. X-ray image reconstruction from a diffraction pattern alone. *Physical Review B* **68,** 140101 (2003).

58. Luke, D. R. Relaxed averaged alternating reflections for diffraction imaging. *Inverse Problems* **21,** 37–50 (2005).

59. Favre-Nicolin, V., Girard, G., Leake, S., Carnis, J., Chushkin, Y., Kieffer, J., Paleo, P. & Richard, M.-I. PyNX: high-performance computing toolkit for coherent X-ray imaging based on operators. *Journal of Applied Crystallography* **53,** 1404–1413 (2020).

60. Horstmeyer, R., Heintzmann, R., Popescu, G., Waller, L. & Yang, C. Standardizing the resolution claims for coherent microscopy. *Nature Photon* **10,** 68–71 (2016).

61. Chapman, H. N., Barty, A., Marchesini, S., Noy, A., Hau-Riege, S. P., Cui, C., Howells, M. R., Rosen, R., He, H. & Spence, J. C. High-resolution ab initio three-dimensional x-ray diffraction microscopy. *Journal of the Optical society of America A* **23,** 1179–1200 (2006).

62. Buhr, E., Günther-Kohfahl, S. & Neitzel, U. Accuracy of a simple method for deriving the presampled modulation transfer function of a digital radiographic system from an edge image. *Medical physics* **30,** 2323–2331 (2003).

63. Davtyan, A., Favre-Nicolin, V., Lewis, R. B., Küpers, H., Geelhaar, L., Kriegner, D., Bahrami, D., Al-Hassan, A., Chahine, G., Loffeld, O. & Pietsch, U. Coherent X-ray diffraction imaging meets ptychography to study core-shell-shell nanowires. *MRS Advances* **3,** 2317–2322 (2018).

64. Hill, M. O., Calvo-Almazan, I., Allain, M., Holt, M. V., Ulvestad, A., Treu, J., Koblmuller, G., Huang, C. Y., Huang, X. J., Yan, H. F., Nazaretski, E., Chu, Y. S., Stephenson, G. B., Chamard, V., Lauhon, L. J. & Hruszkewycz, S. O. Measuring Three-Dimensional Strain and Structural Defects in a Single InGaAs Nanowire Using Coherent X-ray Multiangle Bragg Projection Ptychography. *Nano Lett* **18,** 811–819 (2018).

65. Liang, M., Harder, R. & Robinson, I. Radiation-driven rotational motion of nanoparticles. *J Synchrotron Rad* **25,** 757–762 (2018).

66. Kim, J. W., Ulvestad, A., Manna, S., Harder, R., Fohtung, E., Singer, A., Boucheron, L., Fullerton, E. E. & Shpyrko, O. G. Observation of x-ray radiation pressure effects on nanocrystals. *J. Appl. Phys.* **120,** 163102 (2016).

67. Bjorling, A., Carbone, D., Sarabia, F. J., Hammarberg, S., Feliu, J. M. & Solla-Gullon, J. Coherent Bragg imaging of 60nm Au nanoparticles under electrochemical control at the NanoMAX beamline. *J Synchrotron Radiat* **26,** 1830–1834 (2019).

68. Calvo-Almazán, I., Allain, M., Maddali, S., Chamard, V. & Hruszkewycz, S. O. Impact and mitigation of angular uncertainties in Bragg coherent x-ray diffraction imaging. *Sci Rep* **9,** 6386 (2019).

69. Björling, A., Marçal, L. A. B., Solla-Gullón, J., Wallentin, J., Carbone, D. & Maia, F. R. N. C. Three-Dimensional Coherent Bragg Imaging of Rotating Nanoparticles. *Phys Rev Lett* **125,** 246101 (2020).

70. Wallentin, J., Anttu, N., Asoli, D., Huffman, M., Åberg, I., Magnusson, M. H., Siefer, G., Fuss-Kailuweit, P., Dimroth, F., Witzigmann, B., Xu, H. Q., Samuelson, L., Deppert, K. & Borgström, M. T. InP Nanowire Array Solar Cells Achieving 13.8% Efficiency by Exceeding the Ray Optics Limit. *Science* **339,** 1057–1060 (2013).

71. Otnes, G. & Borgström, M. T. Towards high efficiency nanowire solar cells. *Nano Today* **12,** 31–45 (2017).

72. Gudiksen, M. S., Lauhon, L. J., Wang, J., Smith, D. C. & Lieber, C. M. Growth of nanowire superlattice structures for nanoscale photonics and electronics. *nature* **415,** 617–620 (2002).

73. Gibson, S. J., van Kasteren, B., Tekcan, B., Cui, Y., van Dam, D., Haverkort, J. E., Bakkers, E. P. & Reimer, M. E. Tapered InP nanowire arrays for efficient broadband high-speed single-photon detection. *Nature nanotechnology* **14,** 473–479 (2019).

74. Motohisa, J., Kameda, H., Sasaki, M. & Tomioka, K. Characterization of nanowire light-emitting diodes grown by selective-area metal-organic vapor-phase epitaxy. *Nanotechnology* **30,** 134002 (2019).

75. Corfdir, P., Marquardt, O., Lewis, R. B., Sinito, C., Ramsteiner, M., Trampert, A., Jahn, U., Geelhaar, L., Brandt, O. & Fomin, V. M. Excitonic Aharonov–Bohm oscillations in core–shell nanowires. *Advanced Materials* **31,** 1805645 (2019).

76. Mourik, V., Zuo, K., Frolov, S. M., Plissard, S., Bakkers, E. P. & Kouwenhoven, L. P. Signatures of Majorana fermions in hybrid superconductor-semiconductor nanowire devices. *Science* **336,** 1003–1007 (2012).

77. Zhang, H., Liu, D. E., Wimmer, M. & Kouwenhoven, L. P. Next steps of quantum transport in Majorana nanowire devices. *Nat Commun* **10,** (2019).

78. Haffouz, S., Zeuner, K. D., Dalacu, D., Poole, P. J., Lapointe, J., Poitras, D., Mnaymneh, K., Wu, X., Couillard, M. & Korkusinski, M. Bright single InAsP quantum dots at telecom wavelengths in position-controlled InP nanowires: the role of the photonic waveguide. *Nano letters* **18,** 3047–3052 (2018).

79. Ertekin, E., Greaney, P. A., Chrzan, D. C. & Sands, T. D. Equilibrium limits of coherency in strained nanowire heterostructures. *Journal of Applied Physics* **97,** 114325 (2005).

80. Ye, H., Lu, P., Yu, Z., Song, Y., Wang, D. & Wang, S. Critical Thickness and Radius for Axial Heterostructure Nanowires Using Finite-Element Method. *Nano Lett.* **9,** 1921–1925 (2009).

81. Glas, F. in *Semiconductors and Semimetals* **93,** 79–123 (Elsevier, 2015).

82. Wadhawan, V. *Introduction to Ferroic Materials*. (CRC press, 2000). at <https://doi.org/10.1201/9781482283051>

83. Jia, C., Lin, Z., Huang, Y. & Duan, X. Nanowire Electronics: From Nanoscale to Macroscale. *Chem. Rev.* **119,** 9074–9135 (2019).

84. Tomioka, K., Yoshimura, M. & Fukui, T. A III–V nanowire channel on silicon for high-performance vertical transistors. *Nature* **488,** 189–192 (2012).

85. Memisevic, E., Hellenbrand, M., Lind, E., Persson, A. R., Sant, S., Schenk, A., Svensson, J., Wallenberg, R. & Wernersson, L.-E. Individual Defects in InAs/InGaAsSb/GaSb Nanowire Tunnel Field-Effect Transistors Operating below 60 mV/decade. *Nano Lett.* **17,** 4373–4380 (2017).

86. Al-Ashouri, A., Köhnen, E., Li, B., Magomedov, A., Hempel, H., Caprioglio, P., Márquez, J. A., Morales Vilches, A. B., Kasparavicius, E. & Smith, J. A. Monolithic perovskite/silicon tandem solar cell with> 29% efficiency by enhanced hole extraction. *Science* **370,** 1300–1309 (2020).

87. Liu, X.-K., Xu, W., Bai, S., Jin, Y., Wang, J., Friend, R. H. & Gao, F. Metal halide perovskites for light-emitting diodes. *Nature Materials* **20,** 10–21 (2021).

88. Chen, Q., Wu, J., Ou, X., Huang, B., Almutlaq, J., Zhumekenov, A. A., Guan, X., Han, S., Liang, L. & Yi, Z. All-inorganic perovskite nanocrystal scintillators. *Nature* **561,** 88–93 (2018).

89. Zhu, H., Fu, Y., Meng, F., Wu, X., Gong, Z., Ding, Q., Gustafsson, M. V., Trinh, M. T., Jin, S. & Zhu, X.-Y. Lead halide perovskite nanowire lasers with low lasing thresholds and high quality factors. *Nature Mater* **14,** 636–642 (2015).

90. Marçal, L. A. B., Lamers, N., Hammarberg, S., Zhang, Z., Chen, H., Dzhigaev, D., Gomez-Gonzalez, M. A., Parker, J. E., Björling, A., Mikkelsen, A. & Wallentin, J. Structural and chemical properties of anion exchanged CsPb(Br(1−x)Clx)3 heterostructured perovskite nanowires imaged by nanofocused x-rays. *Nanotechnology* **35,** 265710 (2024).

91. Liu, Y.-P., Lamers, N., Zhang, Z., Zaiats, N., Mikkelsen, A., Wallentin, J., Dittmann, R. & Timm, R. Ion Migration and Redox Reactions in Axial Heterojunction Perovskite CsPb (Br1–x Cl x) 3 Nanowire Devices Revealed by Operando Nanofocused X-ray Photoelectron Spectroscopy. *ACS nano* **18,** 34763–34775 (2024).

92. Zhang, Z., Lamers, N., Sun, C., Hetherington, C., Scheblykin, I. G. & Wallentin, J. Free-Standing Metal Halide Perovskite Nanowire Arrays with Blue-Green Heterostructures. *Nano Lett.* **22,** 2941–2947 (2022).

93. Huang, Z., Zhang, Z., Lamers, N., Baranov, D. & Wallentin, J. Controlled Ligand-Free Growth of Free-Standing $CsPbBr_3$ Perovskite Nanowires. *ACS Omega* **9,** 48390–48396 (2024).

94. Strelcov, E., Dong, Q., Li, T., Chae, J., Shao, Y., Deng, Y., Gruverman, A., Huang, J. & Centrone, A. $CH_3NH_3PbI_3$ perovskites: Ferroelasticity revealed. *Sci. Adv.* **3,** (2017).

95. Martin, L. W. & Rappe, A. M. Thin-film ferroelectric materials and their applications. *Nature Reviews Materials* **2,** 1–14 (2016).

96. Hruszkewycz, S., Folkman, C., Highland, M., Holt, M., Baek, S., Streiffer, S., Baldo, P., Eom, C. & Fuoss, P. X-ray nanodiffraction of tilted domains in a poled epitaxial BiFeO3 thin film. *Applied Physics Letters* **99,** (2011).

97. Guzelturk, B., Yang, T., Liu, Y., Wei, C., Orenstein, G., Trigo, M., Zhou, T., Diroll, B. T., Holt, M. V. & Wen, H. Sub-Nanosecond Reconfiguration of Ferroelectric Domains in Bismuth Ferrite. *Advanced Materials* **35,** 2306029 (2023).

98. Udovenko, S., Son, Y., Tipsawat, P., Knox, R. J., Hruszkewycz, S. O., Yan, H., Huang, X., Pattammattel, A., Zajac, M., Cha, W., Pagan, D. C. & Trolier-McKinstry, S. Mapping domain structures near a grain boundary in a lead zirconate titanate ferroelectric film using X-ray nanodiffraction. *J Appl Crystallogr* **57,** 1789–1799 (2024).
99. Laanait, N., Saenrang, W., Zhou, H., Eom, C.-B. & Zhang, Z. Dynamic X-ray diffraction imaging of the ferroelectric response in bismuth ferrite. *Advanced structural and chemical imaging* **3,** 1–12 (2017).
100. Sando, D., Barthélémy, A. & Bibes, M. BiFeO3 epitaxial thin films and devices: past, present and future. *Journal of Physics: Condensed Matter* **26,** 473201 (2014).
101. Wang, A., Chen, R., Yun, Y., Xu, J. & Zhang, J. Review of Ferroelectric Materials and Devices toward Ultralow Voltage Operation. *Adv Funct Materials* **35,** (2025).
102. Loh, N.-T. D. & Elser, V. Reconstruction algorithm for single-particle diffraction imaging experiments. *Physical Review E* **80,** 026705 (2009).
103. Loh, N. D., Bogan, M. J., Elser, V., Barty, A., Boutet, S., Bajt, S., Hajdu, J., Ekeberg, T., Maia, F. R. N. C., Schulz, J., Seibert, M. M., Iwan, B., Timneanu, N., Marchesini, S., Schlichting, I., Shoeman, R. L., Lomb, L., Frank, M., Liang, M. & Chapman, H. N. Cryptotomography: Reconstructing 3D Fourier Intensities from Randomly Oriented Single-Shot Diffraction Patterns (vol 104, 225501, 2010). *Phys Rev Lett* **104,** (2010).
104. Zhang, Y., Andreas Noack, M., Vagovic, P., Fezzaa, K., Garcia-Moreno, F., Ritschel, T. & Villanueva-Perez, P. PhaseGAN: a deep-learning phase-retrieval approach for unpaired datasets. *Opt. Express* **29,** 19593 (2021).
105. Wu, L., Yoo, S., Suzana, A. F., Assefa, T. A., Diao, J., Harder, R. J., Cha, W. & Robinson, I. K. Three-dimensional coherent X-ray diffraction imaging via deep convolutional neural networks. *npj Comput Mater* **7,** 175 (2021).
106. Zhang, Y., Yao, Z., Klöfkorn, R., Ritschel, T. & Villanueva-Perez, P. 4D-ONIX for reconstructing 3D movies from sparse X-ray projections via deep learning. *Commun Eng* **4,** (2025).
107. Villanueva-Perez, P., Bellucci, V., Zhang, Y., Birnsteinova, S., Graceffa, R., Adriano, L., Asimakopoulou, E. M., Petrov, I., Yao, Z., Romagnoni, M., Mazzolari, A., Letrun, R., Kim, C., Koliyadu, J. C. P., Deiter, C., Bean, R., Giovanetti, G., Gelisio, L., Ritschel, T., Mancuso, A., Chapman, H. N., Meents, A., Sato, T. & Vagovic, P. Megahertz X-ray Multi-projection imaging. Preprint at https://doi.org/10.48550/arXiv.2305.11920 (2023)
108. Wu, L., Bak, S., Shin, Y., Chu, Y. S., Yoo, S., Robinson, I. K. & Huang, X. Resolution-enhanced X-ray fluorescence microscopy via deep residual networks. *npj Comput Mater* **9,** 43 (2023).
109. Masto, M., Favre-Nicolin, V., Leake, S., Schülli, T., Richard, M.-I. & Bellec, E. Patching-based deep-learning model for the inpainting of Bragg coherent diffraction patterns affected by detector gaps. *Applied Crystallography* **57,** (2024).
110. Goodfellow, I., Bengio, Y., Courville, A. & Bengio, Y. *Deep learning*. **1,** (MIT press Cambridge, 2016).
111. LeCun, Y., Bengio, Y. & Hinton, G. Deep learning. *nature* **521,** 436–444 (2015).

112. Robbins, H. & Monro, S. A stochastic approximation method. *The annals of mathematical statistics* 400–407 (1951).
113. Krizhevsky, A., Sutskever, I. & Hinton, G. E. ImageNet classification with deep convolutional neural networks. *Communications of the ACM* **60,** 84–90 (2017).
114. Deng, J., Dong, W., Socher, R., Li, L.-J., Li, K. & Fei-Fei, L. Imagenet: A large-scale hierarchical image database. in 248–255 (Ieee, 2009).
115. Hopfield, J. J. Neural networks and physical systems with emergent collective computational abilities. *Proceedings of the National Academy of Sciences* **79,** 2554–2558 (1982).
116. Ackley, D. H., Hinton, G. E. & Sejnowski, T. J. A learning algorithm for boltzmann machines. *Cognitive Science* **9,** 147–169 (1985).
117. Hornik, K., Stinchcombe, M. & White, H. Multilayer feedforward networks are universal approximators. *Neural networks* **2,** 359–366 (1989).
118. LeCun, Y. & Bengio, Y. Convolutional networks for images, speech, and time series. *The handbook of brain theory and neural networks* **3361,** 1995 (1995).
119. LeCun, Y., Bottou, L., Bengio, Y. & Haffner, P. Gradient-based learning applied to document recognition. *Proceedings of the IEEE* **86,** 2278–2324 (2002).